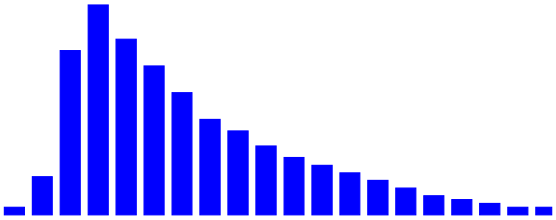

# Becker & Hickl GmbH

## FLIM Systems

## for Zeiss

## LSM 710 / 780 / 880 / 980

## Laser Scanning Microscopes

## An Overview

2021

Becker & Hickl GmbH
Nunsdorfer Ring 7-9
12277 Berlin
Germany
Tel. +49 / 30 / 212 800 20
FAX +49 / 30 / 212 800 213
http://www.becker-hickl.com
email: info@becker-hickl.com

June 2021

# FLIM Systems for Zeiss LSM 710 / 780 / 880 / 980 Laser Scanning Microscopes An Overview

*Abstract:* The FLIM systems for the Zeiss LSM 710 /780 / 880 / 980 family laser scanning microscopes are based on bh's Multi-Dimensional TCSPC technique and 64 bit Megapixel technology [28, 37]. The systems feature single-photon sensitivity, excellent spatial and temporal resolution, multi-exponential decay analysis, and short acquisition time. The systems are available both for confocal and for multiphoton versions of the Zeiss LSMs. The recording functions include basic FLIM recording, dual-channel FLIM, excitation-wavelength-multiplexed FLIM, Z stack FLIM, time-series FLIM, spatial and temporal mosaic FLIM, fluorescence lifetime-transient scanning (FLITS), and phosphorescence lifetime imaging (PLIM). Multi-spectral FLIM is available by adding a special detector to the system. Unlike other systems, the bh FLIM systems are true molecular imaging systems. They use the fluorescence lifetime not only as a contrast parameter but as an indicator of the molecular state of the sample. This becomes possible by recording the complex multi-exponential decay behaviour in the individual pixels and analysing the data with advanced data analysis procedures based on a combination of MLE-based time-domain analysis, phasor analysis, and image segmentation functions. This brochure gives an overview of the recording functions of the systems, the data analysis, and the application to FRET measurements, autofluorescence FLIM of tissue, metabolic imaging, time-resolved recording of fast physiological processes, and plant physiology. For complete information please see handbook of the bh FLIM systems for the Zeiss LSM series microscopes [6] and addendum for LSM 980 microscopes [7].

## Introduction

Becker & Hickl introduced their multi-dimensional TCSPC technique in 1993. Fluorescence lifetime imaging started in 1996 with applications in ophthalmology [172]. The first FLIM module for laser scanning microscopes was introduced in 1998, bh FLIM systems for the Zeiss LSM laser scanning microscopes are available since 2000 [23, 24]. Since then, several new generations of LSM family laser scanning microscopes, and several generations of bh FLIM modules have been introduced. As a result, a wide variety of bh FLIM systems and of FLIM system configurations are in use [28, 37]. The excitation light source can be the Ti:Sapphire laser of a multiphoton microscope, a picosecond diode laser attached to or integrated in the microscope, or a visible-range tuneable solid state laser. The fluorescence light may be detected via a confocal port of the scan head or via a non-descanned port of a multiphoton microscope. Signals may be detected by one detector, simultaneously by two, three, or four detectors, or by the 16 channels of a bh multi-wavelength detector.

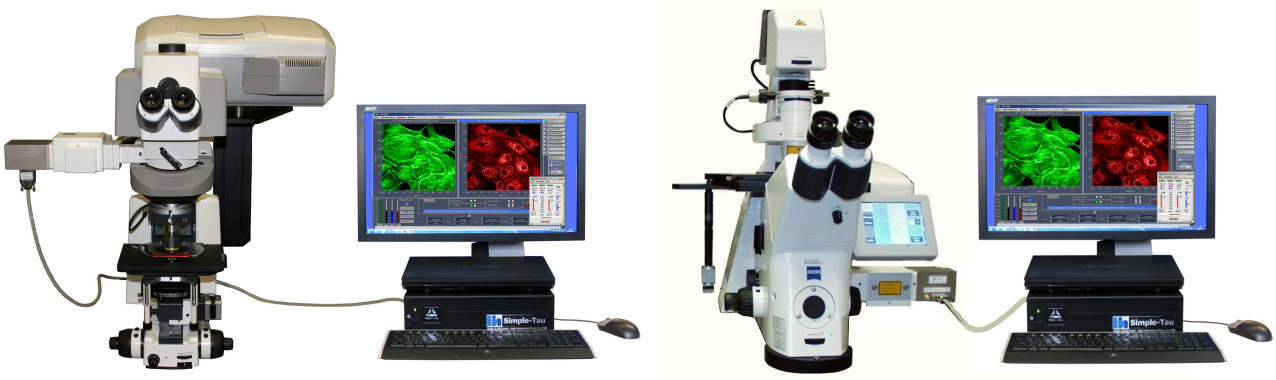

Fig. 1: LSM 710 Multiphoton NDD FLIM systems

The bh FLIM systems are using highly efficient GaAsP hybrid detectors. By combining extremely high efficiency with large active area, high counting speed, high time-resolution, and low background, these detectors have triggered a breakthrough in FLIM recording. Another step was made by the

introduction of 64-bit data acquisition software. FLIM data are now recorded at unprecedented pixel numbers, high dynamic range, short acquisition time, and minimum exposure of the sample.

Most importantly, the bh FLIM systems are based on a new understanding of FLIM in general. FLIM is no longer considered simply a way of adding lifetime contrast to a microscopy image. It is considered a technique of molecular imaging, i.e. of recording and visualising molecular parameters and molecular processes in biological systems. Following this idea, the FLIM systems are designed to observe several parameters of biological system simultaneously, and in their mutual dependence. This is supported by advanced FLIM functions, like multi-channel operation, excitation-wavelength-multiplexing, time-series FLIM, Z stack FLIM, spatial and temporal Mosaic FLIM, simultaneous fluorescence and phosphorescence lifetime imaging (FLIM/PLIM), fluorescence lifetime-transient scanning (FLITS). [37, 193], and combinations of these techniques. An overview of the functions of the bh FLIM systems is given in Fig. 2. For a detailed description please see [6] and [7]. We also recommend [28, 37, 40] as supporting literature.

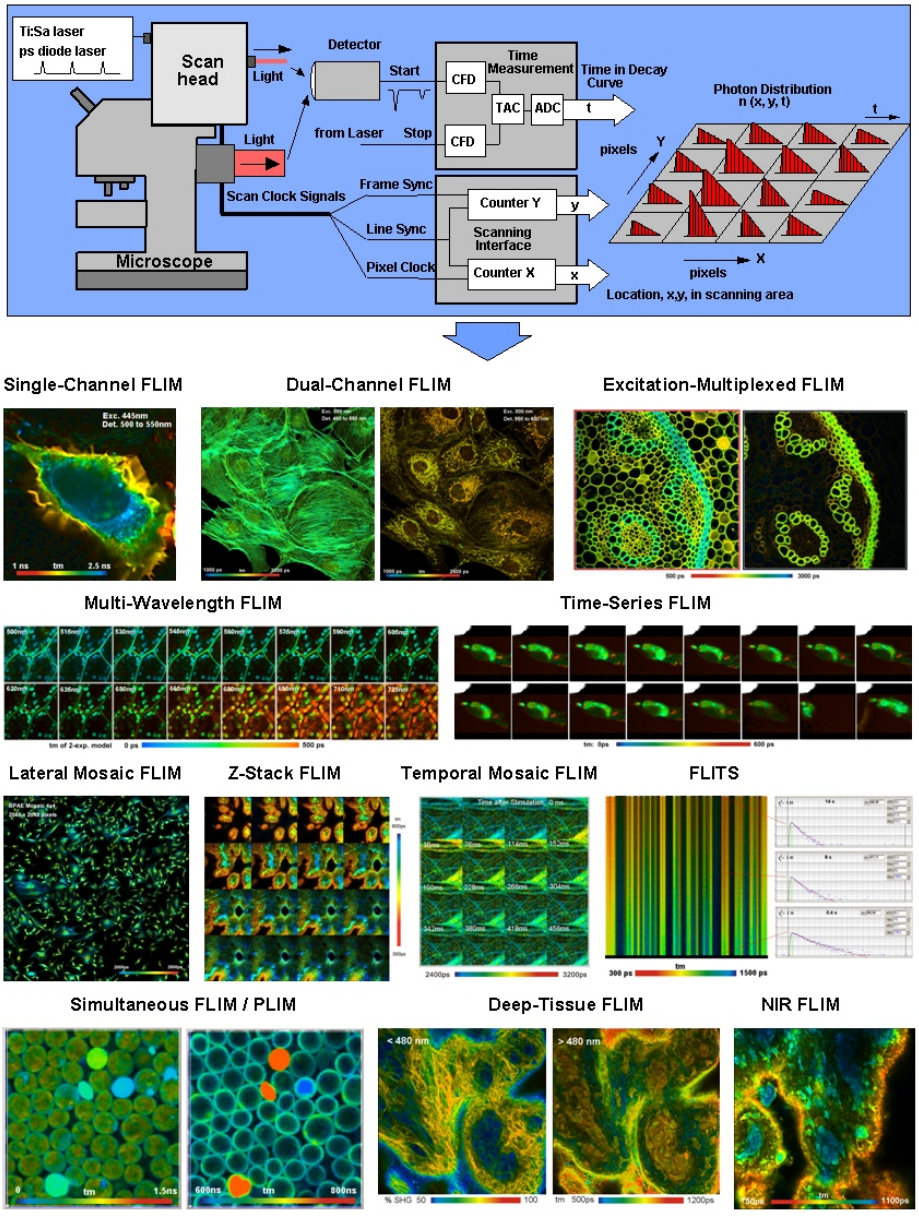


Fig. 2: Overview on bh FLIM functions

# Essential Features

## TCSPC System

bh FLIM systems are unsurpassed in time resolution. With the new SPC-150NX or SPC-180NX TCSPC the systems reach unprecedented timing stability and time resolution. The electrical time resolution is better than 3 ps (FWHM!), the timing stability better than 0.5 ps (RMS) [37, 38] (Fig. 3, left and middle). With the new ultra-fast HPM-100-06 detectors, the instrument-response function for multiphoton systems is <20 ps (FWHM), see Fig. 3, right. Timing performance on this level is entirely out of the reach of any other FLIM system. With their fast detectors and negligible timing jitter of the electronics, the systems accurately record fluorescence-decay components which previously were unknown to even exist. Moreover, the time resolution does not degrade over extended acquisition times. Extremely weak signals or signals from extremely fragile samples can therefore be recorded successfully. The high stability in combination with sophisticated data analysis makes it unnecessary to re-calibrate the system by repeated recording of the instrument-response function (IRF). This is a significant advantage for practical use.

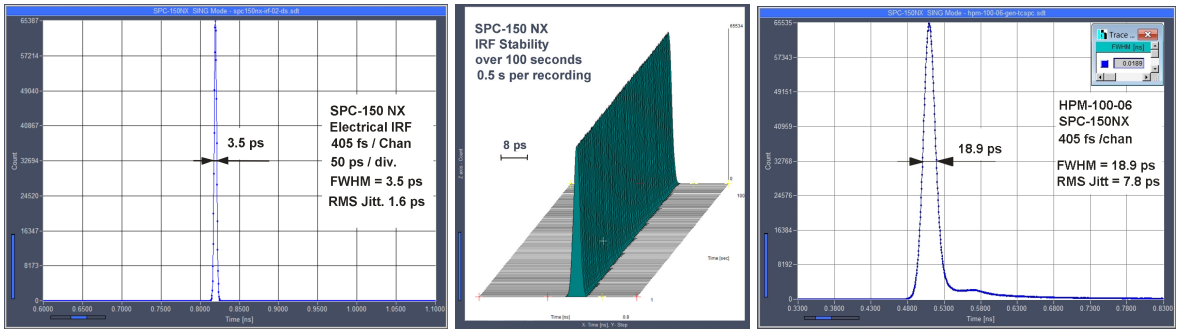


Fig. 3, left to right: Electrical IRF of SPC-150NX, IRF stability over 100 s, IRF of multiphoton system with HPM-100-06

In addition, the bh FLIM systems feature near-ideal photon efficiency and minimum acquisition time to reach a given accuracy for a given photon rate. The pixels of the recorded FLIM images contain precision fluorescence decay curves in a large number of time channels, allowing the user to derive multi-exponential decay parameters from the data. The most intriguing feature is the multi-dimensional nature of the recording process. bh FLIM systems are able to record at several excitation wavelengths simultaneously, record dynamic processes in live samples down to the millisecond range, record FLIM and PLIM simultaneously, or record multi-spectral FLIM images. With these capabilities, bh FLIM systems are true molecular imaging systems, able to observe several parameters of biological system simultaneously, and in their mutual dependence.

## Lasers for Confocal FLIM

bh FLIM systems for the LSM 710, 780, and 880 confocal microscopes had one or two ps diode lasers. These were integrated in the hardware and software of the Zeiss LSM systems. With just two laser wavelengths and limited control over the laser function, these systems were limited both in excitation wavelength and recording functions. The LSM 980 confocal FLIM systems are coming with four ps diode lasers of different wavelength [7]. The lasers are contained in the LHB-104 ‘Laser Hub’ [9], shown in Fig. 4. The lasers are coupled into the LSM 980 scan head via a single-mode fibre with a standard Zeiss / Lasos fibre coupler. The lasers can be switched on an off on demand, multiplexed in time for excitation-wavelength multiplexed FLIM, or on/off modulated for simultaneous FLIM / PLIM.

Fig. 4: LBH-104 ‘Laser Hub’. Output of four wavelengths via single fibre with Zeiss / Lasos coupler, demonstrated by reflection off an optical grating.

## Laser for Multiphoton FLIM

The bh FLIM systems work both with the confocal versions and with the multiphoton versions of the Zeiss LSMs. The excitation source in multiphoton systems is normally a Ti:Sa laser. The FLIM systems are perfectly compatible with these lasers [6]. In principle, they also work with femtosecond fibre lasers, should one of these by used in combination with a Zeiss LSM.

## Detectors

the bh FLIM systems for Zeiss LSMs are using the bh HPM-100 hybrid detectors [31]. The advantage of these detectors is that they have a fast and clean TCSPC response (IRF), and that they have no afterpulsing. The fast IRF and the absence of afterpulsing background have the effect that FLIM data analysis works close to the theoretical limit of photon efficiency [10]. Two versions of the HPM-100 are used for FLIM. The HPM-100-40 is used in applications which require highest sensitivity, the HPM-100-06 in applications which require highest time resolution. Detectors and detector assemblies are compatible both with the BIG port of confocal microscopes and with the NDD ports of multiphoton microscopes. The detectors and detector assemblies are fully integrated in the laser-safety loop of the LSM systems.

Fig. 5: HPM-100 hybrid detector and dual-detector assembly with adapter to the optical ports of the Zeiss LSM systems

The bh FLIM systems also work with the Zeiss GaAsP BIG-2 detectors [15]. The time resolution with these detectors does not reach the resolution of the HPM detectors, but using them has the advantage that no additional hardware has to be attached to the microscope. Additionally, there is the bh MW FLIM detector for recording multi-spectral FLIM data. Also this detector is available with a highly efficient GaAsP cathode [37].

## SPCM Data Acquisition Software

The bh TCSPC modules come with the ‘Multi SPC Software’, SPCM, a software package that allows the user to operate up to four bh TCSPC / FLIM modules. SPCM runs the data acquisition in the various operation modes of the SPC modules while controlling peripheral devices, such as detectors and lasers. Operation modes are available for almost any conceivable TCSPC application, such as

fluorescence and phosphorescence decay recording, multi-wavelength decay recording, laser-wavelength multiplexing, recording of time series, FCS and photon counting histograms, single- and dual, or quadruple-channel FLIM, multi-wavelength FLIM, Mosaic FLIM, time-series FLIM, Z stack FLIM, and simultaneous FLIM / PLIM. Current bh SPCM data acquisition software includes fast online-FLIM display and online display of decay curves in selectable regions or points of interest, see Fig. 6. Moreover, SPCM has been upgraded with extended multi-threading functions, avoiding bus saturation even at the highest count rates and when the online FLIM and curve display functions are used [37].

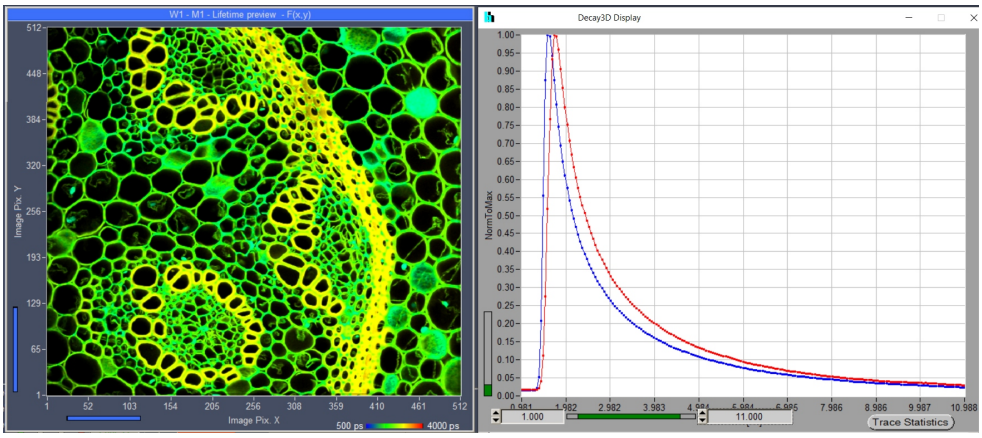


Fig. 6: Online display of lifetime images (left) and online display of decay curves in selectable regions of interest (right)

## SPCImage NG Data Analysis Software

The LSM 710 /780 / 880 / 980 FLIM systems use BH's SPCImage NG next generation data analysis software [8]. SPCImage NG is a combination of time-domain and phasor analysis. It uses maximum-likelihood estimation (MLE) to calculate the FLIM images, resulting in superior photon efficiency of multi-exponential decay analysis. Image segmentation via the phasor plot allows decay parameters to be precisely determined even in data of low photon number. Calculations are running on a GPU (graphics-processor unit). By GPU processing, calculation times are reduced from formerly more than 10 minutes to a few seconds. Another novel feature is advanced modelling of the system IRF. In combination with the extraordinary timing stability of the bh FLIM system, IRF modelling makes the recording of an IRF unnecessary. Please see [8] or [37] for details.

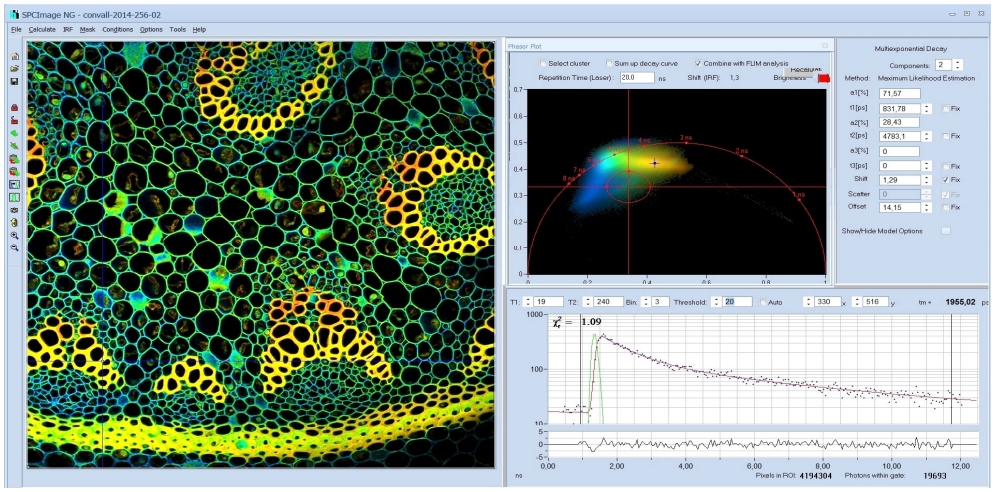


Fig. 7: SPCImage NG Data analysis software. FLIM image (left), phasor plot (upper right), decay curve at cursor position (lower right).

## Principle of the bh FLIM Technique

*Multi-Dimensional TCSPC*

he bh FLIM systems use a combination of bh's multidimensional time-correlated single-photon counting process with confocal or multiphoton laser scanning [28, 37, 41, 42]. The principle is shown in Fig. 8. The laser scanning microscope scans the sample with a focused beam of a high-repetition-rate pulsed laser. Depending on the laser used, the fluorescence in the sample can either be excited by one-photon or by multiphoton excitation. The FLIM detector is attached either to a confocal or non-descanned port of the laser scanning microscope [6, 23, 24, 25, 26, 27, 37]. For every detected photon the detector sends an electrical pulse into the TCSPC module. Moreover, the TCSPC module receives scan clock signals (pixel, line, and frame clock) from the scanning unit of the microscope.

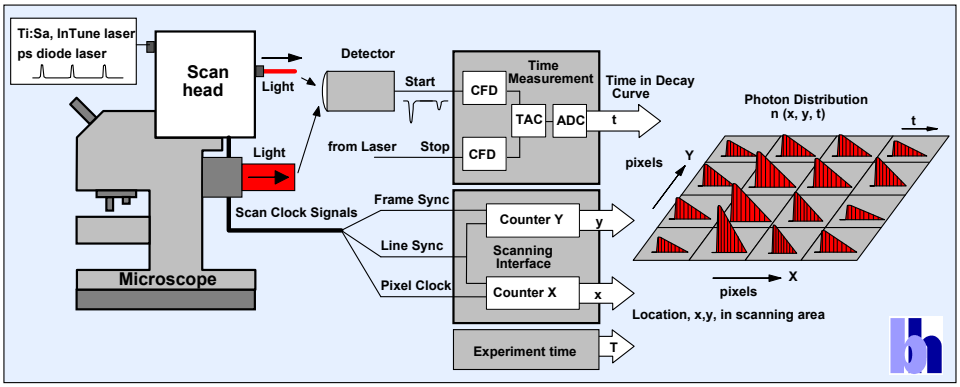


Fig. 8: Multidimensional TCSPC architecture for FLIM

For each photon pulse from the detector, the TCSPC module determines the time within the laser pulse sequence (i.e. in the fluorescence decay) and the location within the scanning area, x and y. The photon times, t, and the spatial coordinates, x and y, are used to address a memory in which the detection events are accumulated. Thus, in the memory the distribution of the photon density over x, y, and t builds up. The result is a data array representing the pixel array of the scan, with every pixel containing a large number of time channels with photon numbers for consecutive times after the excitation pulse. In other words, the result is an image that contains a fluorescence decay curve in each pixel [27, 28]. An example is shown in Fig. 9.

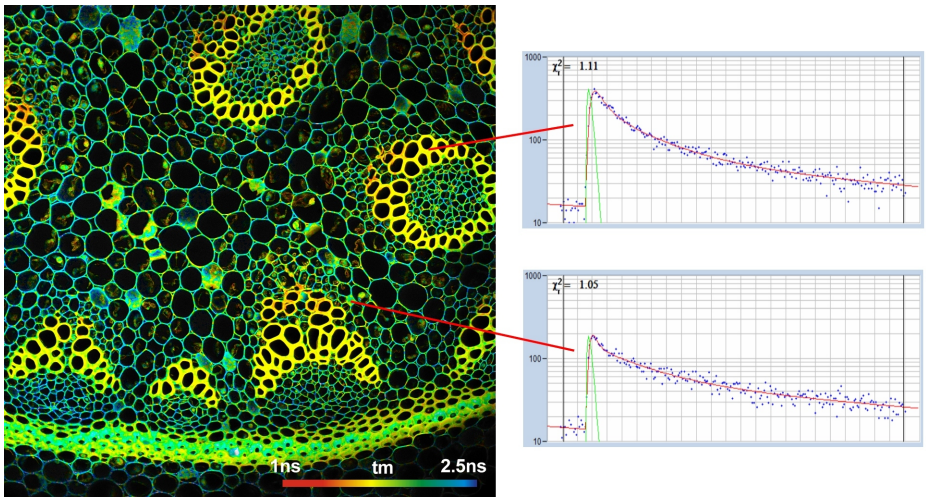


Fig. 9: FLIM image of a Convallaria Sample, 2048x2048 pixels. Every pixel contains a fluorescence decay curve resolved in a large number of time channels.

The recording process works at near-ideal photon efficiency and at extremely high time resolution. Importantly, it delivers the complete temporal profile of the decay functions, not only an average fluorescence lifetime [28, 40, 94, 122]. This is extremely important for biological applications, where the information is in the composition of the multi-exponential decay rather than in a simple 'lifetime'.

The TCSPC module can also process the photon data to obtain fluorescence-correlation data (FCS) data [37, 29], photon counting histograms (PCH) or photon-counting-lifetime histograms. Moreover the 'parameter-tagged' single photon data can be stored in a file for off-line processing by single-molecule spectroscopy techniques [163, 212].

It should be explicitly noted that FLIM by multi-dimensional TCSPC does not require that the scanner stays in one pixel until enough photons for a full fluorescence decay curve have been acquired. It is only necessary that the *total pixel time*, over a large number of subsequent frames, is large enough to record a reasonable number of photons per pixel. Thus, TCSPC FLIM works even at the highest scan rates available in laser scanning microscopes. At the pixel rates used in practice, the recording process is more or less random: A photon is just stored in a memory location according to its time in the fluorescence decay, its detector channel number, and the location of the laser spot in the sample in the moment of detection.

Standard bh FLIM systems have two parallel channels of the architecture shown in Fig. 8. The systems are therefore able to simultaneously record images in two spectral channels. Because the channels are parallel the systems thus deliver high throughput rates. Another advantage is that the channels are independent. If one channel overloads the other one still delivers correct data. Please see [6] and [37] for details.

*Excitation-Wavelength Multiplexing*

It often happens that a sample contains two fluorophores which need to be excited at different wavelengths, either because the excitation spectra are too different, or because the emission cannot be cleanly separated if both are excited at the same wavelength [37]. A typical example is metabolic FLIM by recording signals from NAD(P)H and FAD [43, 44]. In principle, images of the two fluorophores could be recorded one after another. However, biological systems are dynamic, therefore it is desirable to record both images simultaneously. The bh FLIM systems use excitation-wavelength multiplexing for this task. The principle is shown in Fig. 10. Two lasers, Laser 1 and Laser 2, are multiplexed synchronously with the pixels, lines, or frames of the scan. The TCSPC modules receive information which of the lasers was active in the moment when a photon was detected. The modules then build up separate FLIM images for the two lasers. With two TCSPC modules and two detectors detecting in different spectral windows four images for different combinations of excitation and emission wavelength are obtained. In practice not all of these combinations may contain relevant data. Important is that the separation of the signals is near-ideal. Temporal overlap of the decay functions of the fluorophores as it occurs in pulse-by-pulse interleaved excitation does not exist. An example for the recording of a DAPI image simultaneously with an Alexa 488 image is shown in Fig. 11.

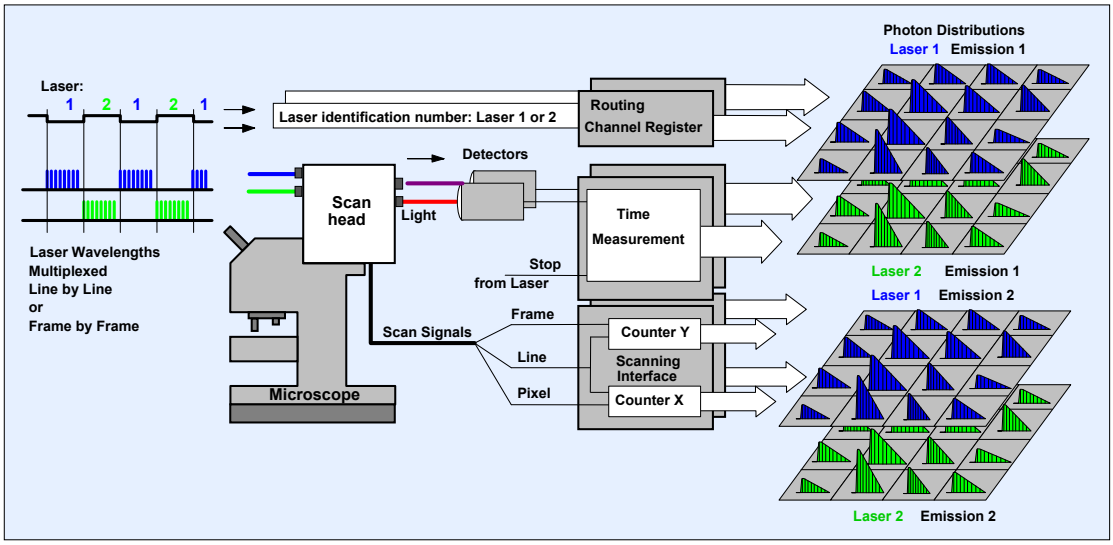


Fig. 10: Excitation wavelength multiplexing. With two lasers and two TCSPC channels four images for different combinations of excitation and emission wavelength are obtained.

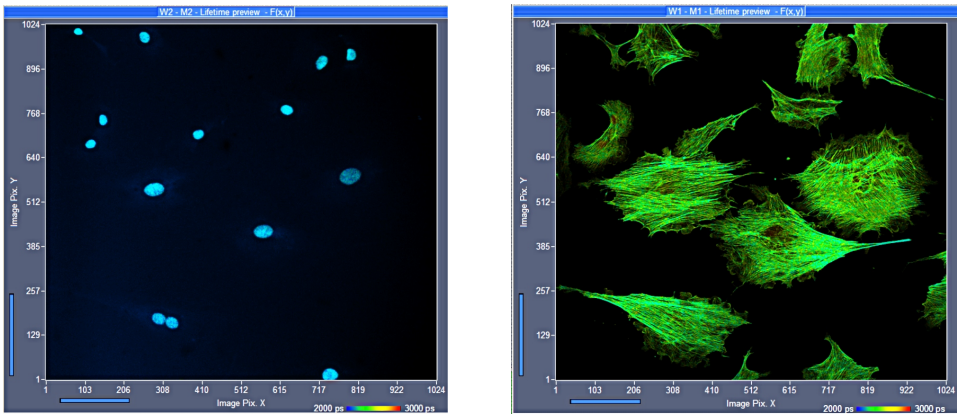

Fig. 11: BPAE sample with DAPI and Alexa 488, excited by multiplexed lasers at 405 nm (left) and 488 nm (right).

*Spatial Mosaic FLIM*

Originally, bh introduced Mosaic FLIM to record large images with the 'Tile Imaging' function of laser scanning microscopes [6, 37]. The microscope scans the sample, and performs a raster stepping ('Tile stepping') of the sample. For every step the sample is scanned for a defined number of frames. The TCSPC device records the data by its normal FLIM procedure. However, the memory is configured to provide space not only for a single image of the defined frame format but for the entire mosaic of images of the tile stepping. The TCSPC FLIM process starts in the first mosaic element. After a defined number of frames the recording proceeds to the next mosaic element. Provided the number of frames per tile of the microscope stepping and the number of frames per mosaic elements are the same the TCSPC module records the entire tile array into a single photon distribution. The recorded photon distribution represents a FLIM image of the entire array. The process is also applicable to Z stack recording. In this case the transition to the next mosaic element is associated to the transition to the next focal plane. The TCSPC FLIM process of Mosaic FLIM is illustrated in Fig. 12., two examples are shown in Fig. 13.

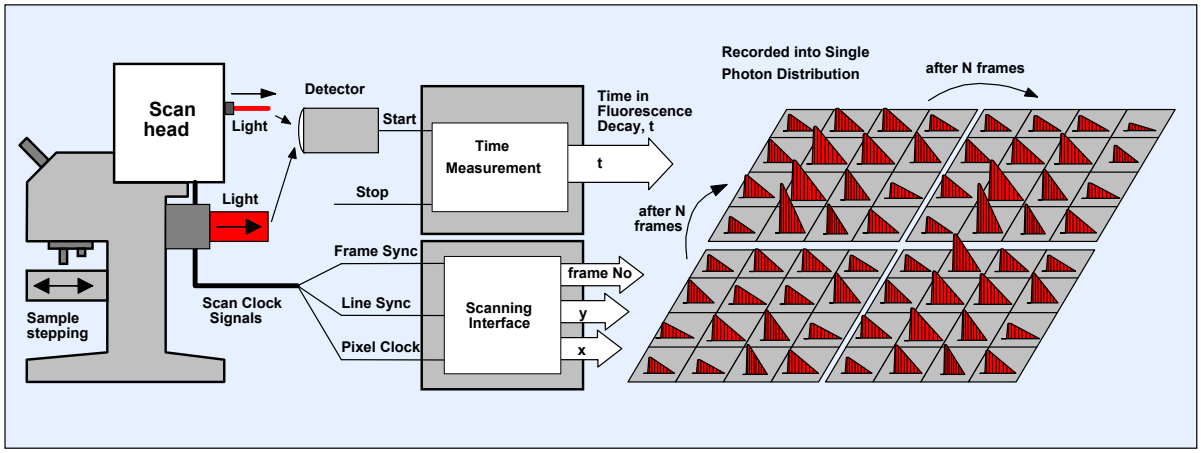


Fig. 12: Mosaic FLIM, recording of a X-Y mosaic

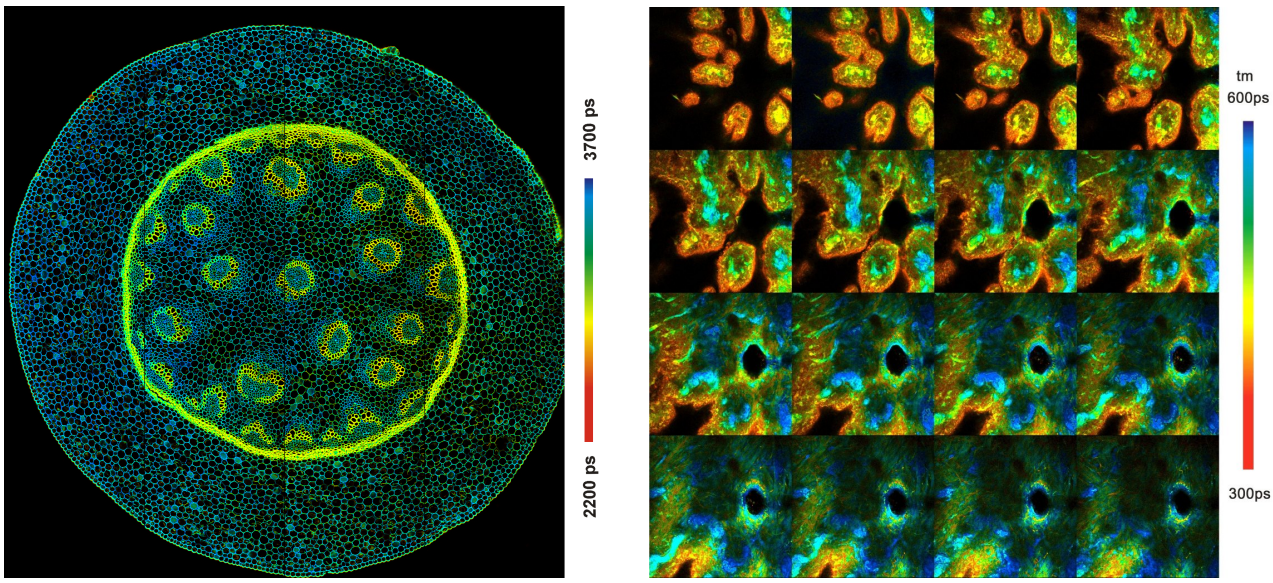


Fig. 13: Left: Mosaic FLIM of a convallaria sample. Right: Z Stack FLIM of Pig skin stained with ICG.

*Temporal Mosaic FLIM*

The idea that Mosaic FLIM records several images into one photon distribution leads to a more general concept of Mosaic FLIM: The transition from one mosaic element in the FLIM data to the next can be associated also to a change in another parameter of the experiment. An example is temporal mosaic FLIM. The sample is repeatedly scanned around the same spatial position, but subsequent images are recorded in consecutive elements of the FLIM mosaic. The result is a time series, the time step of which is a multiple of the frame time [37].

Compared to conventional time-laps recording the temporal mosaic FLIM has several advantages: No time has to be reserved for the save operations, and the data can be better analysed with global-parameter fitting. The biggest advantage is, however, that mosaic time series data can be accumulated: A sample would be stimulated repeatedly by an external event, and the start of the mosaic recording be triggered with the stimulation. With every new stimulation the recording procedure runs through all elements of the mosaic, and accumulates the photons. Accumulation allows data to be recorded without the need of trading photon number and lifetime accuracy against the speed of the time series.

Consequently, the time per step (or mosaic element) is only limited by the minimum frame time of the scanner.

Temporal Mosaic FLIM is thus an excellent way to investigate fast physiological processes in live systems [89, 88]. An example for recording $Ca^{2+}$ transients in live neurons is shown in Fig. 14. Please see [37] for more information.

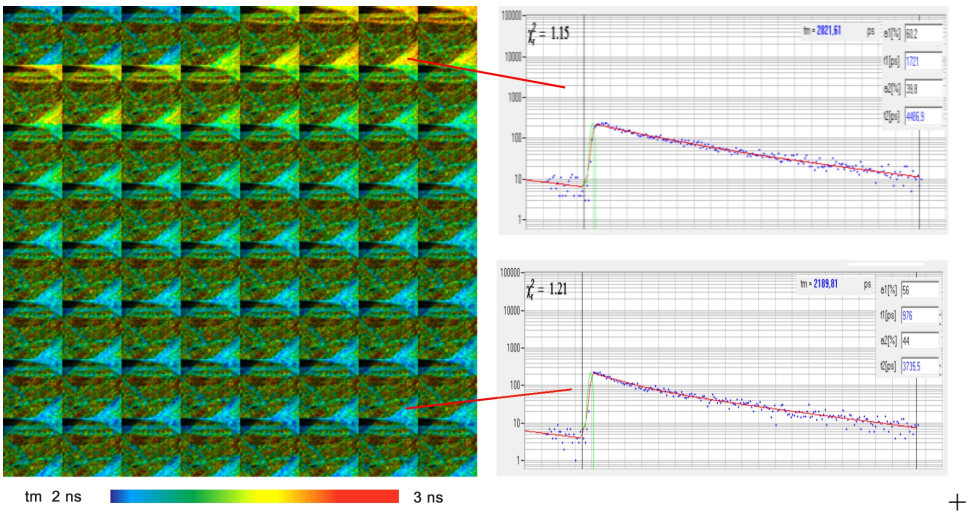


Fig. 14: $Ca^{2+}$ transient in cultured neurons, incubated with Oregon Green Bapta. Electrical stimulation, stimulation period 3s, data accumulated over 100 stimulation periods. Time per mosaic element is 38 ms.

*Multi-Wavelength FLIM*

The principle shown in Fig. 8, page 8, can be extended to simultaneously detect in 16 wavelength channels. The optical spectrum of the fluorescence light is spread over an array of 16 detector channels. The TCSPC system determines the detection times, the channel numbers in the detector array, and the position, x, and y, of the laser spot for the individual photons. These pieces of information are used to build up a photon distribution over the time of the photons in the fluorescence decay, the wavelength, and the coordinates of the image [25, 28, 37, 30]. The principle of multi-wavelength FLIM is shown in Fig. 15.

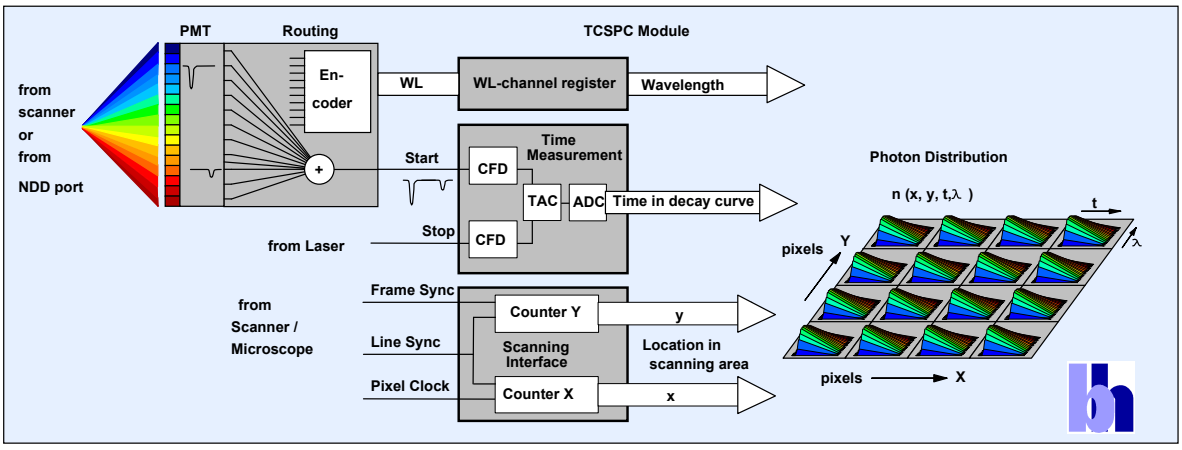


Fig. 15: Principle of Multi-Wavelength TCSPC FLIM

As for single-wavelength FLIM, the result of the recording process is an array of pixels. However, the pixels now contain several decay curves for different wavelength. Each decay curve contains a large

number of time channels; the time channels contain photon numbers for consecutive times after the excitation pulse. An example is shown in Fig. 16.

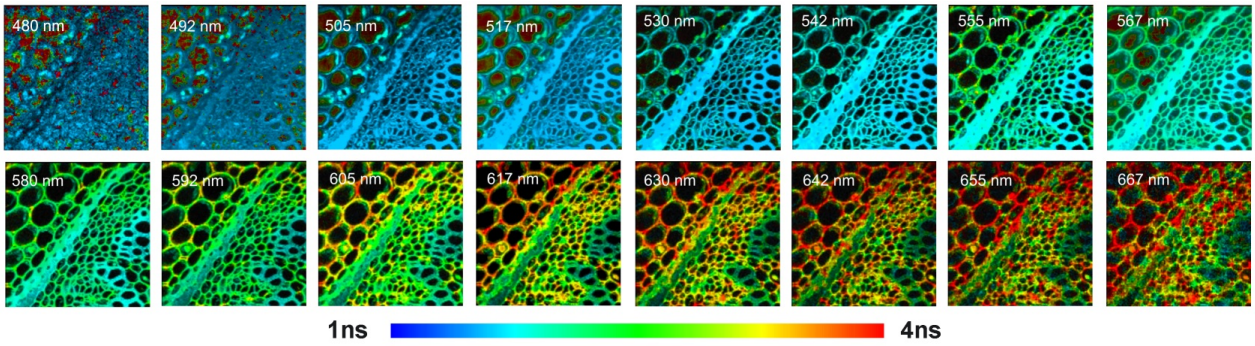


Fig. 16: Multi-wavelength FLIM of a *convallaria* sample

## Optical Architecture of the LSM 710 / 780 / 880 / 980 FLIM Systems

All bh TCSPC FLIM systems have in common that the sample is excited by a pulsed laser of high repetition rate, scanned at high pixel rate by the optical scanner of the microscope, and that the fluorescence light is detected by one or several fast photon counting detectors connected to the microscope. The FLIM data are recorded by building up a photon distribution over the times of the photons in the laser pulse period and the positions of the laser beam in the moment of the photon detection. Typical FLIM configurations for the LSM 710/780/880/980 family microscopes are shown in Fig. 17, Fig. 18 and Fig. 19.

Fig. 17 shows FLIM configurations for inverted microscopes. The configuration on the left uses multiphoton excitation by a femtosecond titanium-sapphire laser for excitation. The fluorescence light is detected via a non-descanned detection (NDD) beam path. Typically, the light is split in two spectral components by a Zeiss 'T Adapter', and detected by two parallel detectors and TCSPC channels. The configuration shown on the right uses picosecond diode lasers. The sample is excited by one-photon excitation. The fluorescence light is detected back through the confocal beam path of the scanner and sent out of the scan head via an optical port. It is split into two spectral channels by a bh beamsplitter module and fed into two FLIM detectors. The single-photon pulses from the detectors are recorded by two separate TCSPC channels of the FLIM system.

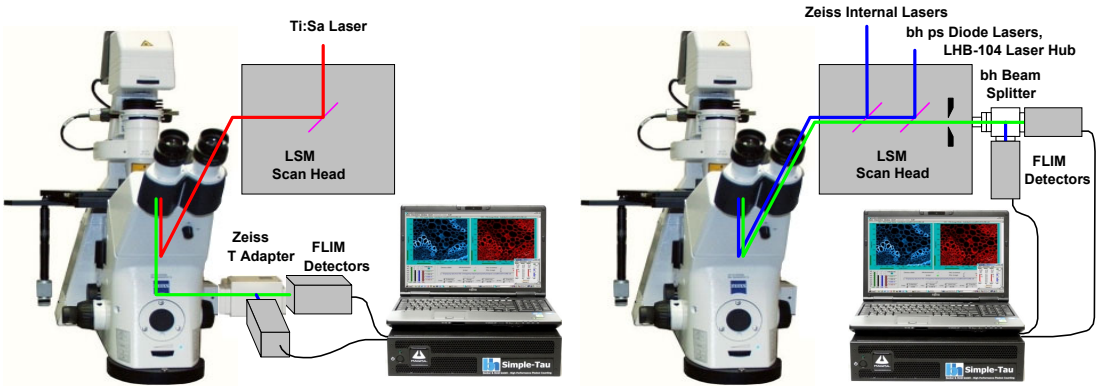


Fig. 17: LSM 710/780 family FLIM systems, inverted microscopes. Left: Multiphoton-excitation FLIM with non-descanned detection. Right: One-photon FLIM with confocal detection.

The detectors and detector assemblies for the confocal port are compatible with those for the NDD port. That means the detectors can be moved between the two port. It is also possible to attach detectors to the both ports permanently. The desired pair of detectors can then be selected from the SPCM data acquisition software.

Fig. 18 shows FLIM at an LSM 710/780/880/980 in the upright version. The configuration on the left uses multiphoton excitation and non-descanned detection, the configuration on the right uses one-photon excitation and confocal detection.

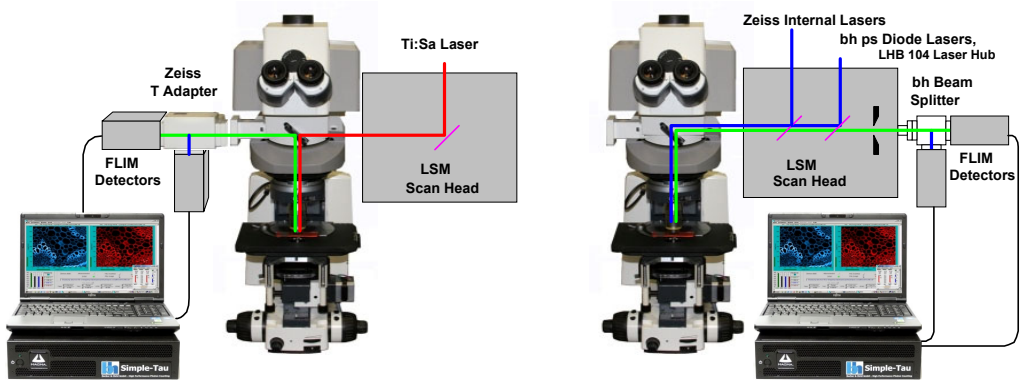


Fig. 18: LSM 710/780/880/980 family FLIM systems, upright microscopes. Left: Multiphoton-excitation FLIM with non-descanned detection. Right: One-photon excitation FLIM with confocal detection.

Multiphoton and the one-photon FLIM configurations for the LSM 880 and LSM 980 with Airy-Scan detectors are shown in Fig. 19, left and right. For the multiphoton system there is no difference to the standard system. The Airy-Scan detector rests at the confocal port and does not interfere with the FLIM detectors at the NDD port. In the one-photon FLIM system the FLIM detectors are connected to a beam switch between the scan head and the Zeiss Airy-Scan detector, see Fig. 19, right.

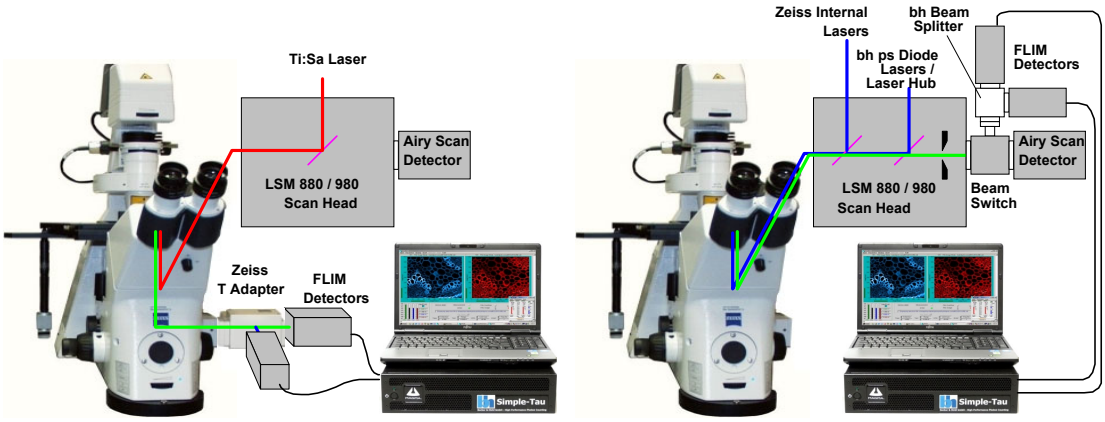


Fig. 19: LSM 880 / 980 FLIM systems, inverted microscopes. Left: Multiphoton-excitation FLIM with non-descanned detection. Right: One-photon excitation FLIM with confocal detection.

Standard bh FLIM systems for the LSM 710, 780, 880, and 980 use the bh HPM-100-40 or -06 hybrid detectors [37, 31]. However, the bh systems work also with the Zeiss BIG 2 detector [15, 37], with the NIR versions of the HPM-100 detectors [13, 14, 39], and with the bh MW-FLIM GaAsP multi-spectral FLIM detectors [37]. The optical configuration for multiphoton multi-wavelength FLIM is shown in Fig. 20. The light is collected from an NDD port by a fibre bundle. The light is dispersed spectrally, and detected by a bh PML-16 GaAsP (16-channel) PMT module. Similarly, the multi-wavelength FLIM detector assembly can be attached to the confocal port of the scan head.

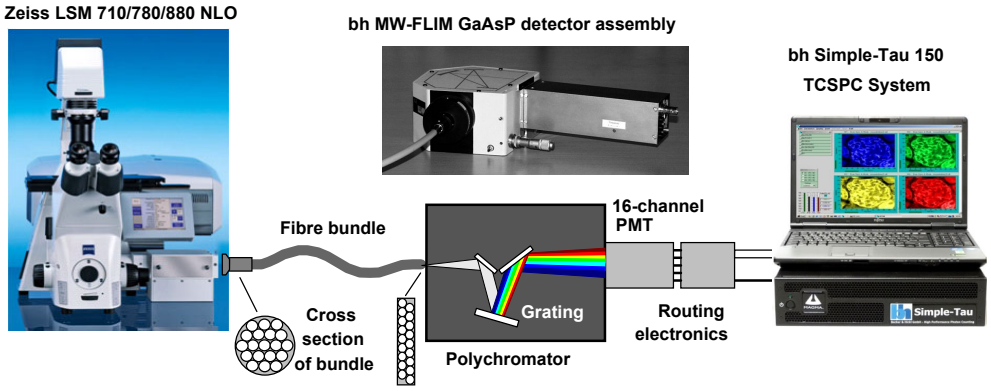


Fig. 20: Multi-wavelength FLIM

## FL IM Functions in Brief

*Data Acquisition Software*

The FLIM systems for the Zeiss LSM 710/780 family use the SPCM data acquisition software. Since 2013 the SPCM software is available in a 64-bit version. SPCM 64 bit exploits the full capability of Windows 64 bit, resulting in faster data processing, capability of recording images of extremely large pixel numbers, and availability of additional multi-dimensional FLIM modes [12, 37, 193]. The bh SPCM software and the Zeiss ZEN software are operated via the same keyboard and the same mouse.

The main panel of the SPCM data acquisition software is configurable by the user [37]. Four configurations for FLIM systems are shown in Fig. 21. During the acquisition the SPCM software displays intermediate results in predefined intervals, usually every few seconds. The acquisition can be stopped after a defined acquisition time or by a user commend when the desired signal-to-noise ratio has been reached [6, 37]. Frequently used operation modes and user interface configurations are selected from a panel of predefined setups.

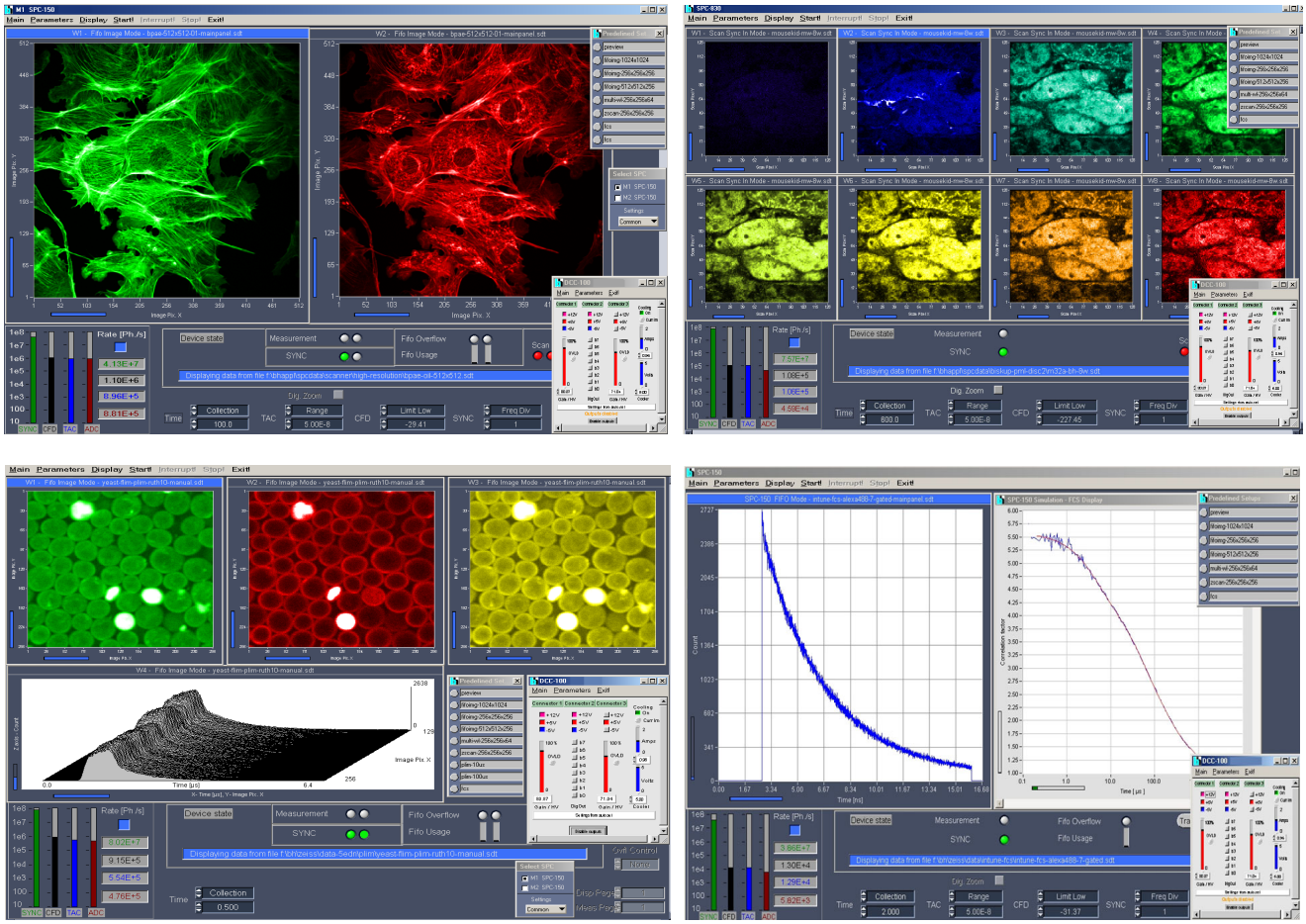

Fig. 21: SPCM software panel. Top left to bottom right: FLIM with two detector channels, multi-spectral FLIM, combined fluorescence / phosphorescence lifetime imaging (FLIM/PLIM), fluorescence correlation (FCS).

*FLIM Data Acquisition*

From the user point of view, FLIM in a laser scanning microscope is performed by the same general procedures as steady-state imaging. First, the sample is brought in focus by looking through the eyepieces and manually turning the microscope focus buttons. Then a fast repetitive scan is run in which the FLIM system displays fast preview images. While observing these images, the exact location and size of the scan area are selected, and the focal plane is fine-adjusted. Then an appropriate FLIM mode is selected, and the final FLIM acquisition is started.

*Fast preview function*

When FLIM is applied to live samples the time and the sample exposure needed for positioning, focusing, laser power adjustment, and selection of the scan region has to minimised. Therefore, the FLIM systems have a fast preview function. The preview function displays images in intervals on the order of 1 second and less, see Fig. 22.

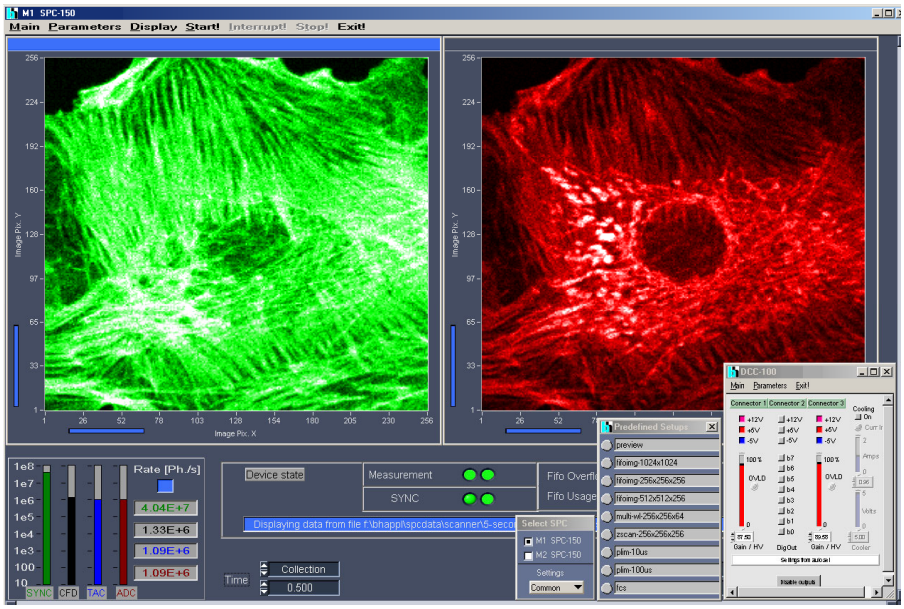


Fig. 22: SPCM software in fast preview mode. 1 second per image. Two parallel FLIM channels recording in separate wavelength intervals.

Whatever you change in the microscope: The position of the samples, the scan area, the zoom factor, the focal plane, pinhole size or the laser power - the result becomes immediately visible in the preview images, see Fig. 23.

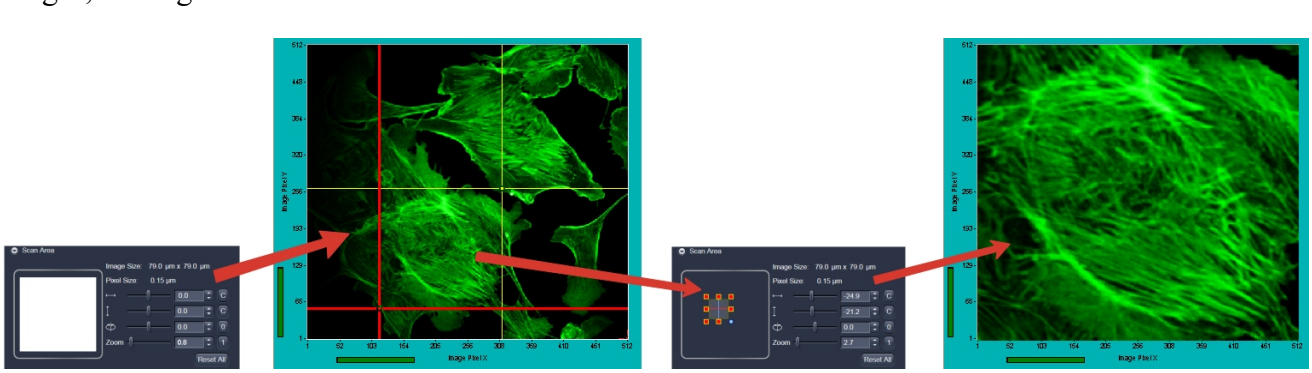

Fig. 23: When the scan area definition in the Zeiss ZEN software is changed the result is shown in the images immediately.

*Easy Switching Between Acquisition Modes and User Interface Configurations*

Frequently used operation modes and user interface configuration can be selected from a panel of predefined setups. Switching between Preview modes, FLIM acquisition, different pixel and time-channel numbers, time-series recording, Z-stack recording, FCS, or any other conceivable recording procedure is a matter of a single mouse click, see Fig. 24.

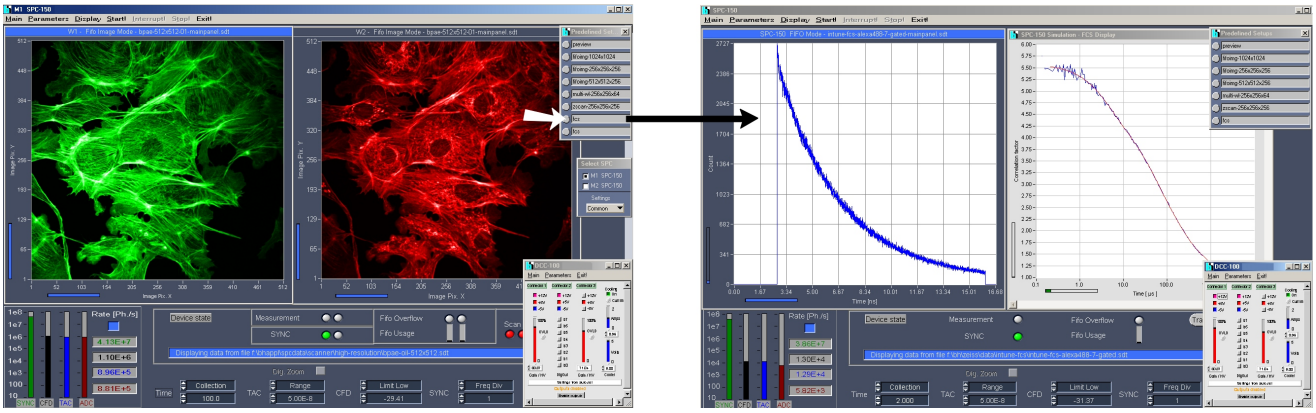

Fig. 24: Switching the instrument configuration via the 'Predefined Setup' panel

*Fast Beam Scanning - Fast Acquisition*

The bh FLIM systems are perfectly compatible with the fast beam scanning used in the Zeiss LSM 710/780/880/980 family microscopes. Frame times can be from less than 50 ms to a few seconds, with pixel dwell times down to less than one microsecond. The multi-dimensional TCSPC process used in the bh FLIM systems delivers identical results for different scan rates, provided the total acquisition time is the same. FLIM can be acquired at short acquisition time. Fig. 25 shows lifetime images of a BPAE cell recorded within 5 seconds acquisition time.

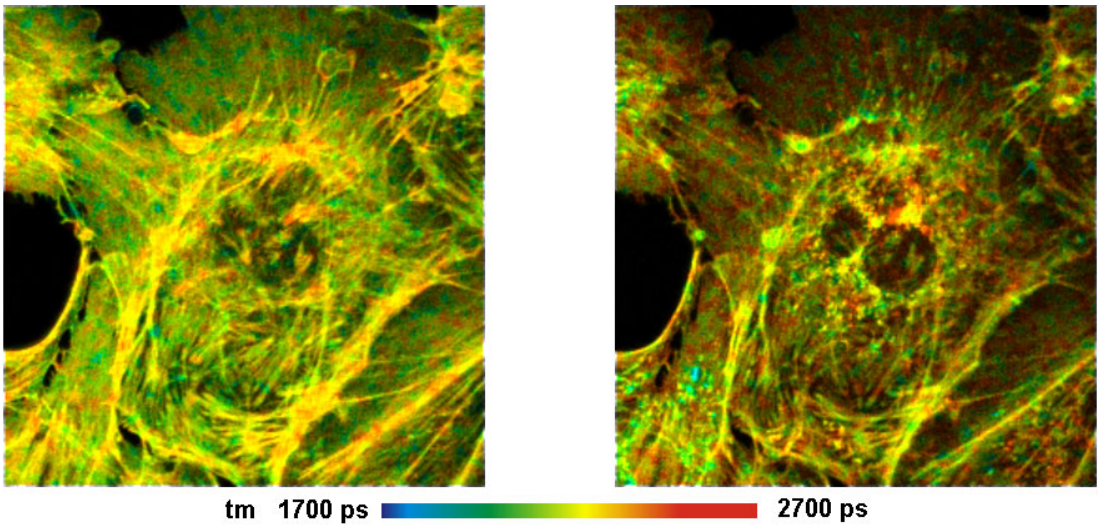


Fig. 25: FLIM acquired within 5 seconds of acquisition time. Left 485 to 560 nm, right 560 to 650 nm. BPAE cell stained with Alexa 488 and Mito Tracker Red.

Acquisition at high scan rate is also the basis of the fast preview mode (see above) and of fast FLIM time-series recording. Time-series can be recorded as fast as two images per second [37, 119], with temporal mosaic FLIM and triggered accumulation even faster. Fig. 26 shows time-series FLIM of an amoeba. The images are 0.4-second snapshots taken very one second.

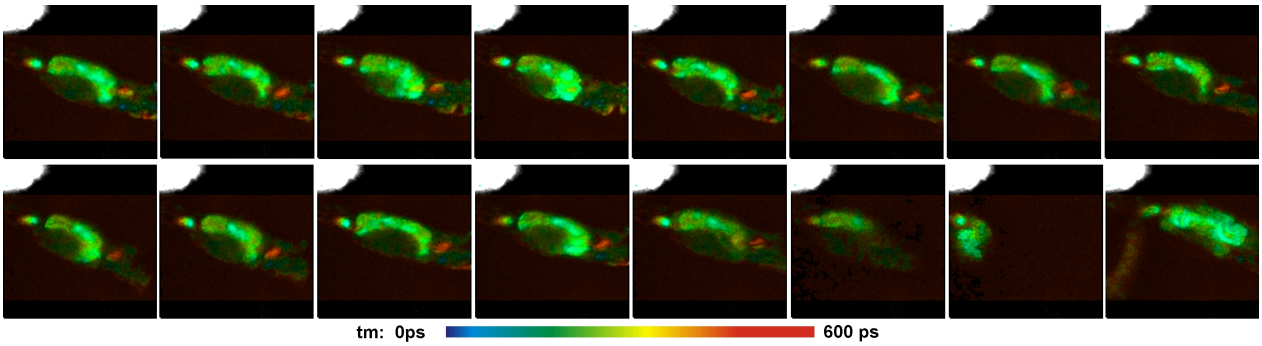


Fig. 26: Moving amoeba. Autofluorescence, acquisition time 0.4 s, image rate 1 image per second.

### *Online FLIM Display*

Starting from Version 9.72 SPCM software the FLIM systems for the Zeiss LSM 710 / 780 / 880 / 980 family are able to display lifetime images online, both during the accumulation of FLIM data and for the individual steps of a fast image sequence. An example is shown in Fig. 27. The calculation of the lifetime images is based on the first moment of the decay data in the pixels of the images [37]. The first-moment technique combines short calculation times with near-ideal photon efficiency. It does not require to reduce the time resolution (time channels per pixel) to obtain high image rates. Even if the fast online lifetime function is used during the FLIM acquisition the data can later be processed by precision SPCImage multi-exponential data analysis.

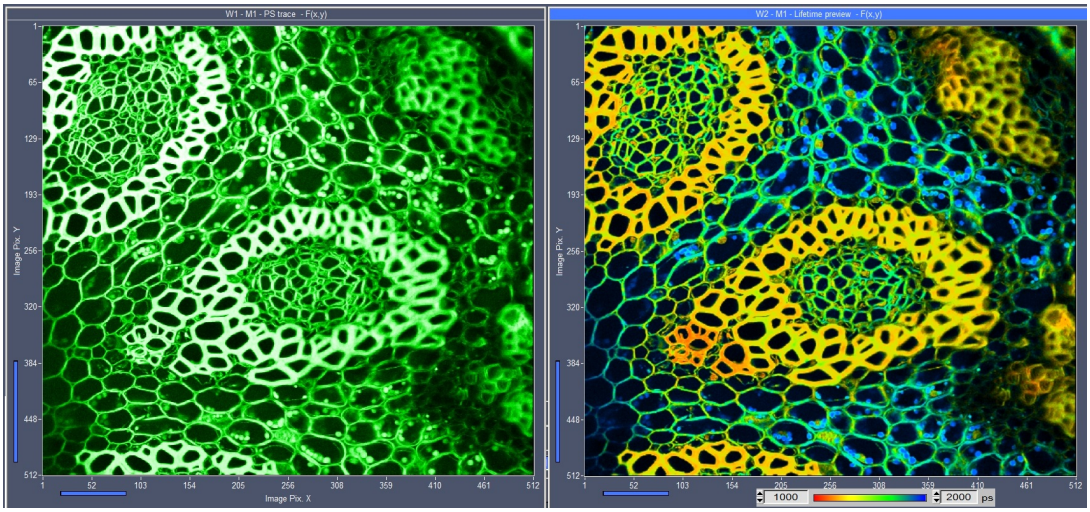


Fig. 27: Intensity image (left) and online lifetime image (right) calculated online by SPCM software

### *Bi-Directional Scanning*

With Version 9.73 SPCM Software, the bh TCSPC / FLIM systems support the bidirectional scanning function of the Zeiss LSMs. As usual, data recording is synchronised with the scanning by frame clock, line clock, and pixel clock pulses from the scanner. Each first line clock pulse indicates the beginning of a forward scan, each second one the beginning of a backward scan. The recording procedure automatically reverses the data from the backward scan and compensates for the line shift caused by the dynamic behaviour of the scanner. The FLIM data structure is the same as for unidirectional scanning. Thus, standard online intensity and lifetime display functions of the SPCM software are available, and data can be analysed by SPCImage as usual [37].

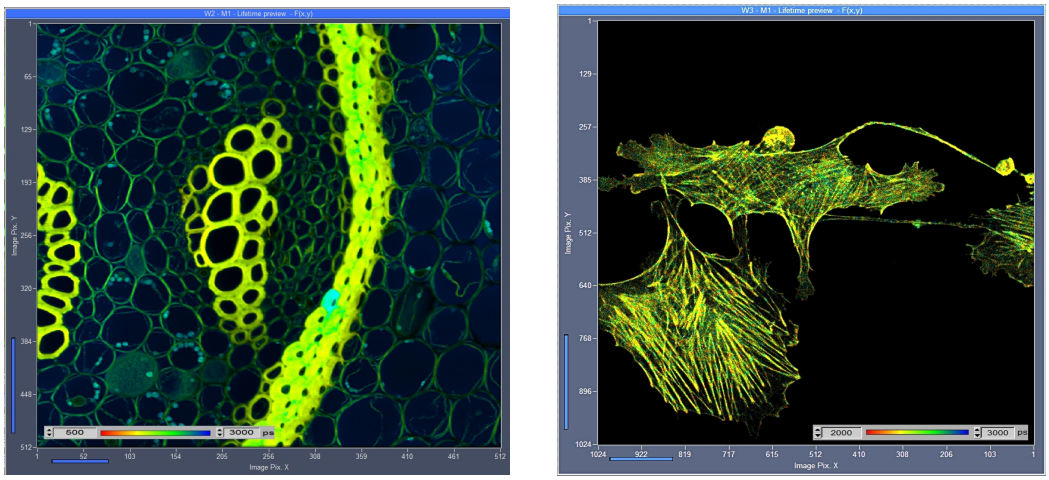

Fig. 28: FLIM of Convallaria sample (left, 512x512 pixels) and BPAE Cell sample (right, 1024x1024 pixels), recorded with bidirectional scanning. Images created by online-lifetime function of SPCM software.

*Megapixel FLIM Images*

With bh's megapixel technology, pixel numbers can be increased up to 2048 x 2048 while maintaining a temporal resolution of 256 time channels. Thus, the useful pixel resolution is rather limited by the optical resolution and the maximum field of view of the microscope lens than by the capabilities of the bh FLIM system. By using the 'Mosaic FLIM' option, the useful pixel number can be increase even beyond the capabilities of the microscope lens, see page 30. Alternatively, the number of time channels can be increased up to 1024 for images of 1024x1024 pixels, and up to 4096 for images of 512x512 pixels or less.

Fig. 29 shows a FLIM image of a BPAE sample recorded at a resolution of 1024 x 1024 pixels. The image on the left shows the entire area of the scan. The image on the right is a zoom into the data shown left.

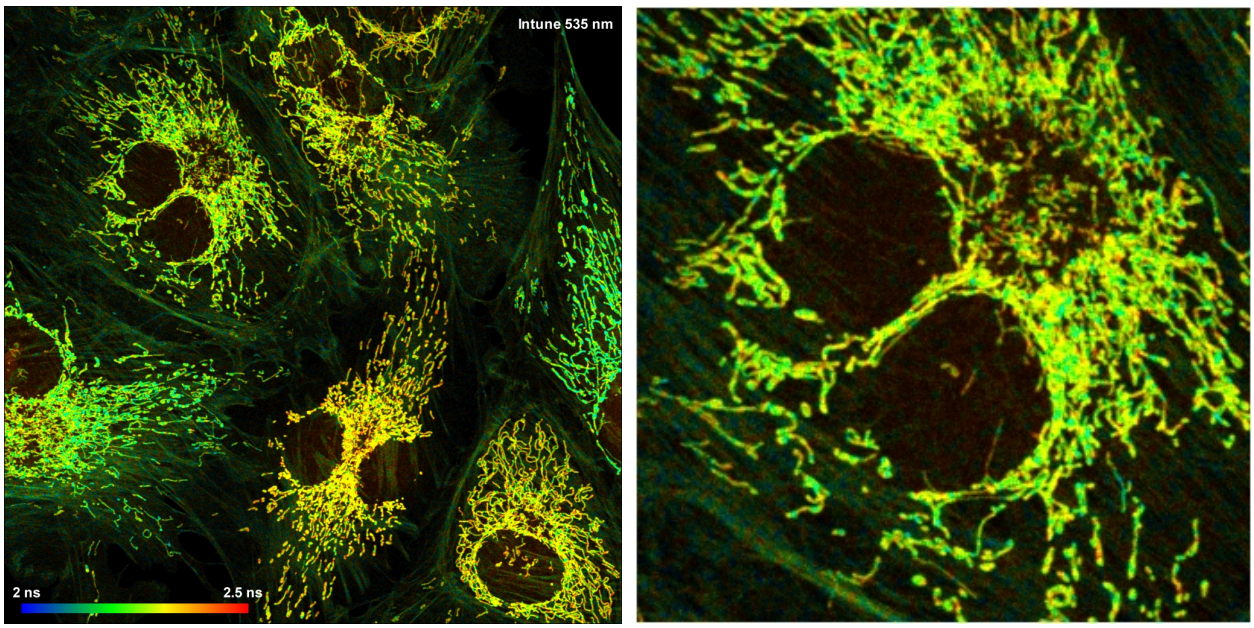


Fig. 29: Left: Image recorded with 1024 x 1024 pixels. Right: Digital zoom into the data of Fig. 29, showing the two cells on the upper left.

Large pixel numbers are important especially for tissue imaging. They are also useful in cases when a large number of cells have to be investigated and the FLIM results to be compared. Megapixel FLIM records images of many cells simultaneously, and under identical environment conditions. Moreover, the data are analysed in a single analysis run, with identical IRFs and fit parameters. The results are therefore exactly comparable for all cells in the image area.

*Two fully parallel TCSPC FLIM Channels*

Standard bh FLIM systems record in two wavelength intervals simultaneously. The signals are detected by separate detectors and processed by separate TCSPC modules [37]. There is no intensity or lifetime crosstalk. Even if one channel overloads the other channel is still able to produce correct data.

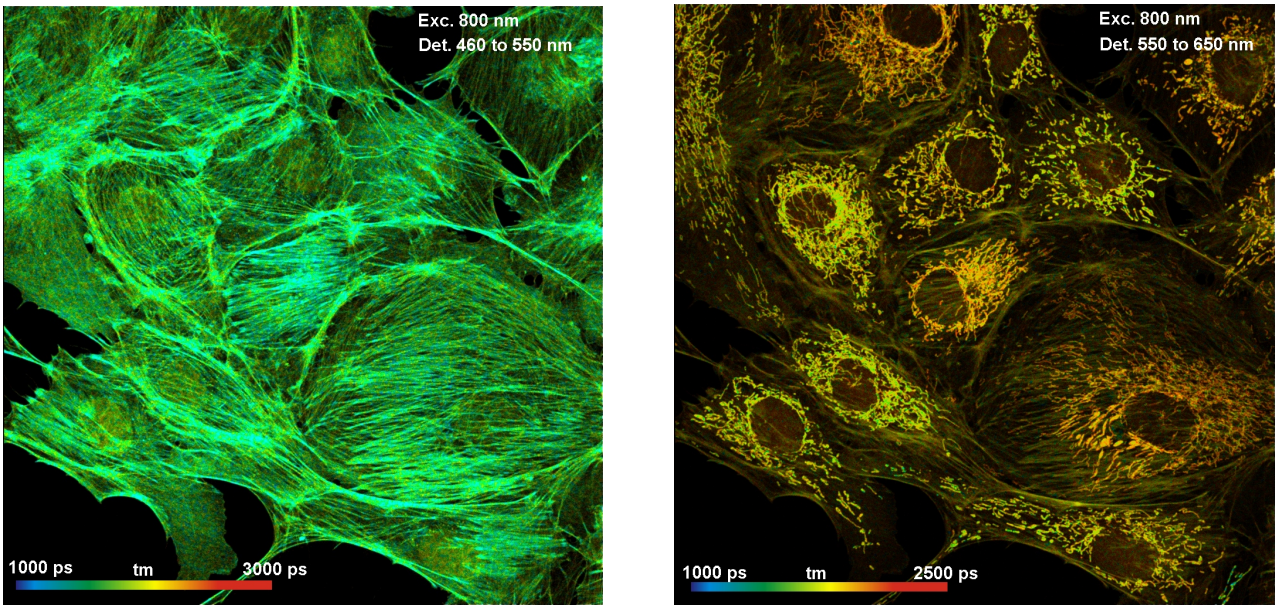


Fig. 30: Dual-channel detection. BPAE cells stained with Alexa 488 phalloidin and Mito Tracker Red. Left: 460 nm to 550 nm. Right: 550 nm to 650 nm.

*Laser Wavelength Multiplexing*

FLIM systems using the bh 'Laser Hub' can be operated in a fast excitation-wavelength multiplexing mode. Multiplexing can be performed frame-by frame, line by line, or even pixel by pixel. The advantage over pulse-interleaved excitation (PIE) is that there is absolutely no overlap between the multiplexing phases. Consequently, there is no intensity or lifetime crosstalk between signals excited by different wavelength. An example is shown in Fig. 31.

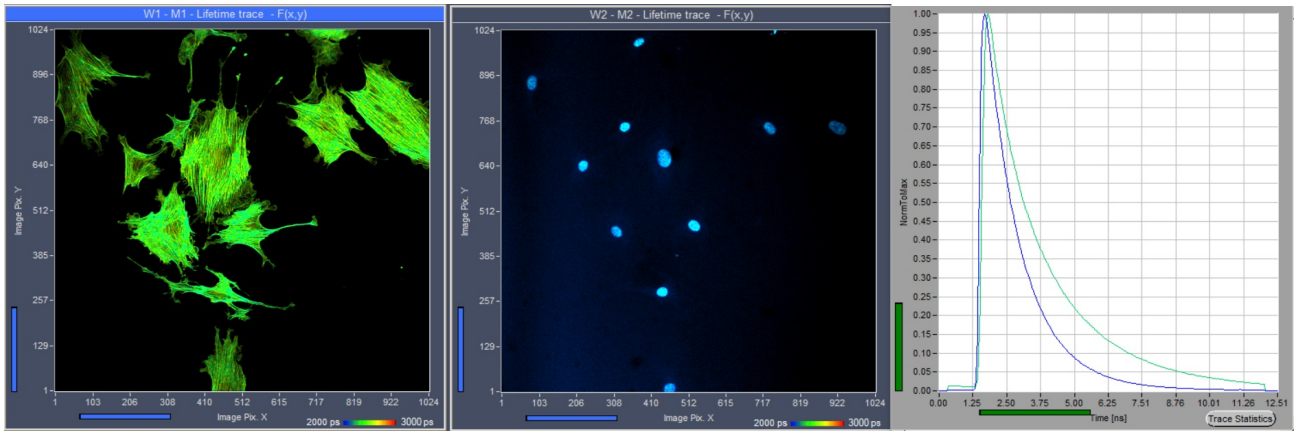


Fig. 31: FLIM with laser-wavelength multiplexing, 480 nm and 405 nm, Alexa 488 and DAPI. LSM 980 confocal system with bh LHB104 laser hub

*Multiphoton NDD FLIM: Clean Images from Deep Tissue Layers*

The bh Multiphoton FLIM systems use the non-descanned detection (NDD) path of the LSM 710/780/880 NLO family microscopes. With non-descanned detection, fluorescence photons scattered on the way out of the sample are detected far more efficiently than in a confocal system. The result is that clear images are obtained from deep tissue layers. An example is shown in Fig. 32. The images show a pig skin sample exited by two-photon excitation at 800 nm. The left image shows the wavelength channel below 480 nm. This channel contains both fluorescence and SHG signals. The SHG fraction of the signal has been extracted from the FLIM data and displayed by colour. The right image is from the channel >480 nm. It contains only fluorescence, the colour corresponds to the amplitude-weighted mean lifetime of the multi-exponential decay functions.

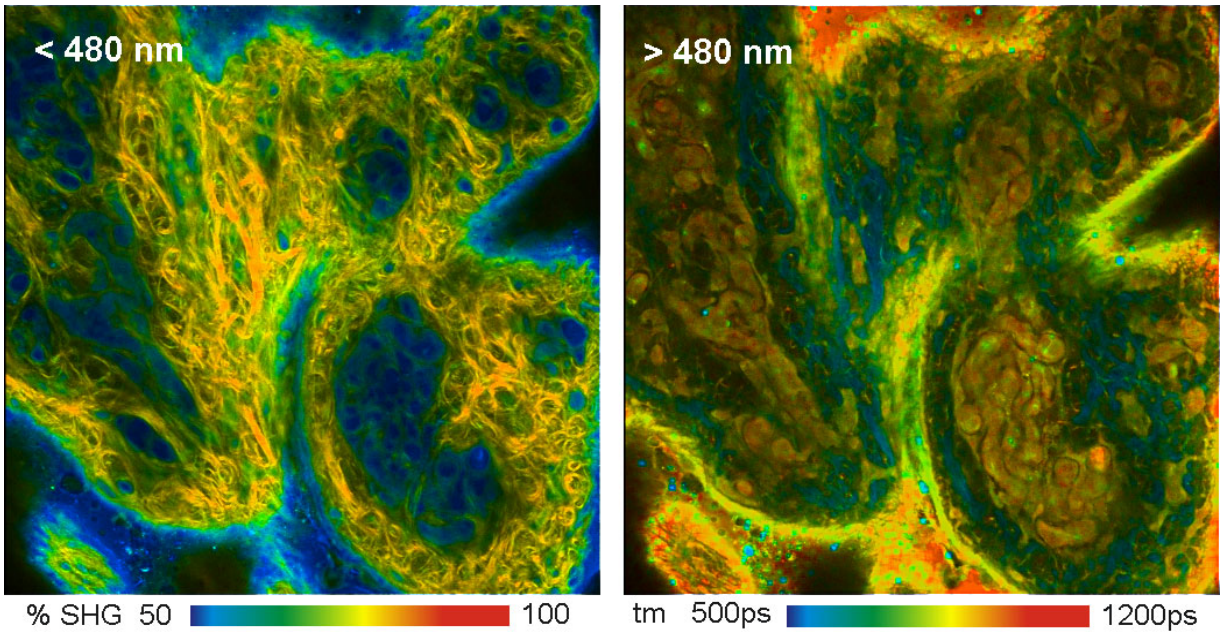


Fig. 32: Two-photon FLIM of pig skin. LSM 710 NLO, HPM-100-40, NDD. Left: Wavelength channel <480nm, colour shows percentage of SHG. Right: Wavelength channel >480nm, colour shows amplitude-weighted mean lifetime.

*FLIM with Ultra-Fast Detectors*

The instrument-response function of a multiphoton FLIM system with HPM-100-06 detectors has a full-width at half maximum (FWHM) of less than 20 ps [18, 37]. The fast response greatly improves the accuracy at which fast decay components can be extracted from a multi-exponential decay. Applications are mainly in the field of metabolic FLIM, which requires separation of the decay components of bound and unbound NADH, and in the range of FRET, which requires the separation of interacting and non-interacting donor components. An NADH FLIM image recorded with an ultra-fast FLIM system on a Zeiss LSM 880 NLO is shown in Fig. 32. Images of the images of the amplitude ratio, a1/a2 (unbound/bound ratio), and of the fast (t1, unbound NADH) and the slow decay component (t2, bound NADH) are shown in Fig. 34.

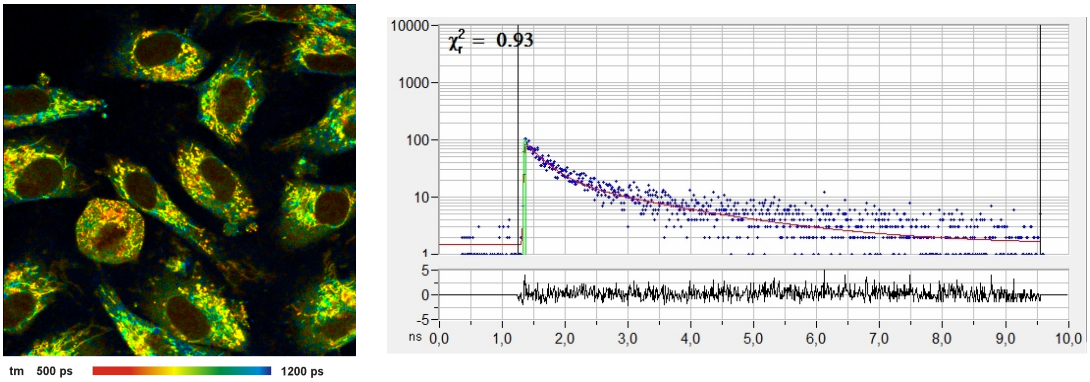


Fig. 33: Left: NADH Lifetime image, amplitude-weighted lifetime of double-exponential fit. Right: Decay curve in selected spot, 9x9 pixel area. FLIM data format 512x512 pixels, 1024 time channels. The IRF width is 19 ps, the time-channel width 10ps.

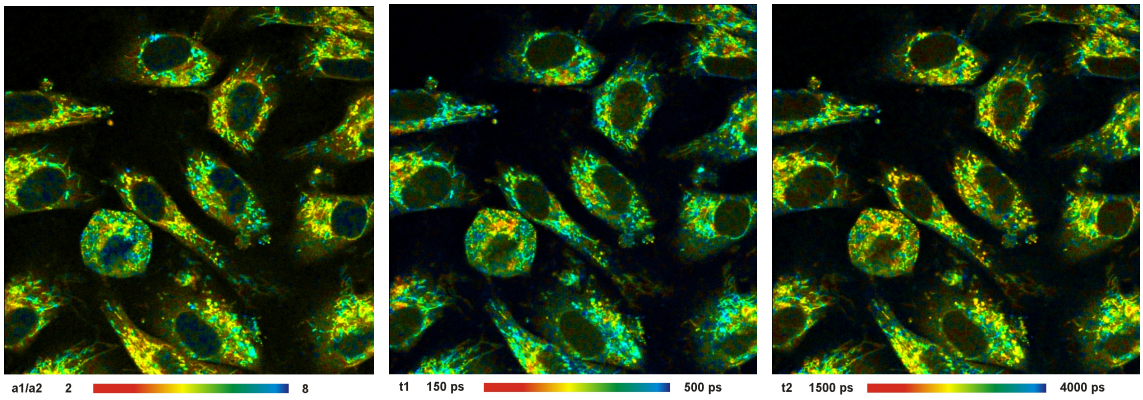


Fig. 34: Left to right: Images of the amplitude ratio, a1/a2 (unbound/bound ratio), and of the fast (t1, unbound NADH) and the slow decay component (t2, bound NADH). FLIM data format 512x512 pixels, 1024 time channels. Time-channel width 10ps.

Fig. 35 shows mushroom spores of *Cortinarius Mucosus*. An image of the amplitude-weighted lifetime, tm, is shown on the left, a decay curve on the right. tm is in the range from 20 to 40 ps, the lifetime of the fast component, t1, in the range from 10 to 20 ps. No other FLIM system is able to show such fast decay processes directly.

Ultra-fast decays in biological material are more frequent than commonly believed. Similarly fast decay components were found in other mushroom spores [45], in pollen grains [46], and in human hair. Ultra-fast fluorescence decay times should therefore no longer be put aside as a peculiarity but seriously considered as a potential source of biological information.

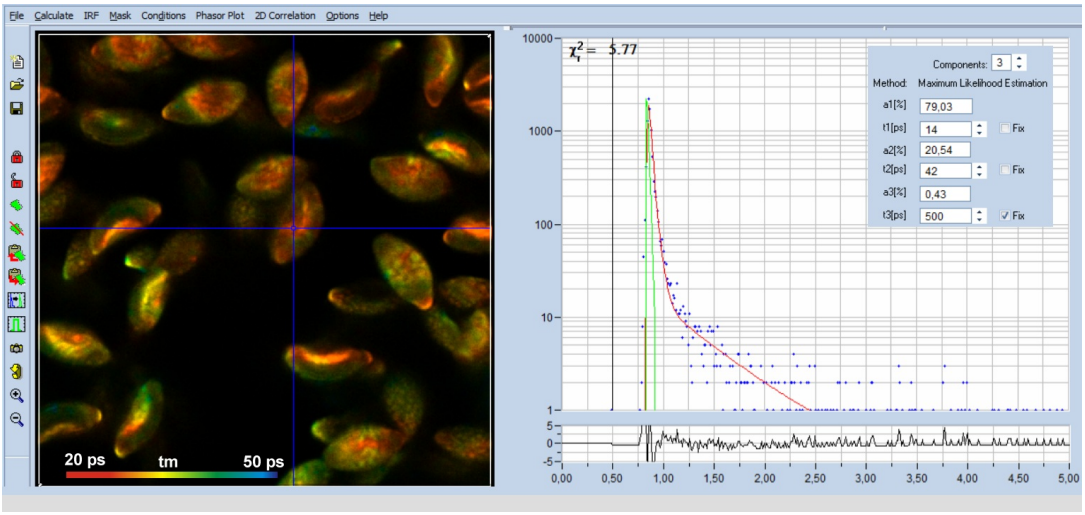


Fig. 35: Mushroom spores, *Cortinarius mucosus*, 2p excitation at 760 nm. Image of the amplitude-weighted lifetime, tm, and decay curve at cursor position. tm is in the range from 20 to 40 ps, t1 is in the range from 10 to 20 ps.

### *FLIM at Different Excitation Wavelength*

FLIM of the same sample at different excitation wavelength can provide additional information on the composition of the fluorophores contained in it. In the past, beautiful FLIM images were obtained with the 'Intune' laser of the Zeiss LSM 710 systems. Examples are shown in Fig. 36. Unfortunately, the Intune system has been discontinued by Zeiss. There is currently no system that delivers similar performance. The only system that comes close to it is the LSM 980 confocal FLIM system with the bh Laser Hub, see Fig. 37.

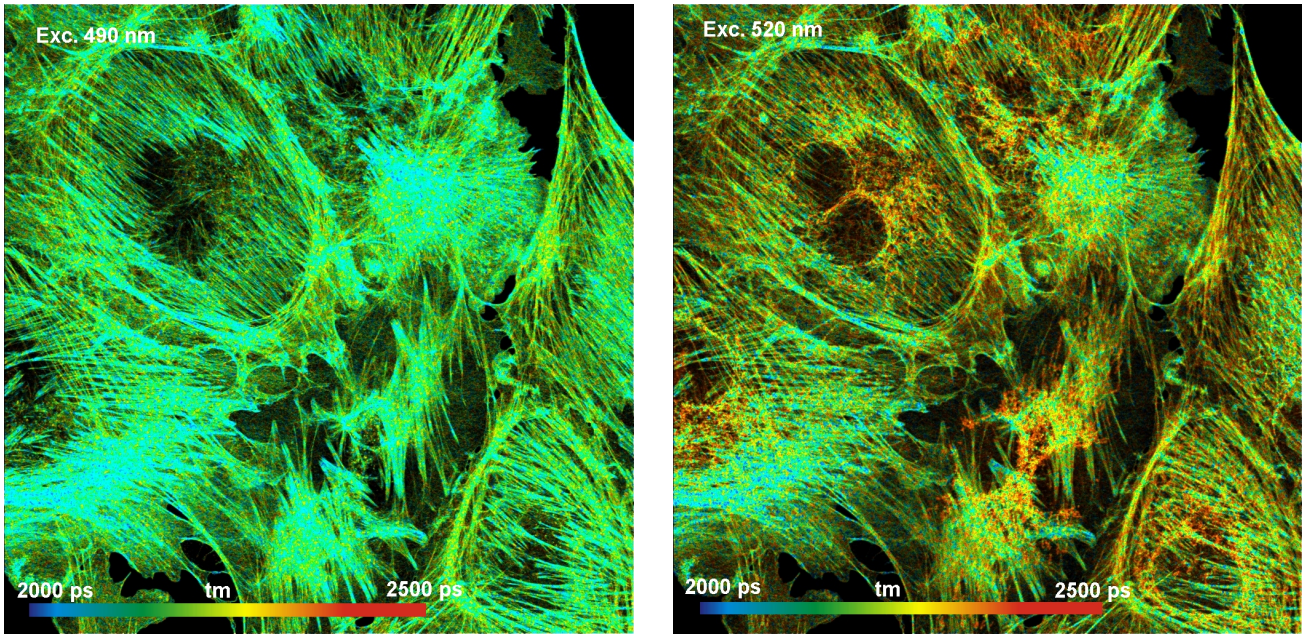


Fig. 36: Confocal FLIM with tuneable 'Intune' laser. BPAE cells stained with Alexa 488 phalloidin and Mito Tracker Red. Amplitude weighted lifetime of double-exponential model. Excitation at 490, 520, 535, and 556 nm, all images 1024 x 1024 pixels. (Continued next page)

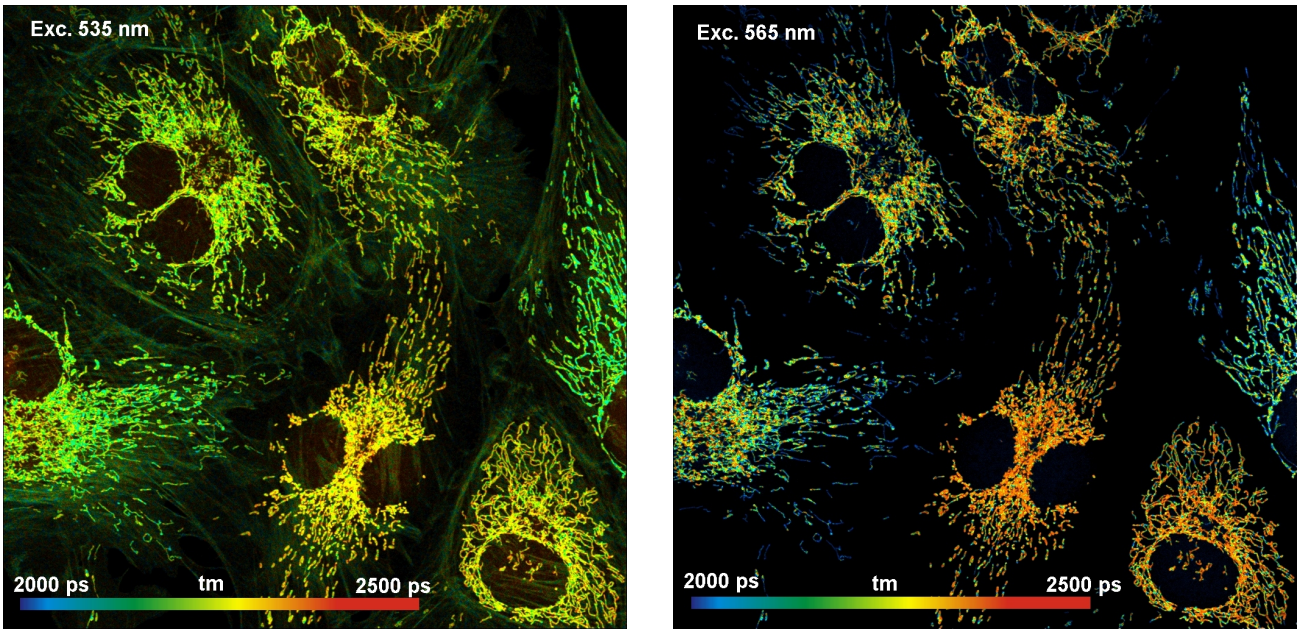


Fig. 36, continued from previous page

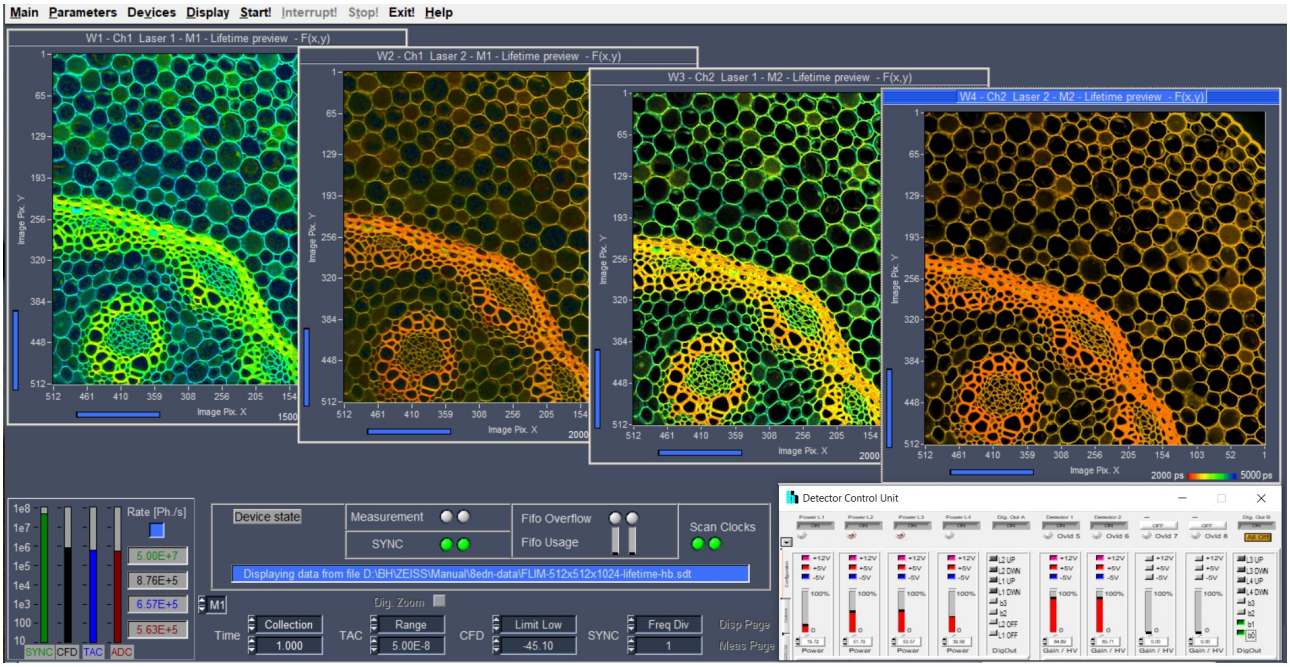


Fig. 37: FLIM at four combinations of excitation and emission wavelength. LSM 980 FLIM system with Laser Hub.

*Near-Infrared FLIM: One-Photon Excitation by Ti:Sapphire Laser*

Near-infrared (NIR) dyes are used as fluorescence markers in small-animal imaging and in diffuse optical tomography of the human brain. In these applications it is important to know whether the dyes bind to proteins or other tissue constituents, and whether their fluorescence lifetimes depend on the targets they bind to. NIR FLIM is possible by using HPM-100-50 detectors and Ti:Sapphire laser excitation. Different than for multiphoton FLIM, the Ti:Sapphire laser is used as a one-photon excitation source [37, 35, 39].

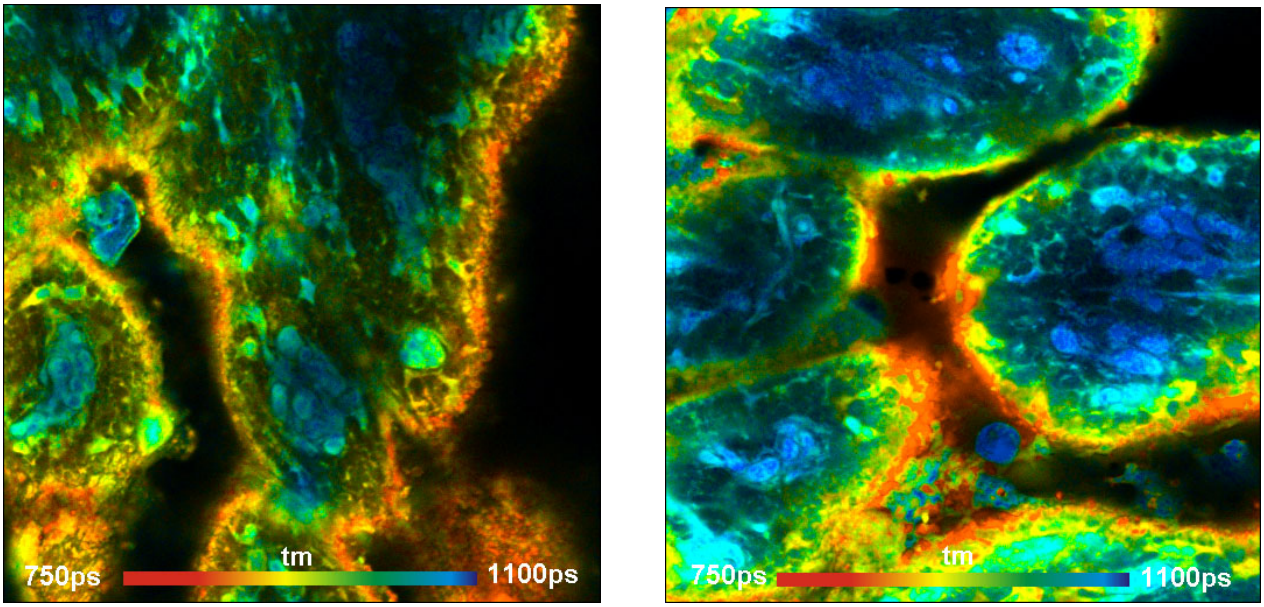


Fig. 38: Pig skin samples stained with 3,3'-diethylthiatricarbocyanine. Excitation at 780nm, detection 800nm to 900nm

*Near-Infrared FLIM: Multiphoton Excitation with OPO*

With the Zeiss LSM NLO OPO systems near-infrared FLIM can be performed by two-photon excitation. The fluorescence signals are detected by HPM-100-50 NIR detectors and non-descanned detection. With excitation wavelengths in the range of 1000 to 1330 nm, the typical NIR dyes are excited at high efficiency [37, 35, 39]. Fluorescence is detected up to 900 nm. An example is shown in Fig. 39.

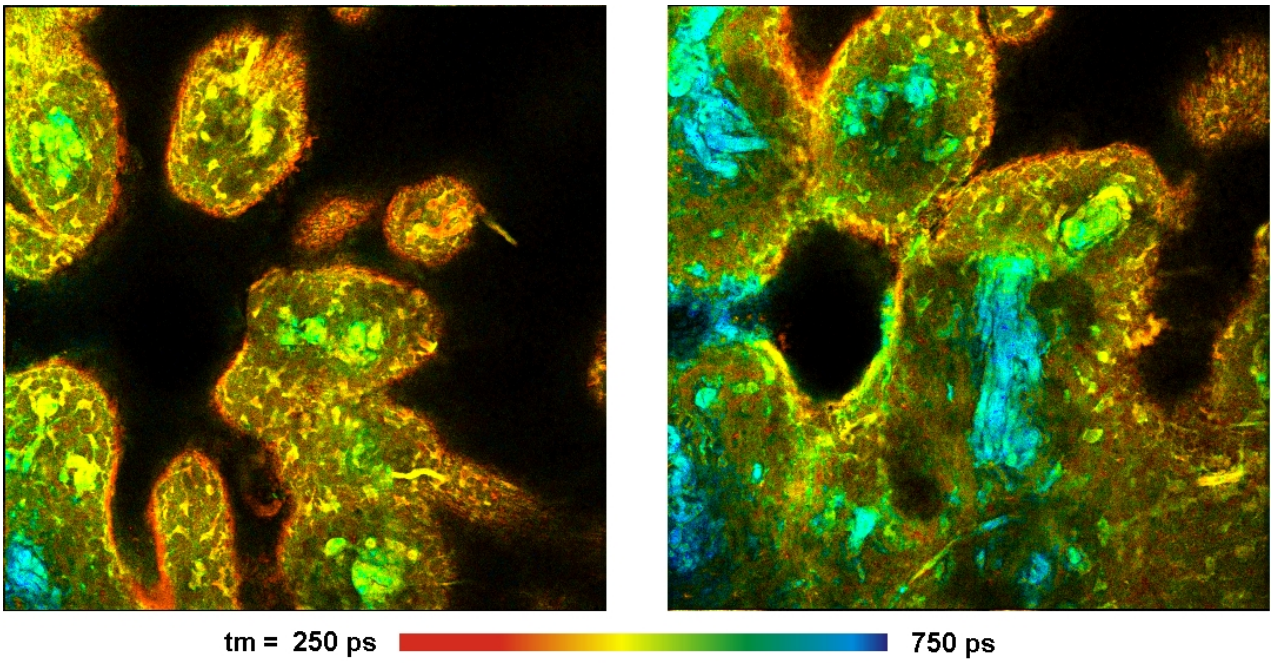


Fig. 39: Pig skin stained with Indocyanin Green. LSM 7 OPO system, two-photon excitation at 1200 nm, non-descanned detection, 780 to 850 nm. Depth from top of tissue 10 µm (left) and 40 µm (right). 512x512 pixels, 256 time channels.

*Confocal Multispectral FLIM*

The bh multispectral FLIM system detects simultaneously in 16 wavelength intervals [28]. By using bh's multi-dimensional TCSPC process it avoids to reject any photons by time gating or wavelength scanning. The systems thus reach near-ideal recording efficiency. Dynamic effects in the sample or photobleaching do not cause distortions of the spectra or decay functions. An example for confocal detection with one-photon (diode-laser) excitation is shown in Fig. 40.

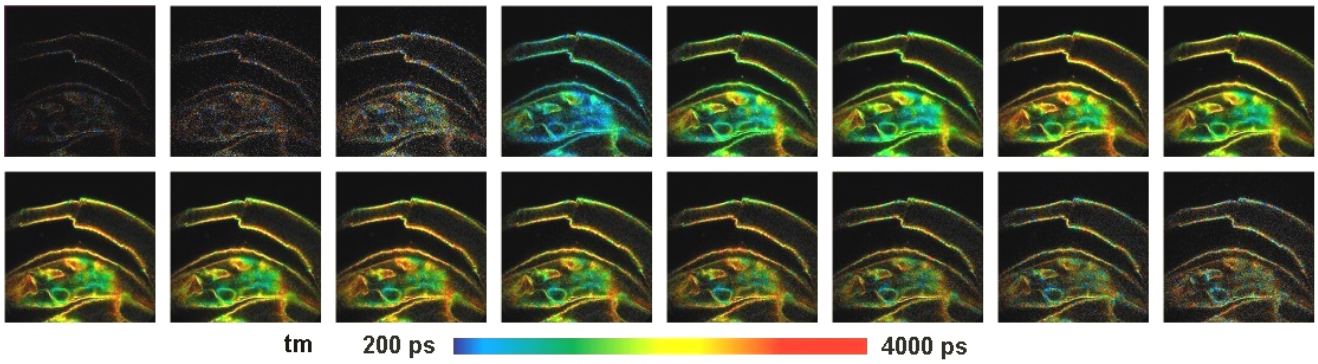


Fig. 40: Confocal multispectral FLIM. Part of a water flee, excitation by 405 nm ps diode laser, LSM 710 confocal port, bh MW FLIM detector

*Multiphoton Multispectral NDD FLIM*

bh's MW FLIM was the world's first simultaneously detecting multiphoton multispectral NDD FLIM system. It uses an optical interface that connects to the NDD ports of the LSM 710/780/880 NLO microscopes [30], see Fig. 20. A typical result is shown in Fig. 41.

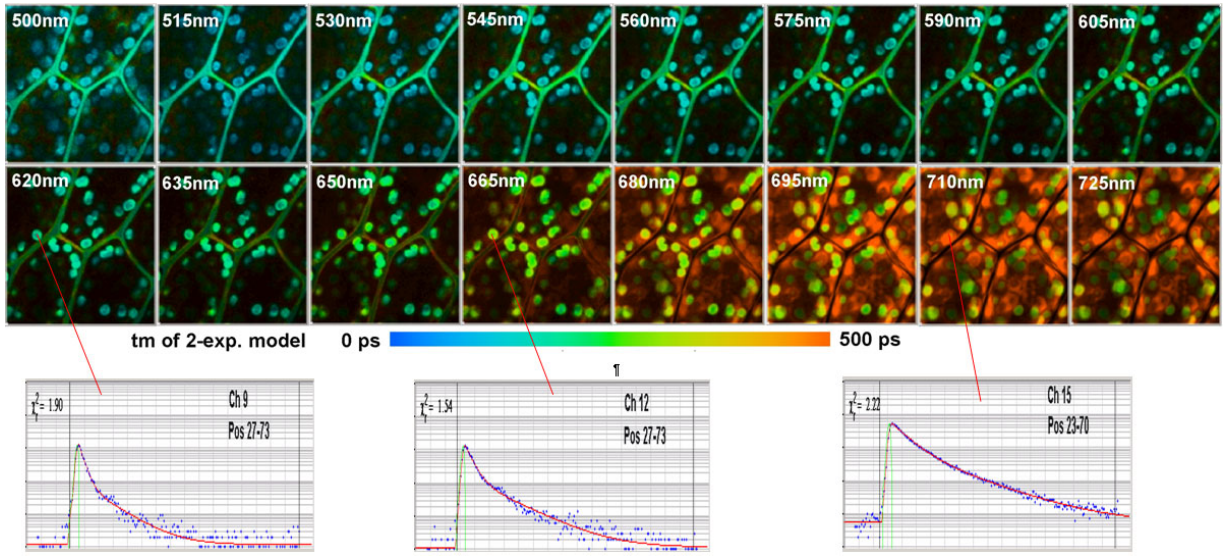


Fig. 41: Multiphoton Multispectral NDD FLIM. Lifetime images and decay curves in selected pixels and wavelength channels. LSM 710 NLO, bh MW FLIM detector

Multispectral FLIM got a new push by the introduction of the new PML-16 GaAsP 16-channel detector. This detector has five time the efficiency of the older PML-16 detectors with conventional cathodes. Another improvement came from bh's Megapixel FLIM technology. Multi-spectral FLIM

can now be obtained at an image size of 512 x 512 pixels in each wavelength channel while maintaining the usual 256-channel time resolution [37].

*Z-Stack FLIM*

For many years, Z-stack FLIM had been prevented by photobleaching and photodamage caused by the high excitation dose. With the LSM 710/780/880 microscopes and the bh GaAsP hybrid detectors photobleaching is no longer a problem. Z-stack FLIM is particularly interesting in combination with the deep-tissue imaging capability of multiphoton NDD FLIM. An example is shown in Fig. 42.

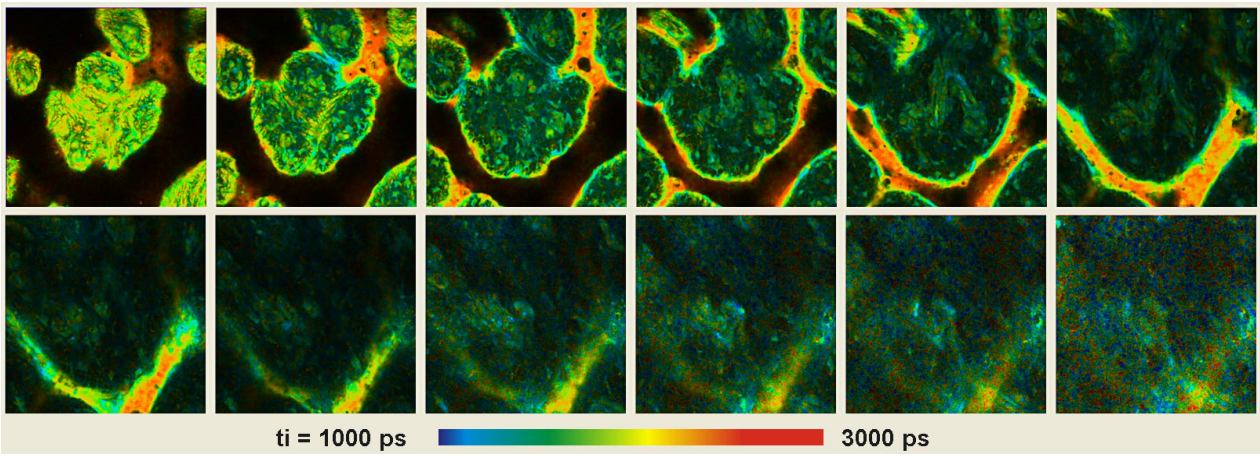


Fig. 42: FLIM Z-stack, planes recorded into a sequence of files. Pig skin, autofluorescence, 5 µm to 60µm below the surface. LSM 710 Multiphoton NDD FLIM, HPM-100-40 GaAsP hybrid detector.

*Infinite-Focus Depth FLIM*

Sometimes it is desirable to project the tree-dimensional structure of a tissue sample into a single image. A frequent example is neuronal tissue where neurons are not necessarily located within a particular image plane. In these cases the SPCM software is able to record a Z stack of the 3-dimensional structure of the sample, and then project a selected number images of different Z planes into a single FLIM data set. An example is shown in Fig. 43.

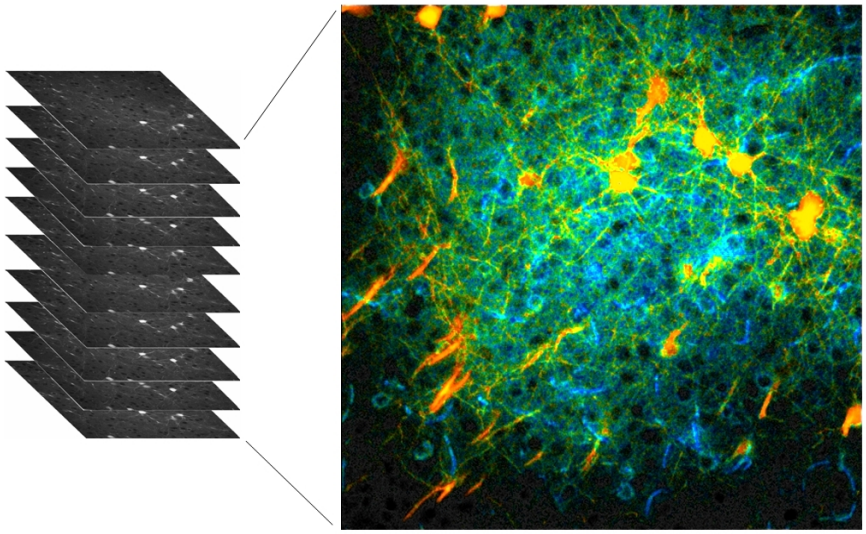

Fig. 43: Infinite-focus depth FLIM. A Z stack of a 3-dimensional sample is recorded, and the image of several planes are projected into a singe FLIM image. Brain tissue, LSM-710 NLO, Simple-Tau 150 FLIM system.

*Time-Series FLIM*

Time-series FLIM is available for all system versions, and all detectors. As for Z stack FLIM, a time series can be acquired both by recording into a series of data files and by Mosaic FLIM. The maximum speed for recording a series of files is about 2 images per second [119]. The speed of temporal mosaic FLIM can be even faster, especially if the lifetime change in the sample is repeatable and can be triggered by an external stimulation. Two time series taken at a moss leafs are shown in Fig. 44 and Fig. 48, page 31. Fig. 44 was acquired by recording into a series of files, Fig. 48, page 31, by recording into the elements of a FLIM mosaic. In both examples, the fluorescence lifetime of the chloroplasts changes due to the Kautski effect induced by the illumination.

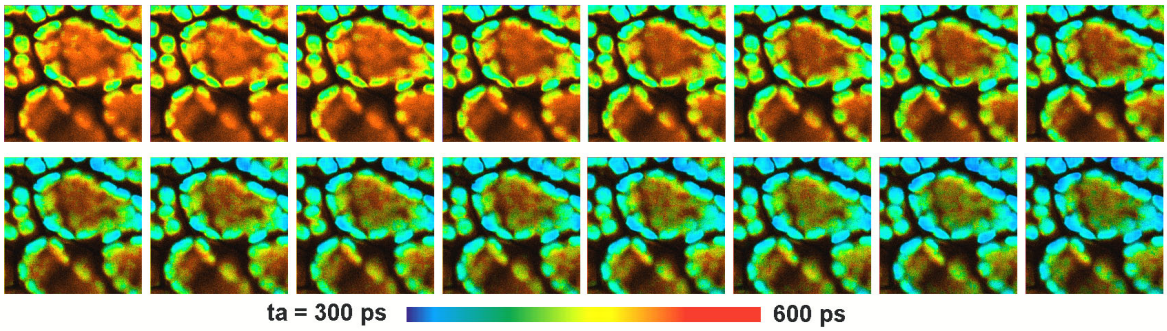


Fig. 44: Time-series FLIM, recorded into sequence of files. Acquisition time 2 seconds per image. Chloroplasts in moss leaf, the lifetime changes due to the Kautski effect

*Fast Acquisition FLIM*

With bh standard bh FLIM systems data can be recorded with acquisition times as short a 100 ms [19]. Due to the low number of photons recorded in this time, the SNR of such images is relatively low. Much higher count rates and higher SNR can be obtained by the bh FASTAC FLIM system. The system is based on fast distribution of the photon pulses of a PMH-100 hybrid detector into four parallel TCSPC FLIM channels [20, 21, 22]. The IRF width with fast detectors is less than 25 ps FWHM, and the temporal data are recorded with typically 1024 time channels per pixel. This is much better than for any other 'Fast FLIM' system. Two images recorded by the system are shown in Fig. 45. Although the FASTAC system is able to record high-resolution FLIM data within short acquisition time the importance of fast FLIM should not be over-estimated. A FLIM system can only be fast if the sample is able to feed it with a high photon rate. This may be the case for demonstration samples as the one in Fig. 45. However, the count rate in typical molecular imaging application is much lower so that the recording speed of a fast FLIM system cannot be exploited.

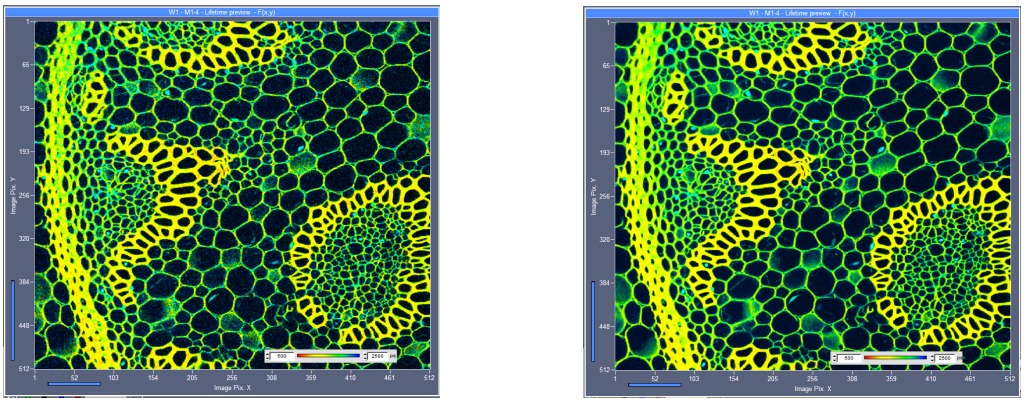

Fig. 45: Convallaria sample, 512 x 512 pixels, 1024 time channels. Left: Acquisition time 0.6 seconds. Right: Acquisition time 4 seconds. Images calculated by online-FLIM algorithm of SPCM. bh FASTAC system with Zeiss LSM 880.

*Spatial Mosaic FLIM*

Mosaic FLIM is based on bh's 'Megapixel FLIM' technology introduced in 2014. Mosaic FLIM records a large number of images into a single FLIM data array. The individual images within this array can be for different displacement of the sample (spatial mosaic), different depth within the sample (z-stack mosaic), of for different times after a stimulation of the sample (temporal mosaic). Spatial mosaic FLIM combines favourably with the Tile Imaging capability of the Zeiss LSM 710/780 systems. An example is shown in Fig. 46. The complete data array has 2048 x 2048 pixels, and 256 time channels per pixel. Compared to a similar image taken through a low-magnification lens the advantage of mosaic FLIM is that a lens of high numerical aperture can be used, resulting in high detection efficiency and high spatial resolution.

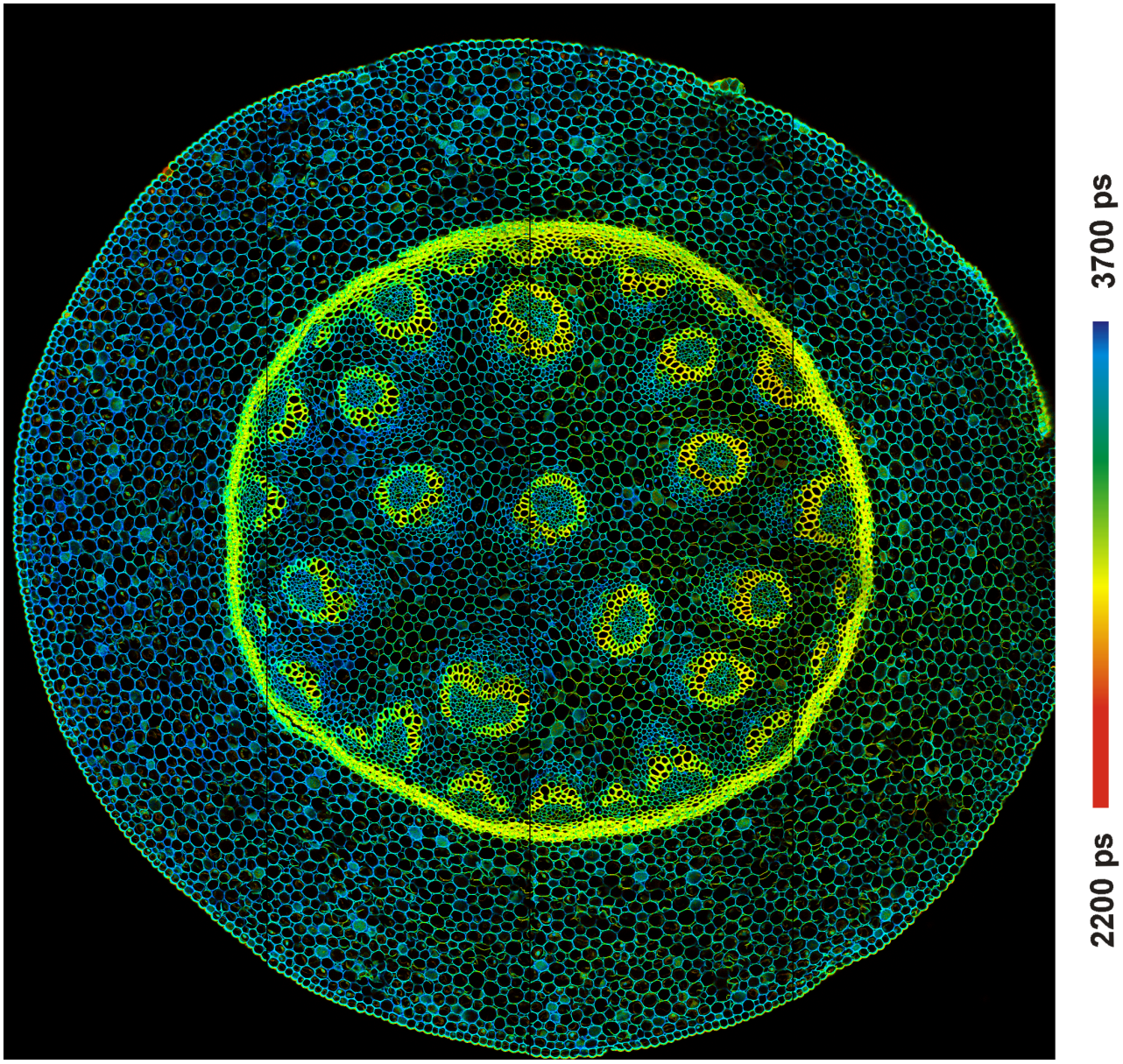


Fig. 46: Mosaic FLIM of a Convallaria sample. The mosaic has 4x4 elements, each element has 512x512 pixels with 256 time channels. The complete mosaic has 2048 x 2048 pixels, each pixel holding 256 time channels. Zeiss LSM 710 Intune system with bh Simple-Tau 150 FLIM system. Total sample size covered by the mosaic 2.5 x 2.5 mm.

*Z Stack Mosaic FLIM*

The Mosaic FLIM function can be used to record Z Stacks of FLIM images. As the microscope scans consecutive images planes in the sample the FLIM system records the data into consecutive elements of a FLIM mosaic. The advantage over the traditional record-and-save procedure is that no time has to be reserved for save operations, and that the entire array can be analysed in a single analysis run.

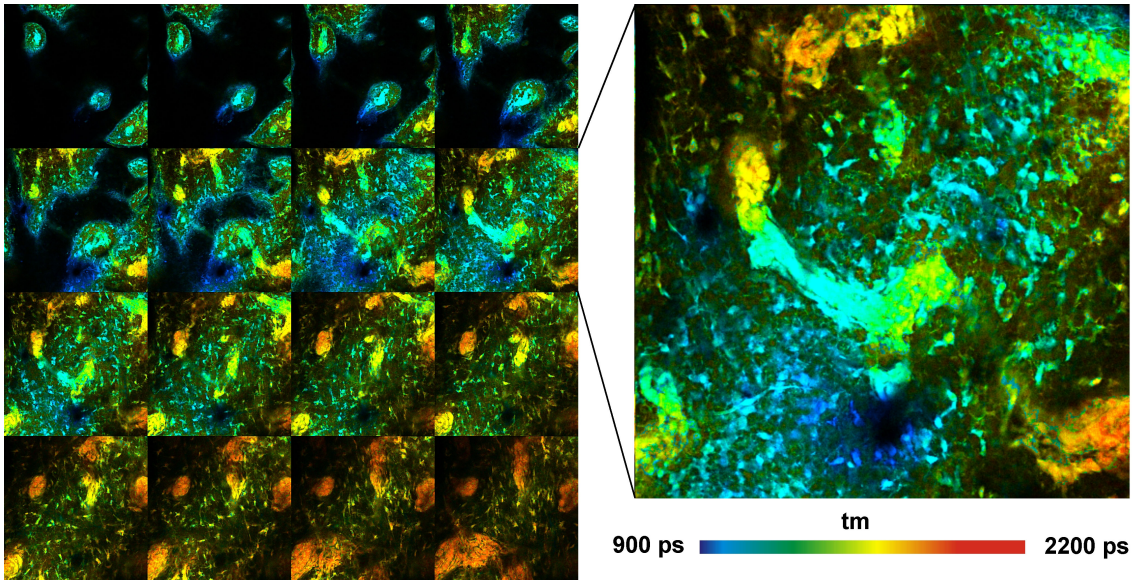


Fig. 47: FLIM Z-stack, recorded by Mosaic FLIM. Pig skin stained with DTTC. 16 planes, 0 to 60 um from top of tissue. Each element of the FLIM mosaic has 512x512 pixels and 256 time channels per pixel. Plane 8 is shown magnified on the right. LSM 7 OPO system, HPM-100-50 GaAs hybrid detector.

*Temporal Mosaic FLIM*

Mosaic FLIM can be used to record FLIM time series. An example is shown in Fig. 48.

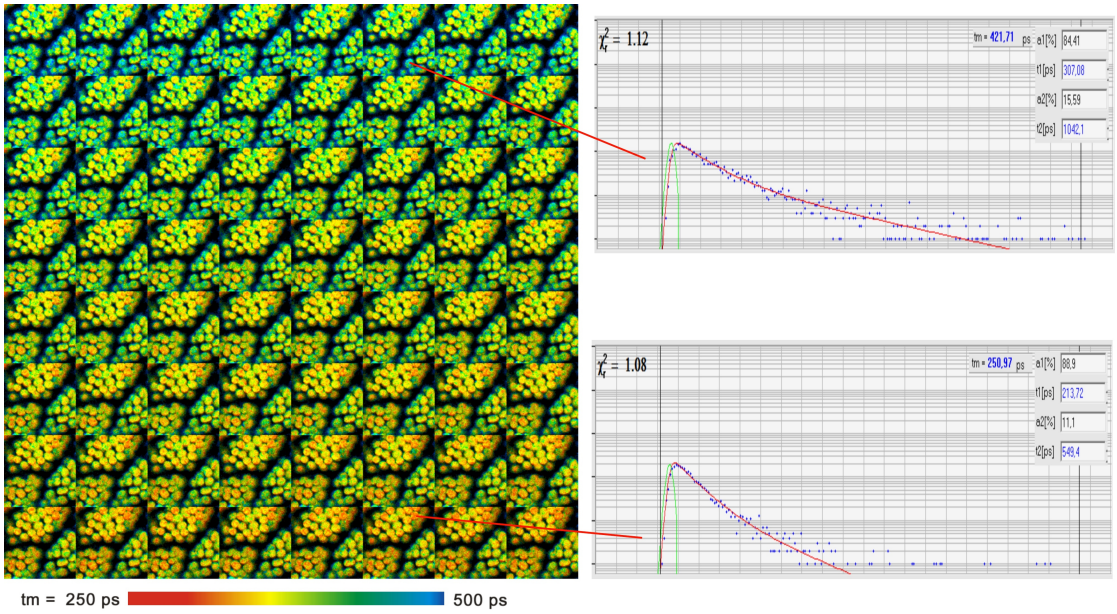


Fig. 48: Time series acquired by mosaic FLIM. Recorded at a speed of 1 mosaic element per second. 64 elements, each element 128 x 128 pixels, 256 time channels, double-exponential fit of decay data. Sequence starts at upper left. Moss leaf, lifetime changes by non-photochemical chlorophyll transient.

Also here, the advantage is that no time has to be reserved for save operations during the recording sequence. A Mosaic-FLIM time series can therefore be made very fast. The most important advantage is, however, that temporal Mosaic FLIM data can be accumulated. A lifetime change in the sample is stimulated periodically, and a mosaic recording sequence started for each stimulation. Because the entire photon distribution is kept in the memory the photons from the subsequent runs are automatically accumulated. The result is that the signal-to-noise ratio no longer depends on the speed of the series. The only speed limitation is the minimum frame time of the scanner. For the Zeiss LSMs frame times of less than 40 milliseconds can be achieved. This brings the transient-time resolution down to the range where $Ca^{2+}$ transients in neurons occur. Experiments have shown that these can indeed by recorded. An example is shown in Fig. 49.

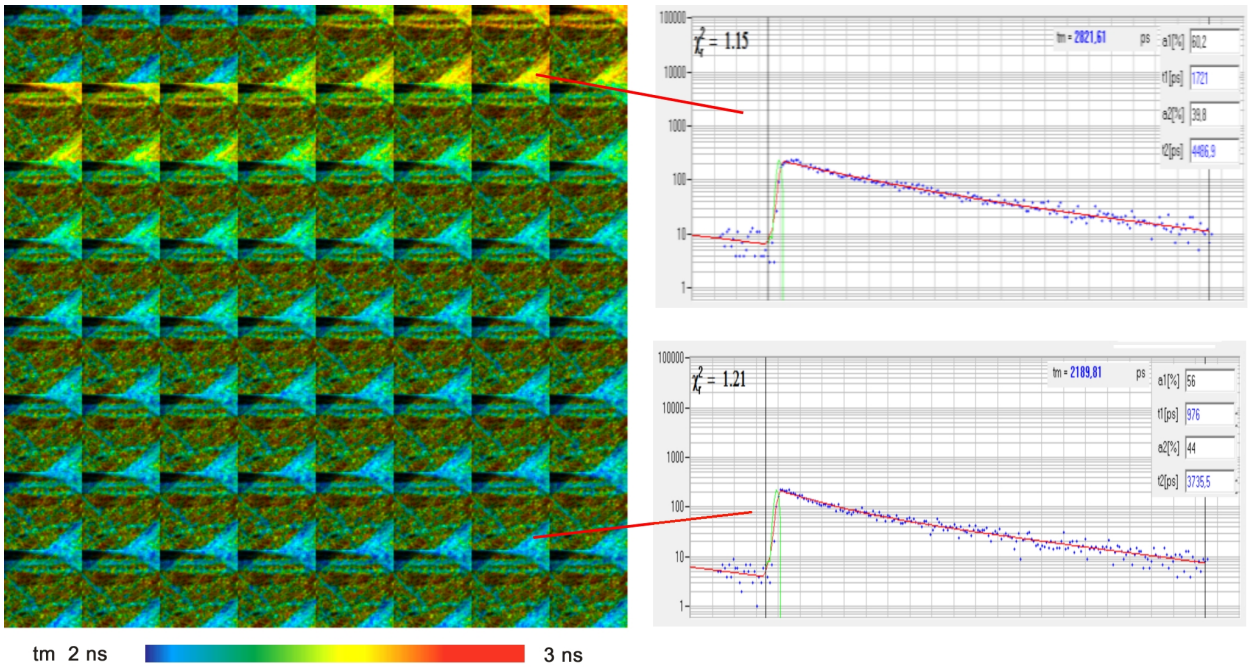


Fig. 49: Temporal mosaic FLIM of the $Ca^{2+}$ transient in cultured neurons after stimulation with an electrical signal. The time per mosaic element is 38 milliseconds, the entire mosaic covers 2.43 seconds. Experiment time runs from upper left to lower right. Photons were accumulated over 100 stimulation periods. Zeiss LSM 7 MP multiphoton microscope and bh SPC-150 TCSPC module. Data courtesy of Inna Slutsky and Samuel Frere, Tel Aviv University, Sackler Faculty of Medicine.

*Mosaic FLIM with Routing*

The elements of a FLIM mosaic can be assigned to information delivered to the TCSC modules via their routing inputs. The traditional application is multi-wavelength FLIM. Examples for multi-wavelength FLIM by the Mosaic FLIM function are shown in [12] and [37]. A potential application is the combination of FLIM with electro-physiology. In that case, one ore more electrophysiology signals would be measured by micro-electrodes, digitized, and used to control the mosaic element into which the photons are recorded. The result would be a mosaic of FLIM images for different physiological states of the cells.

*FLITS: Fluorescence Lifetime-Transient Scanning*

FLITS records transient effects in the fluorescence lifetime of a sample along a one-dimensional scan. The maximum resolution at which lifetime changes can be recorded is given by the line scan time. With repetitive stimulation and triggered accumulation transient lifetime effects can be resolved at a resolution of about one millisecond [37, 33]. Typical applications are recording of chlorophyll transients and $Ca^{2+}$ transients in neurons or neuronal tissue [36]. Examples are shown in Fig. 50 and Fig. 51.

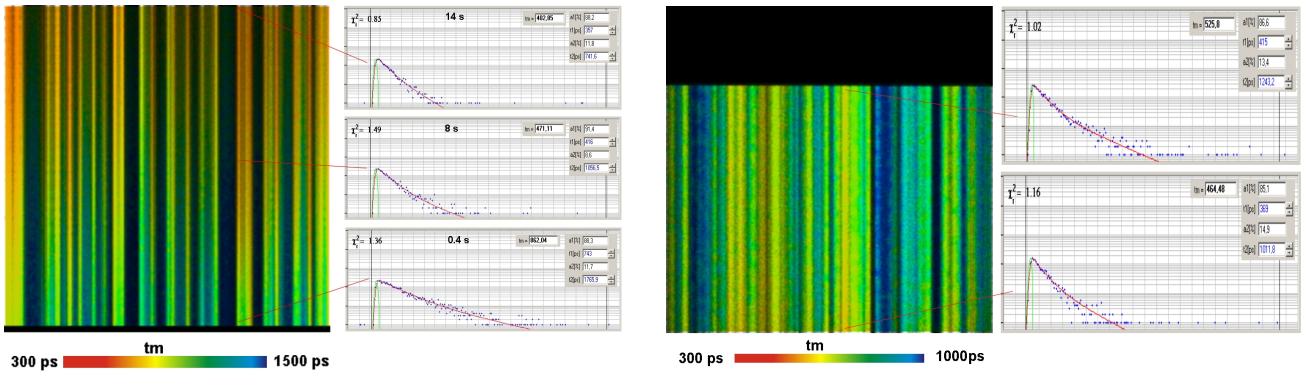


Fig. 50: FLITS of chloroplasts in a grass blade, change of fluorescence lifetime after start of illumination. Experiment time runs bottom up. Left: Non-photochemical transient, transient resolution 60 ms. Right: Photochemical transient. Triggered accumulation, transient-time resolution 1 ms.

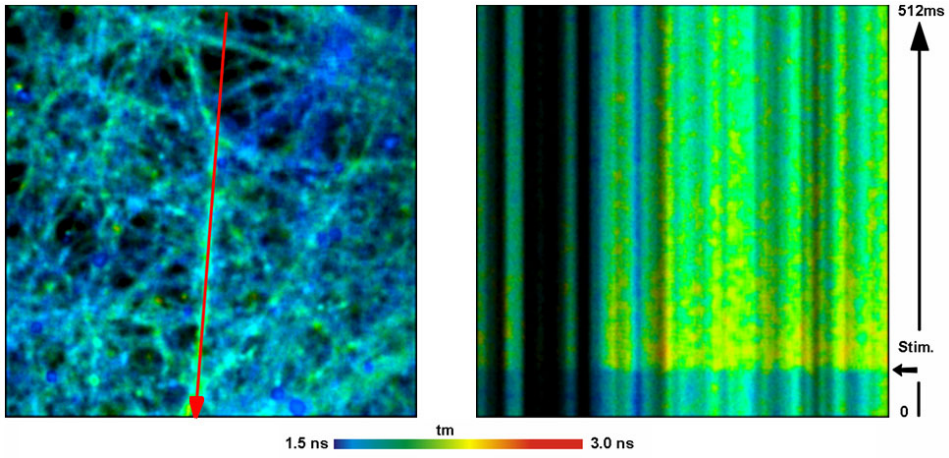


Fig. 51: FLITS of $Ca^{2+}$ concentration in cultured neurons. Ca2+ sensor Oregon Green, LSM 7 MP, electrical stimulation, 100 stimulation periods accumulated. Transient-time resolution 2 ms.

*Simultaneous FLIM / PLIM*

The bh FLIM systems are able to simultaneously record fluorescence (FLIM) and phosphorescence lifetime images (PLIM). The technique is based on modulating a high-frequency pulsed excitation laser synchronously with the pixel clock of the scanner. Photon times are determined both with reference to the laser pulses and the laser modulation period [16, 32, 37]. Fluorescence is recorded during the 'on' time, phosphorescence during the 'off' time of the laser. The technique does not require a reduction of the laser repetition rate, works with two-photon excitation and non-descanned detection, and delivers an extremely high PLIM sensitivity. Unlike other PLIM techniques, it does not cause moiré in the images and can thus be used at scan rates no lower than the reciprocal

phosphorescence decay time. For procedures and parameter setup in combination with the Zeiss LSMs please see [6]. A typical result is shown in Fig. 52.

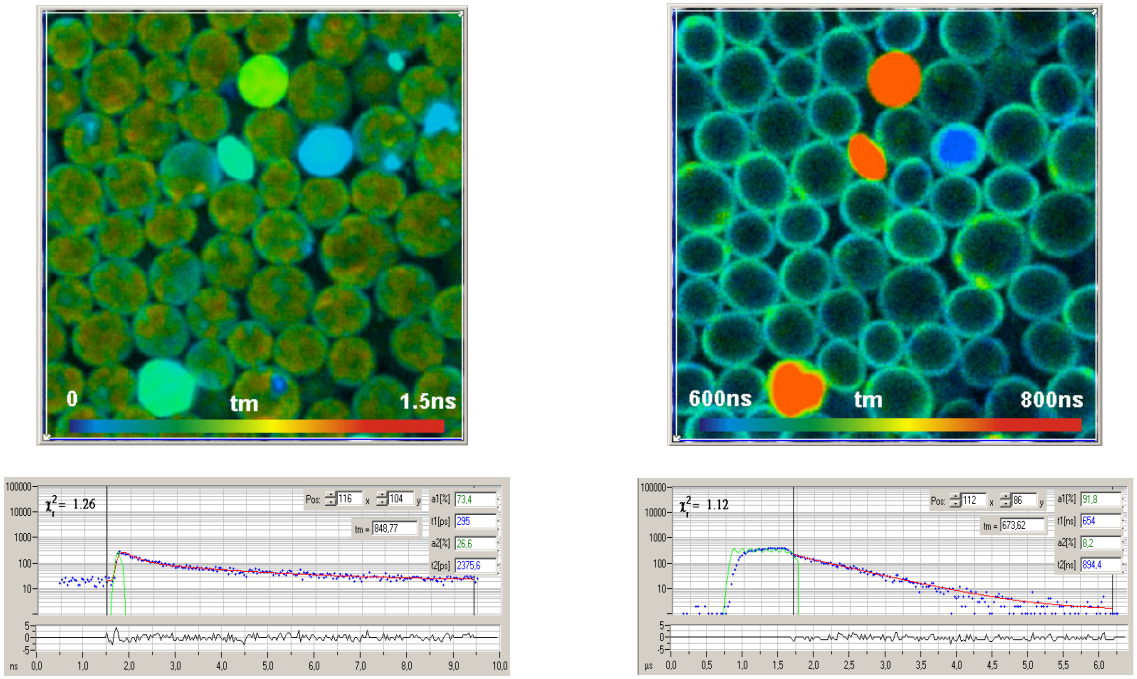


Fig. 52: Yeast cells stained with a Ruthenium dye. Left: FLIM image and fluorescence decay curve in selected spot. Right: PLIM image and phosphorescence decay curve in selected spot.

*FCS*

The bh GaAsP hybrid detectors deliver highly efficient FCS [6, 31, 37]. Because the detectors are free of afterpulsing diffusion times are obtained from a single detector, without the loss in correlation events that occurs when the signals from two detectors are cross-correlated. FCS is be obtained with the diode-laser systems, the Intune system, and even with the multiphoton NDD systems. The bh SPCM data acquisition software calculates FCS online and fits the data with a user-configurable model function [37].

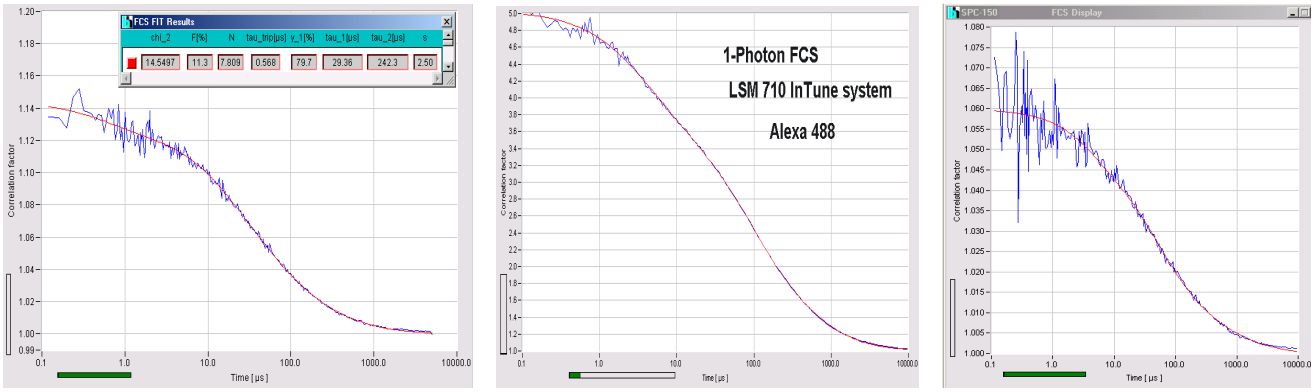


Fig. 53: FCS with GaAsP hybrid detectors. Left to right: Confocal FCS with ps diode laser, Confocal FCS with Intune laser, Two-photon NDD FCS

## SPCImage FLIM Data Analysis

Since 2019 the bh FLIM systems for the Zeiss LSMs use bh 'next Generation' SPCImage NG data analysis software [6, 8]. The main panel of the SPCImage NG is shown in Fig. 54. It shows a lifetime image (left), a parameter histogram over the pixels of a region of interest (upper right), and the fluorescence decay curve in a selected spot of the image (lower right). The basic model parameters (one, two or three exponential components) are shown in the upper right.

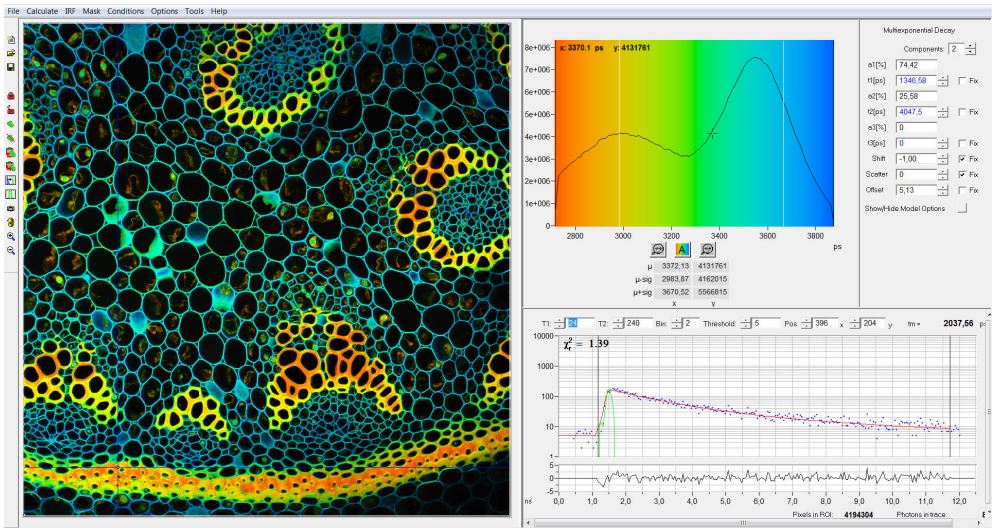

Fig. 54: Main panel of the SPCImage NG data analysis

SPCImage NG runs a de-convolution on the decay data in the pixels of FLIM data. It uses single, double, or triple-exponential decay analysis to produce pseudo-colour images of lifetimes, amplitudes, or intensities of decay components, or of ratios of these parameters. Different than previous versions, SPCImage NG uses a maximum-likelihood estimation (MLE) process to determine the decay parameters in the pixels. In contrast to the frequently-used weighted least-square (WLS) fit, MLE is based on calculating the probability that the values of the model function correctly represent the data points of the decay function. MLE is not only faster than WLS, it also avoids that the determined lifetimes are biased towards lower values when the photon numbers in the pixels are low.

### *Decay Models*

SPCImage NG provides single-, double-, and triple-exponential decay models. An 'incomplete decay' option is available to determine long fluorescence lifetimes within the short pulse period of the Ti:Sa laser of a multiphoton system. A fit of long-lifetime decay data with an incomplete-decay model is shown in Fig. 55.

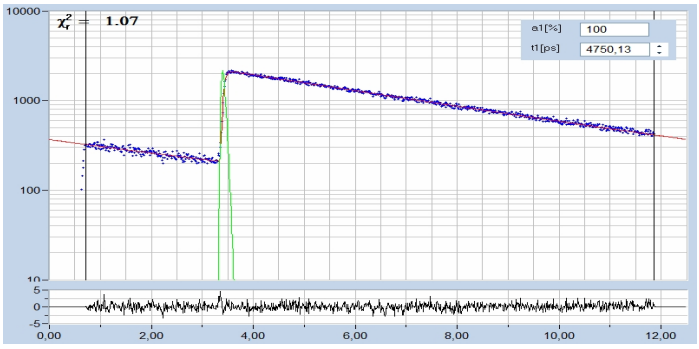


Fig. 55: Fit of a long-lifetime decay with an incomplete-decay model

*Instrument-Response Function*

Importantly, SPCImage NG avoids troublesome recording of an instrument response function (IRF) in short intervals or even for each FLIM measurement. This is achieved by modelling the IRF with a generic function. The parameters of this function are determined by fitting it to the FLIM data together with the selected decay model. The results of this procedure are so good that an accurate IRF is obtained even for decay functions containing ultra-fast components, see Fig. 56. For details please see [6, 8] or [37].

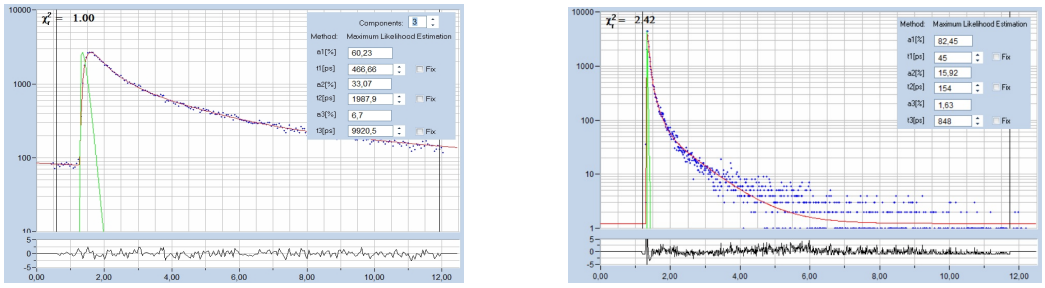

Fig. 56: Analysis with synthetic IRF. Left: Diode laser, HPM-100-40. Right: Ti:Sa laser, sample with extremely fast decay component.

*GPU Processing*

SPCImage NG uses GPU (Graphics Processor Unit) processing for MLE data analysis. The FLIM data are transferred into the GPU, which then runs the de-convolution and fit procedure for a large number of pixels in parallel. Data processing times are thus massively reduced. GPU processing is running an NVIDIA cards and a number of other NVIDIA-compatible display devices. When SPCImage NG finds a suitable device in the computer it automatically runs the data analysis on it. An example is shown in Fig. 57. The image has 1024 x 1024 pixels and 1024 time channel per pixel. By GPU processing, it is analysed in less than 10 seconds.

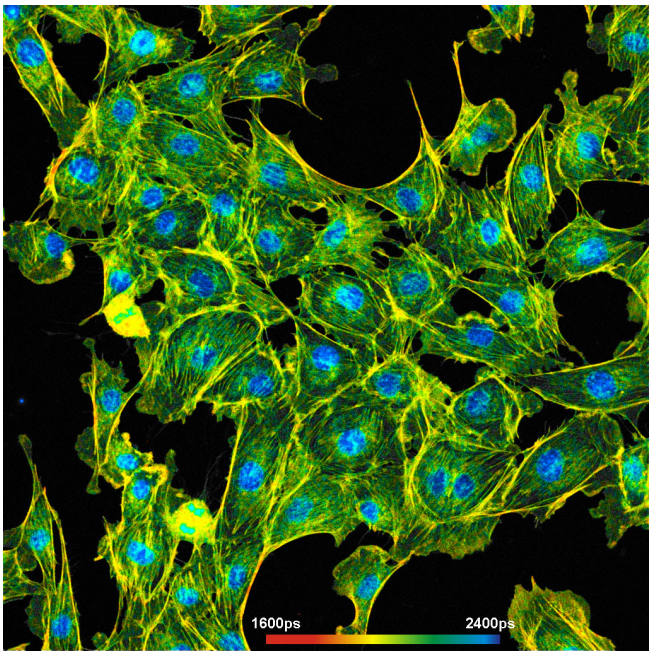


Fig. 57: A lifetime image with 1024 x 1024 pixels and 1024 time channel per pixel. Data analysis was performed on an NVIDIA GPU in less than 10 seconds. BPAE cells, recorded by bh FASTAC FLIM system on a Zeiss LSM 880 NLO.

*Multi-Exponential Decay Parameters*

For complex decay functions the fit procedure delivers the lifetimes and amplitudes of the decay components. SPCImage then creates colour-coded images of the amplitude- or intensity-weighted lifetimes in the pixels, images of the lifetimes or amplitudes of the decay components, or images of lifetime or amplitude ratios, see Fig. 58. SPCImage NG is able to calculate also other combinations of decay parameters, such as FRET intensities, FRET distances, bound-unbound ratios, or the fluorescence-lifetime redox ratio, FLIRR.

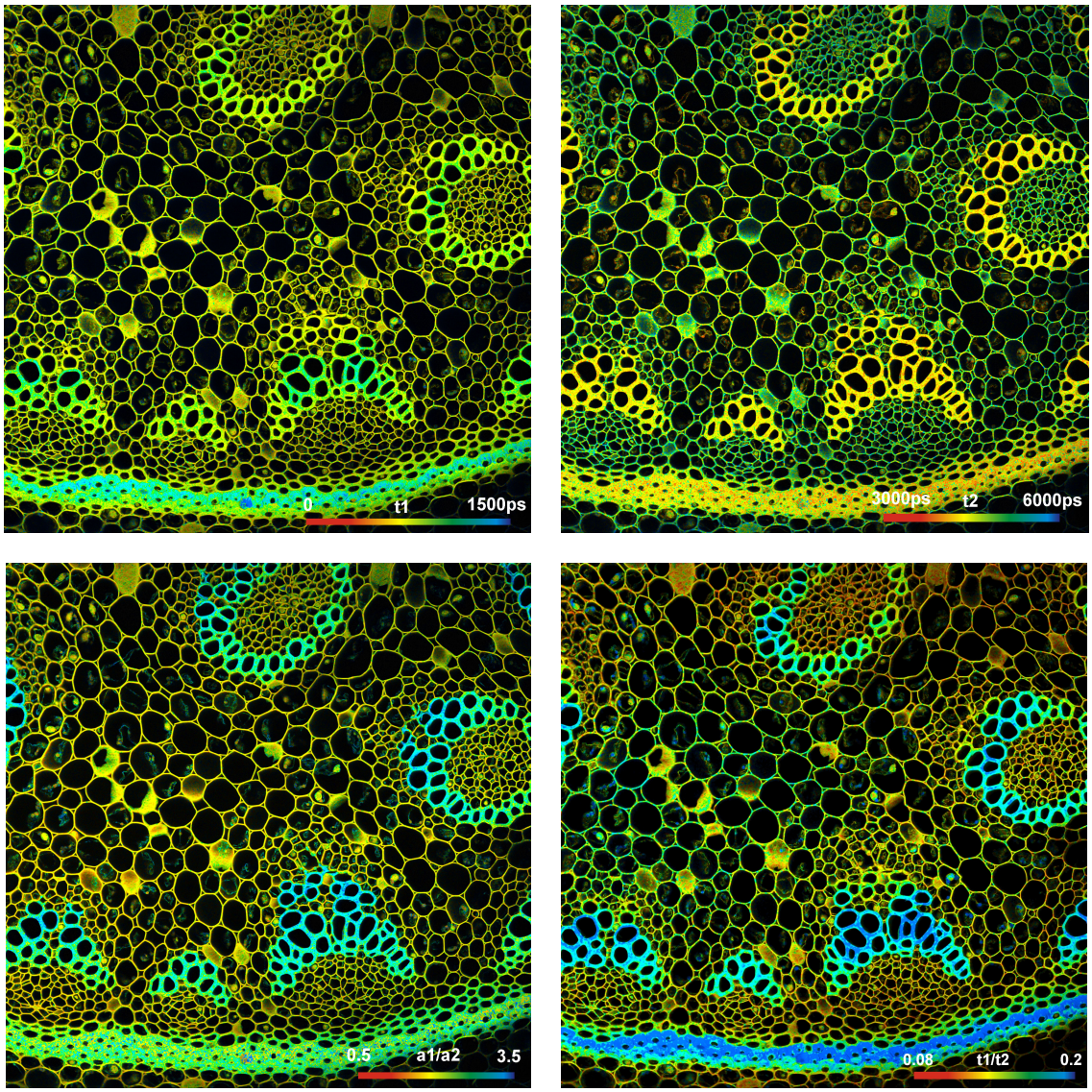


Fig. 58: Upper row: Images of the lifetimes of the fast component, t1, and the slow component, t2, of a double-exponential decay. Lower Row: Images of the amplitude ratio, a1/a2, and the lifetime ratio, t1/t2, of the fast and the slow decay component.

*Dual-Channel Analysis*

SPCImage is able to hold up to 16 images of different detection or laser channels in the memory. Two of these images can be displayed simultaneously, see Fig. 59. Data operations, such as calculations of ratios of component lifetimes or amplitudes, can be performed between the two channels.

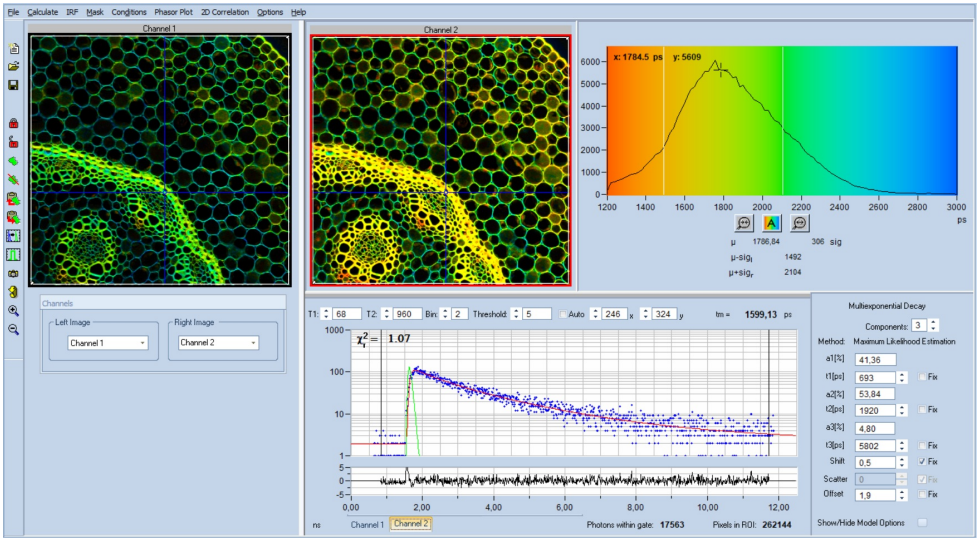

Fig. 59: SPCImage NG holding data from two FLIM channels

*Phasor Plot*

SPCImage FLIM analysis software combines time-domain multi-exponential decay analysis with phasor analysis. Phasor analysis expresses the decay data in the individual pixels as phase and amplitude values in a polar diagram, the 'Phasor Plot' [74, 75]. Pixels with similar decay signature form distinct clusters in the phasor plot. Clusters of interest can be selected and back-annotated in the lifetime image for further processing or for combination of pixel data [37]. The main panel of SPCImage NG with the phasor plot opened is shown in Fig. 60.

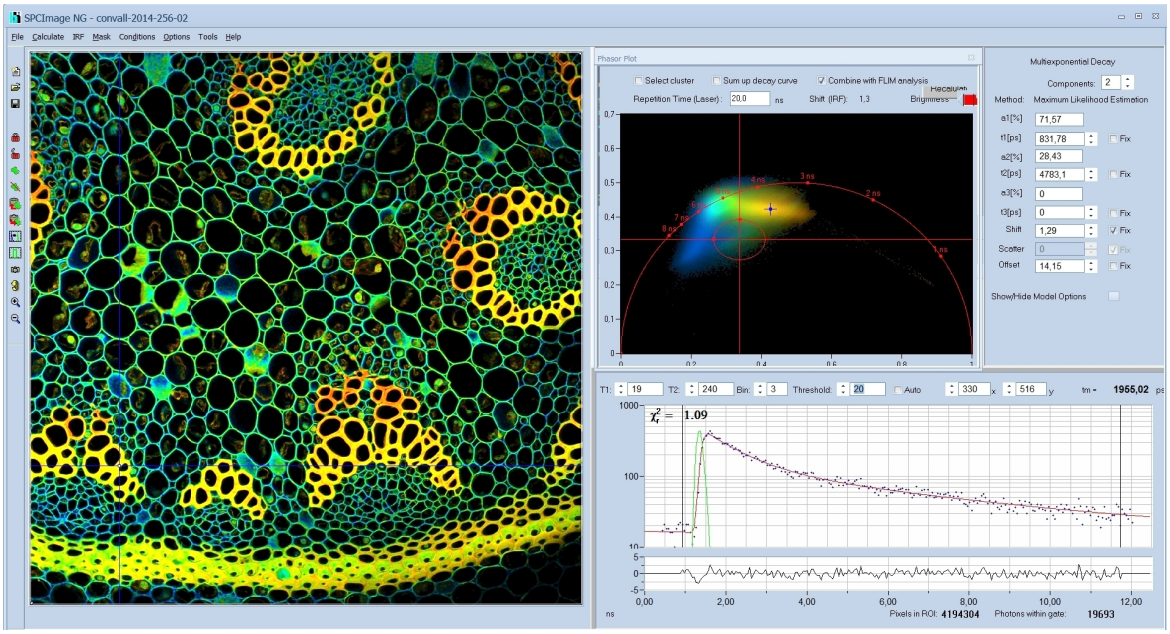

Fig. 60: Combination of time-domain analysis (left and lower right) and Phasor Plot (upper right)

Selection of different phasor clusters and combination of the corresponding pixels into a single precision decay curve are shown in Fig. 61 and Fig. 62. Please see [17] and [37] for details.

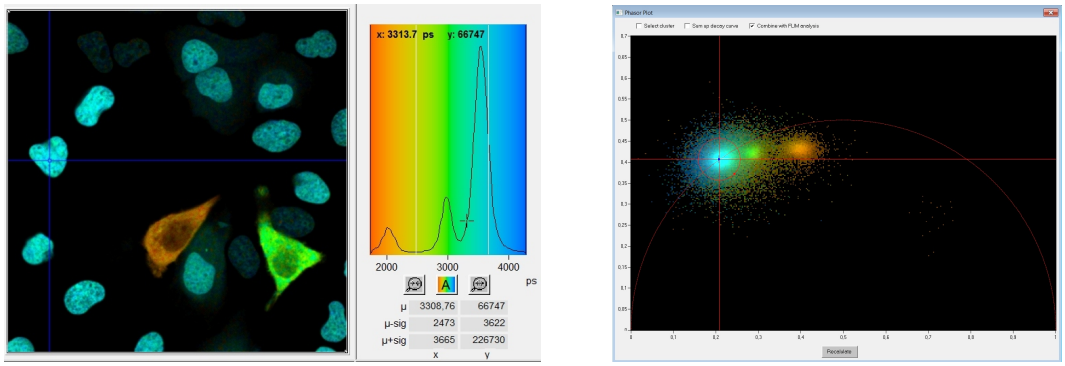

Fig. 61: Left: Lifetime image and lifetime histogram. Right: Phasor plot. The clusters in the phasor plot represent pixels of different lifetime in the lifetime image. Recorded by bh Simple-Tau 152 FLIM system with Zeiss LSM 880.

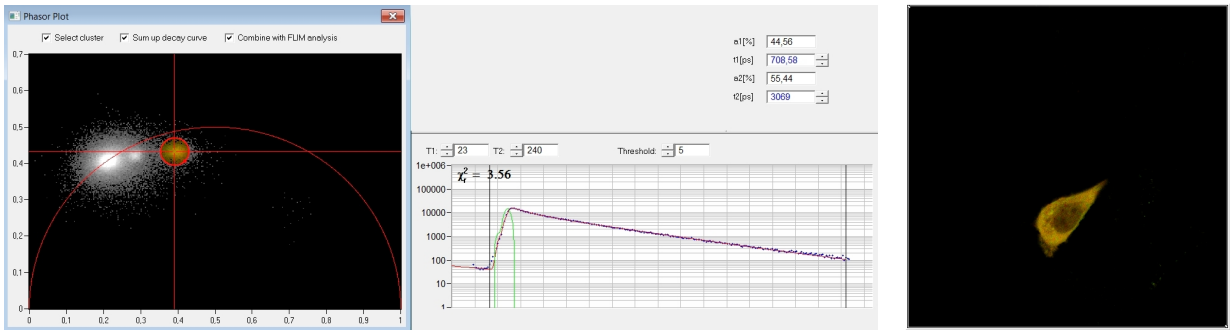

Fig. 62: Left: Selecting a cluster of phasors in the phasor plot. Middle: Combination of the decay data of the corresponding pixels in a single decay curve. Right: Display of the pixels corresponding to the cluster selected in the phasor plot.

### *ROI Selection and Histogram Functions*

SPCImage has tools to select ROIs within a FLIM image, and functions to display parameter histograms within one or several ROIs. The histogram shows how often pixels of a given parameter value (lifetime, lifetime of a decay component, amplitude of a component, or combinations of these values) occur in the ROI. An example is shown in Fig. 63.

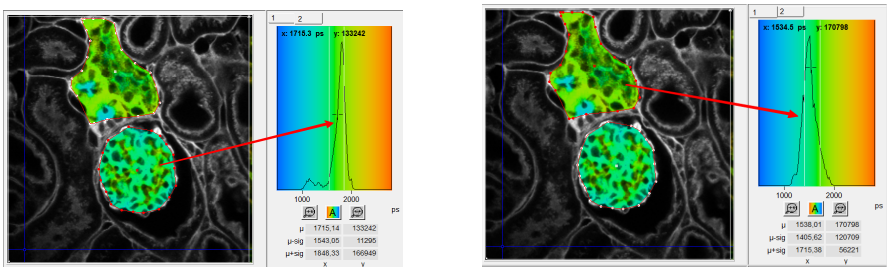

Fig. 63: Decay-parameter histograms for two different regions of interest

### *Other SPCImage Functions*

There are more functions of SPCImage than can be described in this brochure. For example, two different decay parameters can be displayed against each other in two-dimensional histograms, clusters found in these histograms can be back-annotated in the images, decay curves can be summed up within ROIs or clusters, sequences of data files can be batch-processed, and the results can be exported as image files. Please refer to [38], chapter 'SPCImage NG Data Analysis'.

# FLIM Applications

When fluorescence in a sample is excited (Fig. 64, left) the emission intensity depends both on the concentration of the fluorophore and on possible interaction of the fluorophore with its molecular environment. If only the intensity of the fluorescence is recorded changes in the concentration cannot be distinguished from changes in the molecular environment. Intensity imaging (second left) is thus an excellent way to resolve the spatial structure of a sample but it does not tell much about effects on the molecular scale. Spectral measurements (second right) are able to distinguish between different fluorophores. However, changes in the local environment usually do not cause changes in the shape of the spectrum. Information about molecular effects is thus difficult to obtain. The fluorescence lifetime of a fluorophore (Fig. 64, right), within reasonable limits, does not depends on the concentration but systematically changes on interaction with the molecular environment. By using the fluorescence lifetime, or, more precisely, the shape of the fluorescence decay function, molecular effects can therefore be investigated independently of the unknown and usually variable fluorophore concentration [34, 37, 47, 56, 137, 166, 195].

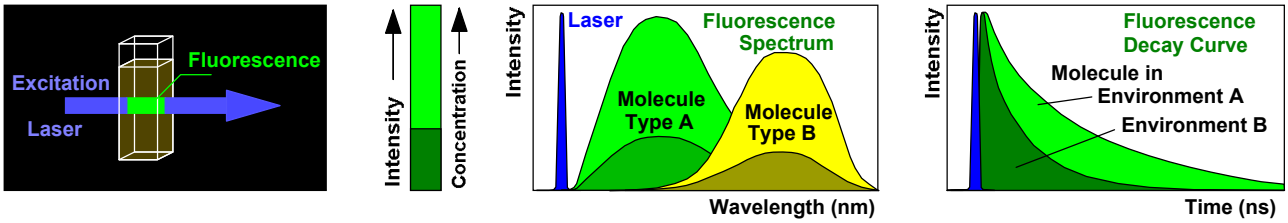


Fig. 64: Fluorescence. Left to right: Excitation light is absorbed by a fluorophore, and fluorescence is emitted at a longer wavelength. The fluorescence intensity varies with concentration. The fluorescence spectrum is characteristic of the type of the fluorophore. The fluorescence decay function is an indicator of interaction of the fluorophore with its molecular environment.

Common FLIM applications are measurements of the molecular environment of the fluorophores, pH and ion concentration measurements, probing of protein interaction via FRET, and investigation of metabolic activity and cell viability via the fluorescence lifetimes of NADH and FAD. FLIM may also find application in plant physiology because the fluorescence lifetime of chlorophyll changes with the photosynthesis activity.

## Measurement of Molecular Environment Parameters

### *pH Imaging*

An example of recording variation in local environment parameters is shown in Fig. 65. A skin sample was stained with 2',7'-bis-(2-carboxyethyl)-5-(and-6)-carboxyfluorescein (BCECF). BCECF has a protonated and a deprotonated form. Both forms have different fluorescence lifetimes. The average lifetime is a direct indicator of the pH in the immediate molecular environment of the fluorophore [104, 137]. Similar approaches can be used to measure concentrations of various ions. An application for determining absolute calcium concentrations in mice brains has been described in [131]. FLIM is also used for measuring the concentration of intracellular $Cl^-$ in neurons [93, 117]. Changes of the $Cl^-$ concentration during maturation of chloride homeostasis in neurons were investigated in [100], changes on inflammation in [90].

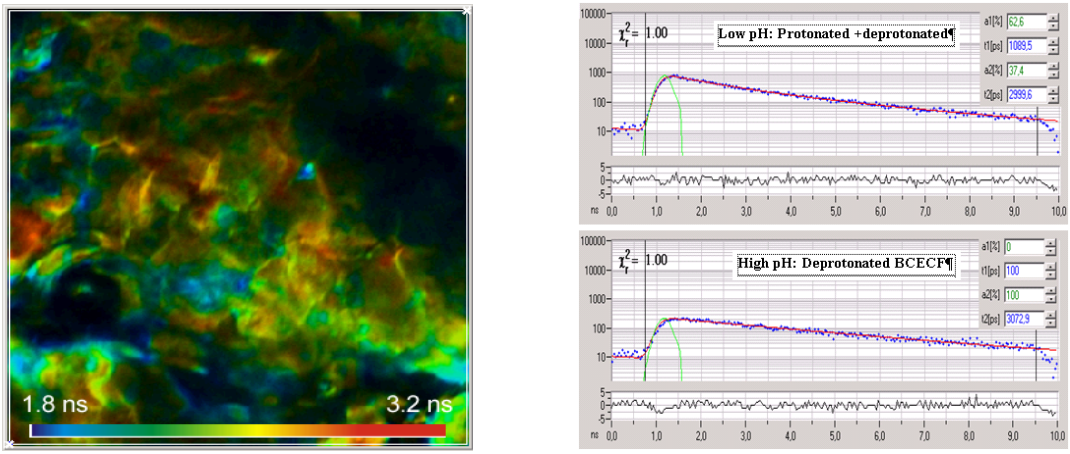


Fig. 65: Lifetime image of skin tissue stained with BCECF. The lifetime is an indicator of the pH. Right: Fluorescence decay curves in an area of low pH (top) and high pH (bottom). LSM 510 NLO, Data Courtesy of Theodora Mauro, University of San Francisco.

## *Calcium Imaging*

$Ca^{2+}$ ions are involved in a large number of cell functions, such as intracellular transport, membrane potential, muscle contraction, gene expression, and cell differentiation. There is a wide variety of $Ca^{2+}$ sensors [137], most of which change their fluorescence lifetime with the $Ca^{2+}$ concentration. The mechanism of the $Ca^{2+}$-dependent lifetime change is that the fluorophore has a Ca-bound and an Ca-unbound form of different fluorescence quantum efficiency and thus different fluorescence lifetimes. Consequently, the net fluorescence lifetime depends on the $Ca^{2+}$ concentration. An example of mapping of the $Ca^{2+}$ concentration by FLIM is shown in Fig. 66.

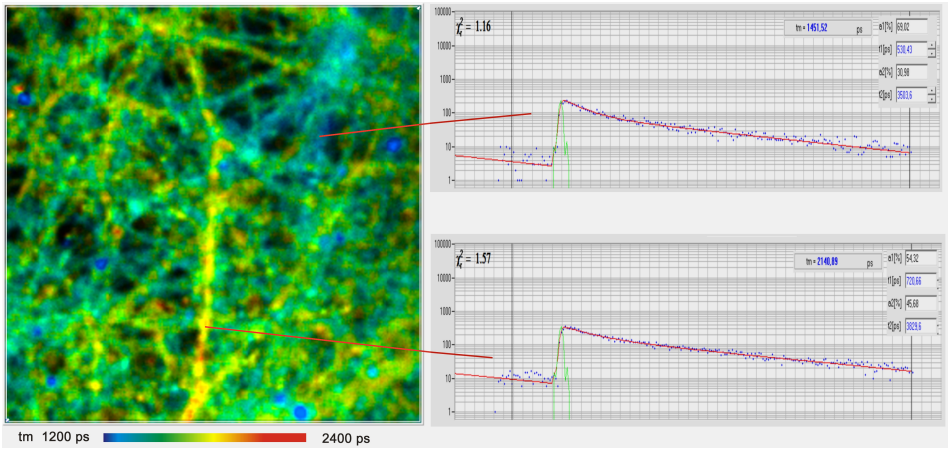


Fig. 66: FLIM image of cultured neurons stained with Oregon green OGB-1 AM. Colour range from τm = 1200 ps (blue) to 2400 ps (red). Decay curves of regions with low Ca (top) and high Ca (bottom) shown on the right. LSM 7 MP, Data courtesy of Inna Slutsky and Samuel Frere, Tel Aviv University, Sackler School of Medicine.

The $Ca^{2+}$ concentration in cells can change within remarkably short periods of time. The $Ca^{2+}$ response of live neurons to stimulation occurs within milliseconds. Nevertheless, the effects can be measured by FLITS [36, 88] and Temporal Mosaic FLIM [37, 40]. An example is shown in Fig. 67.

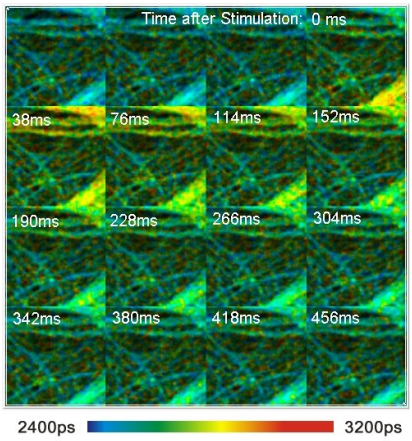


Fig. 67: Ca2+ transient in cultured neurons. Oregon Green Bapta, data recorded by temporal mosaic FLIM, 38 ms per mosaic element. Zeiss LSM 7 MP, bh Simple-Tau 152 TCSPC FLIM system.

Also other fluorophores, especially those with medium or low fluorescence quantum efficiency show variations of their fluorescence decay time depending on the local environment and the binding target [35, 39]. It is therefore likely that lifetime-based probes and markers can be found for a wide variety of cell and tissue parameters.

Lifetime imaging can also be used to obtain images of refractive index changes or viscosity changes in the vicinity of a fluorophore [108, 132, 139, 199]. Moreover, there are fluorophores that change their fluorescence behaviour depending on the redox potential of the local environment. An improved redox sensor based on a modified GFP (roGFPiE) was developed by Avezov et al. Test results obtained on various cells by TCSPC FLIM are described in [3].

Ion concentrations in cells can be influenced by physiological processes. Changes can be very fast, with transition times down to the millisecond range. The bh FLIM systems can record such changes by Mosaic FLIM and FLITS. Please see examples in Fig. 49, Fig. 50, and Fig. 51 in Section ‘FLIM Functions’.

## Förster Resonance Energy Transfer (FRET)

FRET is an interaction of two fluorophore molecules with the emission band of one dye overlapping the absorption band of the other. In this case the energy from the first dye, the donor, can be transferred to the second one, the acceptor. The energy transfer itself is a dipole-dipole interaction. It does not involve any light emission and absorption [84, 85, 137]. Fluorescence resonance energy transfer (FRET), or resonance energy transfer (RET), are synonyms of the same effect. The energy transfer rate from the donor to the acceptor decreases with the sixth power of the distance. Therefore it is noticeable only at distances shorter than 10 nm [137]. FRET results in an extremely efficient quenching of the donor fluorescence and, consequently, decrease of the donor lifetime, see Fig. 68, right.

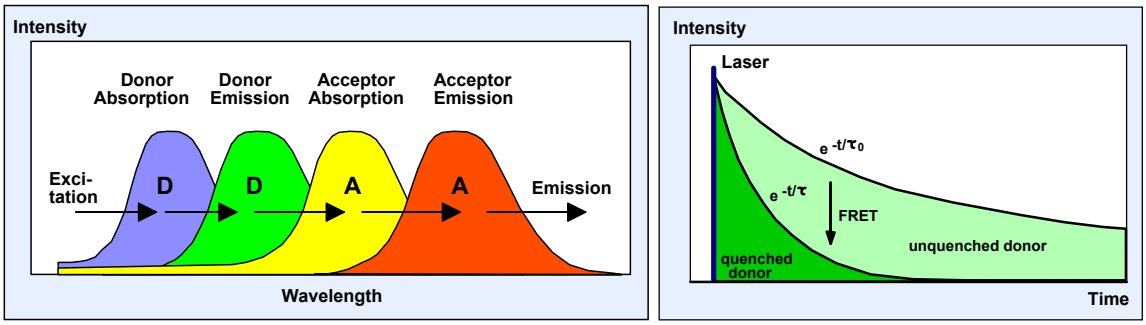


Fig. 68: Fluorescence resonance energy transfer

Because of its dependence on the distance FRET has become an important tool of cell biology [156, 157]. Different proteins are labelled with the donor and the acceptor; FRET is then used to verify whether the proteins are physically linked and to determine distances on the nm scale.

The problem of steady-state FRET techniques is that the concentration of the donor and the acceptor changes throughout the sample. The techniques therefore depend on ratios of the donor and acceptor intensities. However, the FRET-excited acceptor intensity is not directly available. There is ‘donor bleedthrough’ due to the overlap of the donor fluorescence into the acceptor emission band. For the CFP / YFP FRET system this signal component can be more than 30%. Moreover, some of the acceptor molecules are excited directly, not via energy transfer for the donor. Directly-excited acceptor fluorescence is a problem especially when the acceptor concentration is made high to guarantee that all acceptor targets are labelled. Steady-state FRET techniques therefore require careful calibration, including measurements of samples containing only the donor and only the acceptor.

The calibration problems can partially be solved by the acceptor photobleaching technique. An image of the donor is taken, then the acceptor is destroyed by photobleaching, and another donor image is taken. The increase of the donor intensity is an indicator of FRET. The drawback is that this technique is destructive, and that it is difficult to use in live cells. In fixed cells, however, the protein structure is changed already by the fixation so that the results are not necessarily correct.

All steady-state techniques have the problem that there is usually a mixture of interacting and non-interacting proteins. Both the fraction of interacting proteins and the distance between the proteins influence the FRET efficiency. It therefore cannot be told whether a variation in FRET efficiency is due to a variation in the distance or a variation in the fraction of interacting proteins.

## Single-Exponential FLIM FRET

The use of FLIM for FRET has the obvious benefit that the FRET intensity is obtained from a single lifetime image of the donor. Donor bleedthrough and directly excited acceptor fluorescence therefore have no influence of FLIM-FRET measurements. The only reference value needed is the donor lifetime in absence of the acceptor [53, 63, 82, 160]. It will be shown later that even this reference lifetime can be obtained from the FLIM-FRET data themselves.

Fig. 69 shows a single-exponential lifetime image of a cultured HEK (human embryonic kidney) cell expressing two interacting proteins labelled with CFP and YFP.

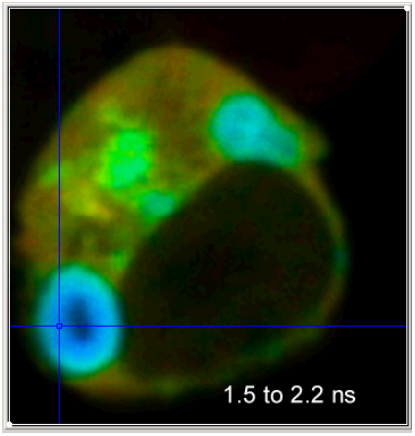


Fig. 69: FRET in an HEK cell. Blue to red corresponds to a lifetime range of 1.5 to 2.2 ns. (Christoph Biskup, University Jena, Germany)

The classic FRET efficiency can be directly calculated from the decrease in the fluorescence lifetime. Single-exponential lifetime images as the one shown in Fig. 69 are very useful to locate the areas in a cell where the labelled proteins interact. It has been shown that for a given efficiency of the optical system and detector and a given excitation power FLIM-based FRET measurements give better accuracy than steady-state techniques [154]. Single-exponential decay measurements do, however, not solve the general problem of the FRET techniques that the total decrease of the donor fluorescence intensity or fluorescence lifetime depends both on the distance of donor and acceptor and the fraction of interacting donor molecules. In the simplest case, a fraction of the donor molecules may not be linked to their targets, or not all of the acceptor targets may be labelled with an acceptor. This can happen especially in specimens with conventional antibody labelling [135]. But even if the labelling is complete not all of the labelled proteins in a cell are interacting, and the fraction of interacting protein pairs varies throughout the cell.

## Double-exponential FLIM FRET

TCSPC FLIM solves the problem of interacting and non-interacting donor by double-exponential lifetime analysis. The resulting donor decay functions can be approximated by a double exponential model, with a slow lifetime component from the non-interacting (unquenched) and a fast component from the interacting (quenched) donor molecules. If the labelling is complete, as it can be expected if the cell is expressing fusion proteins of the GFP variants, the decay components directly represent the fractions of interacting and non-interacting proteins. The composition of the donor decay function is illustrated in Fig. 70.

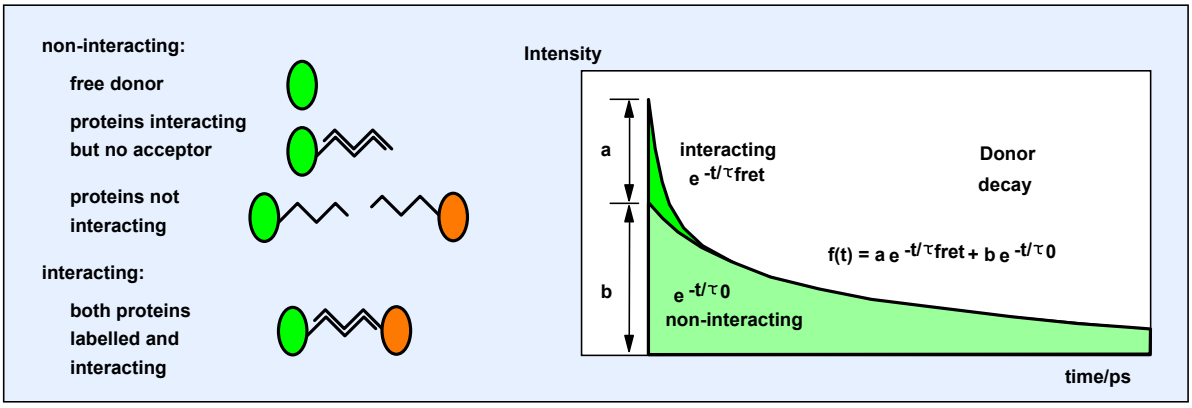


Fig. 70: Fluorescence decay components in FRET systems

Double exponential decay analysis delivers the lifetimes, $\tau_0$ and $\tau_{fret}$, and the intensity factors (amplitudes), a and b, of the two decay components. From these parameters can be derived the true FRET efficiency, $E_{fret}$, the ratio of the distance and the Förster radius, $r/r_0$, and the ratio of the number of interacting and non-interacting donor molecules, $N_{fret} / N_0$:

$$E_{fret} = 1 - \tau_{fret} / \tau_0$$

$$(r / r_0)^6 = \tau_{fret} / (\tau_0 - \tau_{fret}) \quad \text{or} \quad (r / r_0)^6 = \frac{1}{E_{fret}} - 1$$

$$N_{fret} / N_0 = a / b$$

Fig. 71 shows the fluorescence decay curves in a selected spot (array of 4 adjacent pixels, selected by the blue crosshair) of Fig. 69. The fluorescence decay is indeed double-exponential, with a fast lifetime component, $\tau_{fret}$, of 590 ps, and a slow lifetime component, $\tau_0$, of 2.41 ns.

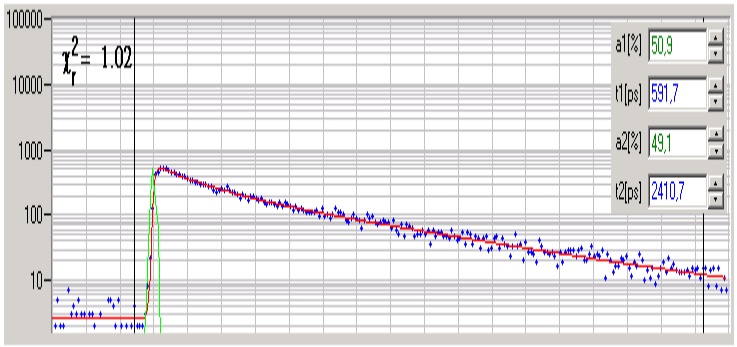


Fig. 71: Fluorescence decay curve in a selected spot of Fig. 69. The decay profile is clearly double-exponential.

Fig. 72 shows the result of a double-exponential analysis of the data. The left image shows the ratio of the lifetimes of the non-interacting and interacting donor fractions, $\tau_0 / \tau_{fret}$. The distribution of $\tau_0 / \tau_{fret}$ in different regions is shown far left. The locations of the maxima differ by only 10%, corresponding to a distance variation of about 2%. However, the variation in the intensity coefficients, a/b, is about 10:1.

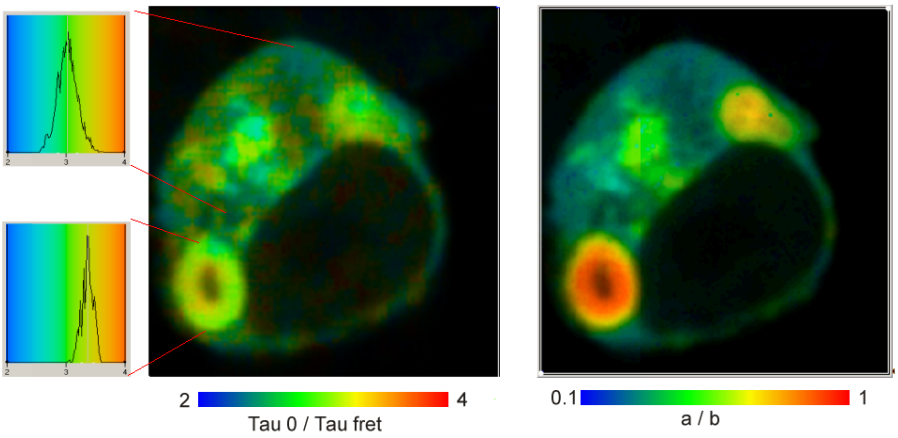


Fig. 72: FRET results obtained by double exponential lifetime analysis. Left: $\tau_0/\tau_{fret}$, Right: $N_{fret}/N_0$

The results show that the variation in the single-exponential lifetime (Fig. 69) is almost entirely caused by a variation in the fraction of interacting proteins, *not* by a change in distance. In other words, interpreting variations in the single-exponential lifetime (or classic FRET efficiencies from steady-state experiments!) as distance variations leads to wrong results.

Similar double exponential decay behaviour is commonly found in FRET experiments based on multi-dimensional TCSPC [4, 23, 24, 27, 53, 160]. Double-exponential decay profiles have also been confirmed by streak-camera measurements [52]. There is no doubt that the double-exponential behaviour is due to the presence of an interacting and a non-interacting donor fraction. It should be noted, however, that real FRET experiments can be more complicated. There is the problem that a protein can be expressing (or be labelled with) several donor or acceptor molecules. Energy may then migrate between the donors, and an the energy transfer rate may increase due to interaction with several acceptor molecules.

An enormous amount of FRET papers based on the bh FLIM technique has been published in the last few years. General characterisations of TCSPC-FLIM FRET for monitoring protein interactions can be found in [53, 63, 160]. An overview on monitoring HIV-1 Protein Oligomerization by FLIM FRET was given in [165]. FRET measurements by multi-wavelength FLIM are described in [54, 55].

Almost all of the FRET applications are more or less related to protein interactions or protein organisation, please see [1, 53, 60, 91, 105, 109, 134, 149, 155, 158, 184, 185, 192] for a (somewhat arbitrary) selection.

There is a number of FRET applications which are directly related clinical research [145]. Because FRET yields information about protein interaction it can be used to investigate the formation - and possible dissolution - of amyloid plaques of Alzheimer's disease [4, 4, 5, 48, 48, 49, 50, 107, 101, 107, 114, 142, 141, 142, 202, 219]. Mechanisms of Huntington disease (another progressive neuro-degenerative disorder) were investigated in [87] and [148].

Another potential application is the investigation of infection mechanisms. The technique was demonstrated by Ghukasyan et al. for the infection of HeLa cells with enterovirus 71 [97].

FLIM FRET applications in synaptic structures have been published in [58, 80, 86, 147, 200, 201]. These experiments are difficult because FRET occurs in sub-resolution volumes of the sample. Nevertheless, Bosch et al. were not only able to detect protein interaction, they could even observe the re-organisation of post-synaptic substructures during long-term potentiation by time-series FLIM [58]. Fogel used a combination of intensity FRET measurement, FLIM FRET measurement, and single-

molecule imaging to show that the amyloid precursor protein homo-dimer constitutes a resynaptic receptor that transduces a signal from amyloid-beta peptides to glutamate release [86].

There are currently a number of attempts to detect FRET between endogenous fluorophores, and use the results to gain structural information about proteins and protein complexes. The problem is that these fluorophores are hard to reach by one-photon and even two-photon excitation. It has been shown recently that three-photon excitation of tryptophane - and the detection of its fluorescence - is possible with the Zeiss LSM 710/780/880 NLO microscopes. With UV-optimised optics in the NDD beam path, hybrid detectors, and carefully adjusted laser power three-photon excited TCSPC FLIM images of tryptophane were obtained. FRET was expected to occur between the tryptophane and the bound component of the NADH. Indeed, FLIM experiments have shown a decrease in the tryptophane lifetime correlated with an increase in the bound-unbound ratio of the NADH [2, 115, 157].

For a detailed description of FLIM FRET and a review of the related literature please see 'The bh TCSPC Handbook', 6th edition, 2015 [37] and 'FLIM Systems for Zeiss LSM 710/780/880 microscopes' [6].

## Autofluorescence Microscopy of Cells and Tissue

Biological tissue contains a wide variety of endogenous fluorophores [71, 99, 124, 164, 173]. For many years, autofluorescence measurements of cells and tissue have mainly been performed by spectrally resolved imaging techniques. The problem of purely spectrally resolved techniques is that the emission and excitation spectra of the endogenous fluorophores are broad and poorly defined. Many of the fluorophores are mixtures of closely related compounds. The shape of the spectra can therefore vary. Moreover, absorbers present in the tissue may change the apparent fluorescence spectra. It is therefore difficult to disentangle the fluorescence components by their emission spectra alone. The most serious drawback of purely spectral techniques is, however, that different binding states of fluorophores cannot be distinguished.

Fluorescence lifetime imaging is likely to improve the contrast of separation of the different fluorophores. This has been demonstrated by Krasieva et al. [130] who used TCSPC FLIM and phasor plot analysis to separate the fluorescence components of different melanin types, and the melanin fluorescence form the NADH fluorescence. The most important argument for using lifetime imaging is, however, that the lifetimes of many endogenous fluorophores depend on local environment parameters, such as pH, oxygen saturation, and on the binding to proteins. Autofluorescence lifetime detection therefore not only adds an additional separation parameter but also yields direct information about the metabolic state, the microenvironment, and the binding state of the endogenous fluorophores. There is a steadily increasing number of papers about this subject [51, 57, 64, 65, 102, 136, 137, 146, 153, 159, 168, 174, 188, 189, 196, 197, 203, 205, 206, 207, 213].

Autofluorescence imaging has also benefits in cases when the reaction of tissue to optical radiation is to be investigated, such as skin ageing [170] or photodamage and tumor induction by UV [123] and IR irradiation [126]. Such experiments forbid the use of exogenous fluorophores because energy or electron transfer between the fluorophores and the proteins can induce photoreactions. Moreover, TCSPC FLIM is more and more introduced into clinical applications [72, 124, 125, 127, 166, 170, 171, 173, 174, 174]. In these applications 'label-free' imaging is needed because staining the tissue with exogenous fluorophores is either not possible or not permitted.

## NADH and FAD Lifetime Imaging

The use of fluorescence-lifetime variations is especially promising for NADH and FAD. These coenzymes are involved in the electron transfer mechanism of the cell metabolism. Both NADH and FAD form redox pairs. NADH is fluorescent in its reduced form but loses fluorescence when oxidised. FAD is fluorescent when oxidised, and loses fluorescence when reduced. The fluorescence intensity ratio of NADH and FAD therefore changes with the redox state of the tissue. Chance et al. defined a 'Redox Ratio' that shows whether the metabolism in a cell is more oxidative (phosphorylation) or more reductive (glycolysis) [61, 62]. Measurements of the redox state are related to the 'Warburg Effect': Normal cells have an oxidative, cancer cells a reductive metabolism [210, 211]. For practical applications please see [190, 191, 204].

*Redox Ratio*

The influence of the redox state can be shown by recording FLIM from yeast cells. Fig. 73, left, shows yeast cells in a medium saturated with $CO_2$ and virtually free of oxygen. Except for a few (probably apoptotic) cells the fluorescence is extremely week. When the sample has taken up oxygen from the air the fluorescence intensity increases, accompanied by a change in the lifetimes.

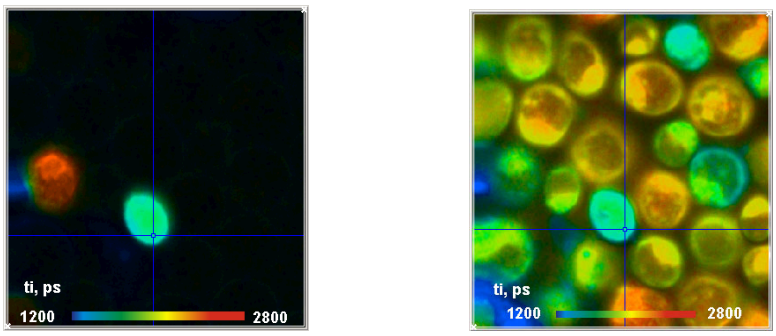


Fig. 73: Yeast cells in a cell dish saturated with $CO_2$ (left) and saturated with $O_2$ (right). Confocal FLIM, excitation 405 nm, detection by bh MW FLIM, 540 nm

*NADH Lifetimes*

It is known that the fluorescence lifetimes of NADH and FAD depend on the binding to proteins [136, 137, 153]. Unbound NADH has a fluorescence lifetime of about 0.4 ns. When NADH binds to proteins the lifetime typically increases to about 1.2 ns [137]. However, the bound-NADH lifetime depends on the proteins, and can reach 4 to 5 ns [137]. For FAD the effect of binding is opposite: Bound FAD has a lifetime of a few 100 ps, unbound FAD of a few ns.

The fluorescence decay parameters, especially those of NADH, can thus be used to obtain information about the binding state of NADH. The ratio of bound and unbound NADH depends on the metabolic activity. The NADH lifetime or, better, the amplitude ratio of the two decay components is therefore an indicator of the metabolic state. This information is not available from fluorescence spectra or fluorescence intensity images. Additional information about NADH binding can be obtained by recording also fluorescence anisotropy decay data of intracellular NADH [106, 203, 215]

An overview on NADH / FAD fluorescence dynamics has been given by Chorvat and Chorvatova [67] and by Heikal at al. [106]. Ghukasyan and Kao [98] have shown that the NADH decay parameters, in particular amplitudes of the fast and slow lifetime components, are indicators of physiological and pathological states of the cells. Differentiation between apoptosis and necrosis by the NADH lifetime components was descried by Wang et al. [209].

Skala et al. [188, 189] used two-photon excited autofluorescence FLIM to record lifetime images of NADH in normal and pre-cancerous epithelia. They found a significantly decreased lifetime of the slow decay component of (bound) NADH, in precancerous tissue. A significant decrease of the lifetime of the protein-bound FAD was detected in high-grade pre-cancers [189]. Bird et al. used a similar approach for metabolic mapping of human breast cells [51].

Szaszak et al. [197] used the NADH fluorescence to track metabolic changes in the host and in the pathogen during intracellular infectious by *chlamydia trachomatis*.

Kantelhardt et al. [118] and Leppert et al. [138] recorded two-photon excited lifetime images of glioma and the surrounding brain tissue. They found a significantly increased mean (amplitude-weighted) lifetime for the glioma cells compared to the surrounding brain cells.

Metabolic imaging of melanoma progression was performed by Pastore et al. [151]. They confirm a significant increase in the unbound / bound (a1/a2) ratio of NADH with the growth of a melanoma tumor, while the lifetimes of the decay components remained constant.

*OMI Index*

Skala and Walsh combined the normalised value of the redox ratio RR, the normalised amplitude-weighted fluorescence lifetime, $\tau_{m\ NADH,}$ and the normalised $\tau_{m\ FAD,}$ of NAD(P)H and FAD into a single 'Optical Molecular Imaging', or OMI index. High OMI means a shift toward glycolysis and cancer metabolism.

$OMI = RR + \tau_{m\ NADH} - \tau_{m\ FAD}$ (all parameters normalised to reference values)

The OMI index turned out to be a robust parameter to characterise the metabolism of a cell. The authors use it successfully to check the response of human cancer cells from clinical biopsies to various anti-cancer drugs. The cells are cultured, the cell cultures are treated with the drugs, the cells are repeatedly imaged by FLIM, and the OMI index is used as an indicator of the response to the drugs [204, 205, 206, 207, 208]. Within a few days, the most efficient drug can be determined and a treatment strategy for the patient be developed. The technique has the potential to revolutionise cancer therapy, and, notably, can be performed by a normal bh FLIM system in combination with a two-photon laser scanning microscope.

*Response to Drugs*

NADH FLIM is closely related to effect of cancer drugs in chemotherapy. Skala and Walsh used it to evaluate the effect of different cancer drugs on cells from biopsies from patients, and to develop the best treatment strategy, see above. Stunz et al. [194] studied the response of cultured rat astrocytes and neurons to manganese treatment.

Shirmanova et. al. [187] demonstrated the relationships between the intracellular pH and the metabolic state derived from NAD(P)H / FAD FLIM in response to treatment with cisplatin. They found a metabolic shift from glycolysis towards oxidative metabolism during cisplatin-induced inhibition of cancer cell growth in vitro and in vivo.

Sergeeva et al. [183] performed metabolic imaging of NAD(P)H and FAD, and simultaneously used the genetically encoded pH-indicator SypHer1 and the FRET-based mKate2-DEVD-iRFP sensor for pH imaging and caspase-3 activity imaging. They found a relationship between the metabolic state derived from NAD(P)H FLIM, intracellular pH and caspase-2 activation during apoptosis. Induction of apoptosis was accompanied by a switch to oxidative phosphorylation, cytosol acidification and caspase-3 activation.

The effect of Ouabain, a pharmaceutical drug, and of 4-hydroxynonenal on live cardio-myocytes was studied by Chorvatova et al., see [69] and [70].

*Stem Cells Research*

Gou at al. used FLIM of the decay components of NADH to distinguish human mesenchymal stem cells from differentiated progenies [103]. Uchugonowa & König applied two-photon autofluorescence lifetime imaging to human and animal stem cells [127, 128]. They found significant changes in the fluorescence lifetimes on differentiation and maturation of the cells. An example is shown in Fig. 74. The differentiated cells have smaller $a_1/a_2$ ratios and longer mean lifetime, $t_m$.

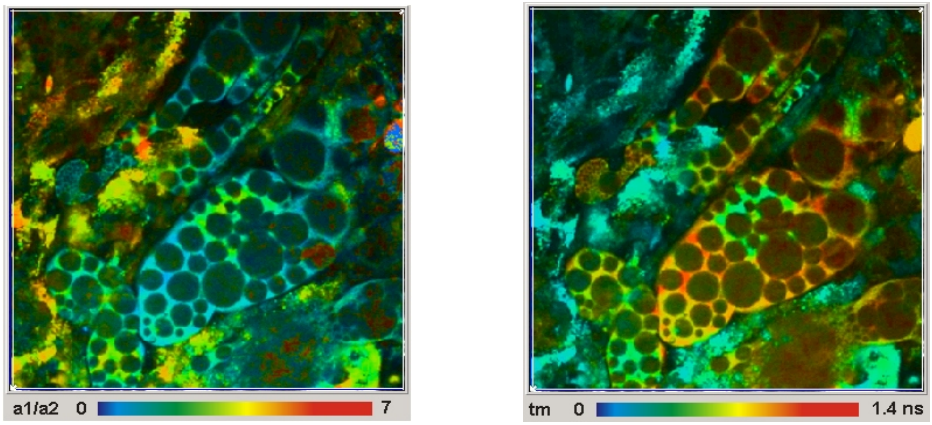


Fig. 74: FLIM of human salivary gland stem cells. Differentiated cells have significantly lower a1/a2 ratio and longer mean lifetime. Data courtesy of Aisada Uchugonova and Karsten König, Saarland University, Saarbrücken.

## NADH / FAD Multi-Wavelength FLIM

A problem of NADH / FAD FLIM is that there is a strong overlap in the excitation and emission spectra [137]. An improvement can be achieved by using the bh multi-wavelength FLIM detector [30, 167]. Fig. 75 shows autofluorescence FLIM data of a fresh mouse kidney section recorded by a bh MW-FLIM system. Two-photon excitation at a wavelength of 750 nm was used. Each of the images covers a wavelength range of about 12.5 nm. The colour of the images represents the lifetime obtained from a single-exponential fit.

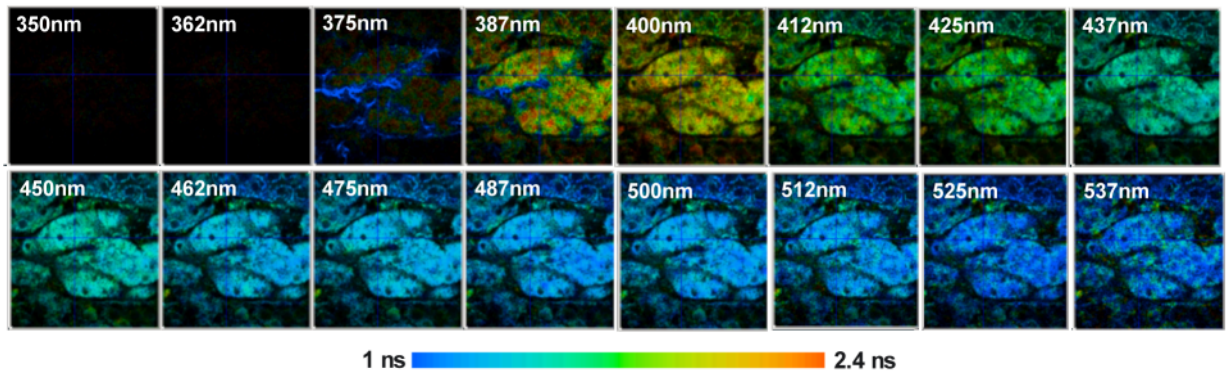


Fig. 75: Multi-wavelength fluorescence lifetime images of a mouse kidney section. Two-photon excitation at 750 nm. Images in subsequent wavelength intervals from 350 nm to 550 nm. (Christoph Biskup, University Jena, Germany)

Due to the different fluorophores present in the tissue, the lifetimes in the individual wavelength intervals are different. The third left image contains a strong SHG component. SHG reveals itself as an infinitely short lifetime component, see the blue features in the third to left image.

An interesting application of multi-wavelength lifetime detection of NADH has been published by Chorvat et al. [68]: The authors used the data to detect early stages in the metabolism of isolated live cardiomyocytes during rejection of transplanted hearts. The effect of Ouabain, a pharmaceutical drug, on live cardiomyocytes was studied by Chorvatova et al., see [69].

An overview about autofluorescence multi-wavelength FLIM is given in [67]. Full exploitation of multi-wavelength autofluorescence FLIM data requires a global fit with a suitable model that includes the effective spectra of the expected fluorophores. The task is extremely difficult because some of the endogenous fluorophores are in fact mixtures of slightly different compounds, with different absorption and emission spectra [174]. Moreover, there may be absorbers of unknown absorption spectra, inhomogeneous distribution, and unknown concentration in the tissue. Nevertheless, there is currently a number of approaches that are likely to solve at least a part of the problem [65, 66, 67, 161].

## Two-Photon FLIM of Skin

A promising application of two-photon excited FLIM measurements of tissue autofluorescence is optical tomography of skin [121, 124, 125]. The technique has reached the state of clinical evaluation, and there is a growing number of publications in this field [72, 127, 152, 166, 170, 171]. Multiphoton FLIM images of skin are surprisingly rich in detail, both in terms of morphological and fluorescence-lifetime information. An example is shown in Fig. 76.

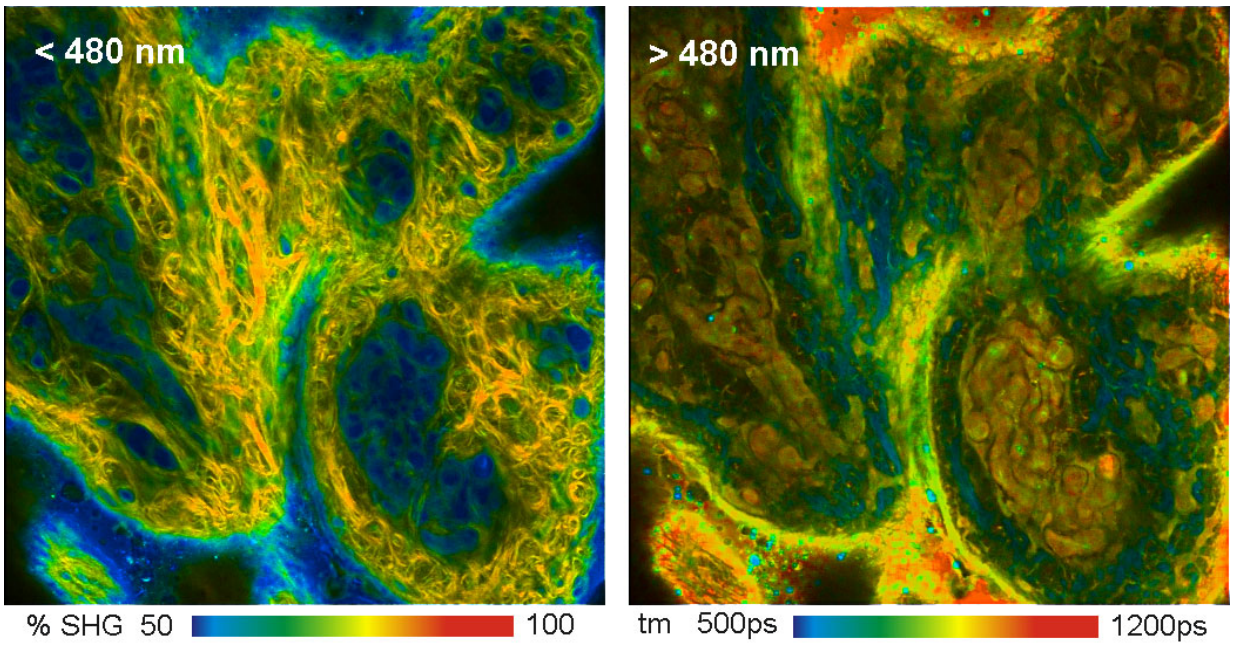


Fig. 76: Two-photon FLIM of pig skin. LSM 710 NLO, excitation 800nm, HPM-100-40, NDD. Left: Wavelength channel <480nm, colour shows percentage of SHG in the recorded signal. Right: Wavelength channel >480nm, colour shows amplitude-weighted mean lifetime.

Measurements as the ones described above can favourably be performed by Z stack FLIM. Fig. 77 shows Z-stack FLIM data of a pig skin sample in the wavelength channel above 480 nm. The data were analysed by the batch-processing function of the SPCImage. The colour of images shows the average (intensity-weighted) lifetime of a double-exponential decay fitted to the decay data. The intensity of the images was normalised to the intensity of the brightest pixel.

Fig. 78 shows the SHG intensity extracted from the FLIM data in the channel below 480 nm. Also here, intensity of the images was normalised to the intensity of the brightest pixel.

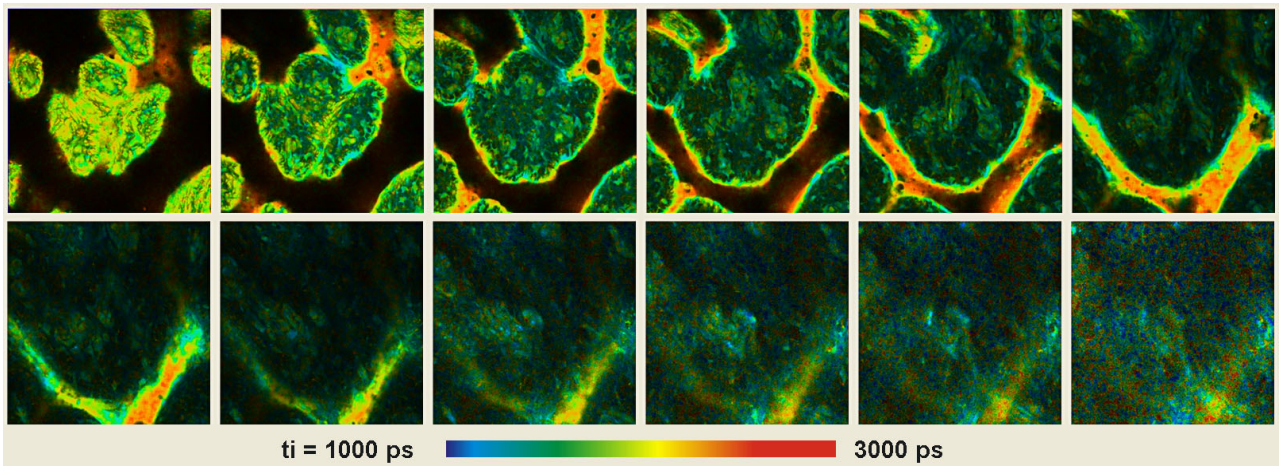


Fig. 77: FLIM Z stack recorded at a pig skin sample, excitation at 800 nm, emission above 480 nm. Z step width 5.09 µm, scan area 212 x 212 µm. Images from 5 µm to about 60µm below the surface. Colour represents average (intensity-weighted) lifetime of a double-exponential fit. FLIM data format 256 x256 pixels, 256 time channels. Normalised intensity.

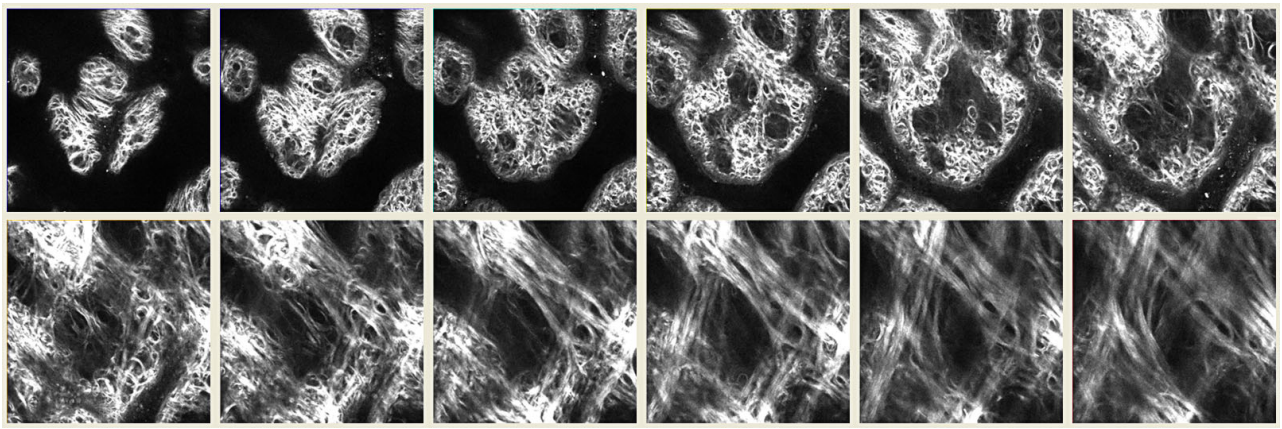

Fig. 78: Z stack recorded at a pig skin sample, excitation at 800 nm, emission below 480 nm, SHG signal, extracted by selecting photons in an early time window. Z step width is 5.09 µm, scan area 212 x 212 µm. Images from 5 µm to about 60µm depth. Normalised intensity.

In all autofluorescence lifetime experiments it is important that the metabolism of the tissue be not changed before or during the measurement. This is critical especially for ex-vivo samples. Sanchez et al. have therefore studied the degradation of skin samples over the storage time and under different storage conditions [169].

## Autofluorescence of the Ocular Fundus

TCSPC FLIM has recently be introduced in ophthalmic scanners. The instruments have produced FLIM images of amazing quality. Clinical trials have shown that FLIM is able to detect metabolic changes that are early indications of a number of eye diseases [83, 173, 174, 176, 177, 174, 176, 177, 179, 180, 181]. Ophthalmic FLIM has produced absolutely tantalizing results. Ophthalmic scanner do, however, not deliver spatial resolution at the cell level. Clinical research has therefore to be supported by FLIM microscopy of ex-vivo samples. A FLIM study of extra-macular drusen has been published

by Schweitzer et al. [178]. Based on the FLIM data, the authors were able to clearly discriminate the RPE from Bruch's membrane, drusen, and choroidal connective tissue. An example of a FLIM image of the RPE with hard drusen is shown in Fig. 79.

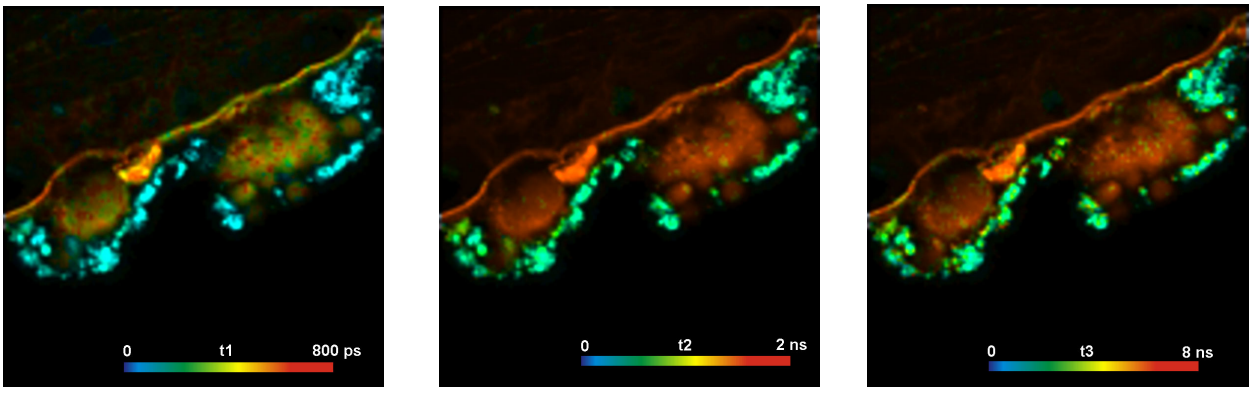


Fig. 79: Autofluorescence FLIM image of a human fundus sample. Triple-exponential analysis, left to right: Lifetimes of the fast, medium, and slow decay component. Courtesy of Dietrich Schweitzer, Martin Hammer, Sven Peters, Christoph Biskup, University Jena, Germany. LSM 710, bh MW FLIM detector and SPC-150 TCSPC module.

The data were acquired with the MW FLIM multi-wavelength detector. The figure shows the lifetime data in all combined wavelength channels. Triple-exponential decay analysis was used; the images show the fast decay component, the medium component, and the slow decay component. Interestingly, in the drusen and in the Bruch's membrane an extremely slow component with about 8 ns decay time occurs. The lifetimes in the RPE are much shorter.

Spectrally resolved data are shown in Fig. 80. It shows 6 consecutive wavelength channels of the MW FLIM detector from 450 nm to 575 nm. The lifetime shown is the amplitude weighted average of a triple-exponential decay model. The intensities were normalised to the brightest pixel.

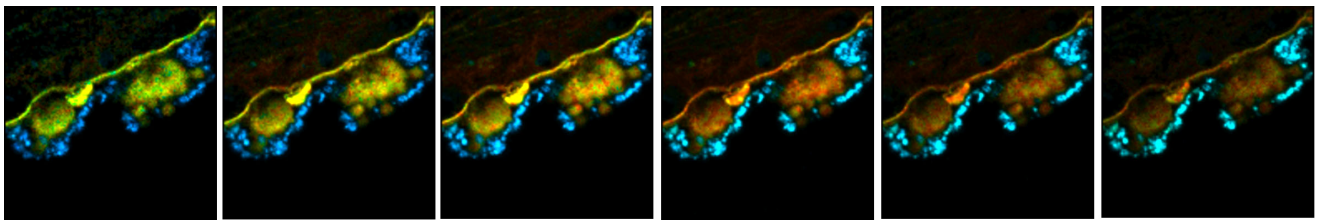

Fig. 80: Lifetime images of the amplitude-weighted lifetime, tm, for single wavelength channels from 450 nm to 575 nm. The lifetime scale is blue to red, 0 to 2500 ps. LSM 710, bh MW FLIM detector and SPC-150 TCSPC module.

## FLIM of Other Endogenous Fluorophores

There are other endogenous fluorophores which can possibly be used for the identification of the tissue state and of cancerous and pre-cancerous situations. Melanin and its relationship to melanoma has been described above. The use of the tryptophane fluorescence, including FRET from tryptophane into NAD(P)H has been described in [2, 115, 157]. The problem of tryptophane is that it cannot easily be excited by wavelength available in one-photon and two-photon laser microscopes. The authors therefore used three-photon excitation. FLIM with endogenous bilirubins has been described by Shen et al. [186]. Bilirubin is present at high concentration in liver tissue. The authors excited it by two-photon excitation at 1230 nm. In differentiated hepatocellular carcinoma they found a fluorescence lifetime of 500 ps compared to 300 ps in non-tumor tissue. Endogenous fluorescence is also recorded from porphyrines. Porphyrines exhibit a strongly multi-exponential fluorescence decay which

indicates that they are a mixture of slightly different compounds, different conformations, or, possibly, aggregates of different size. The composition of these mixtures may depend on the tissue state. The composition of the decay function may therefore contain biological information. Other endogenous fluorophores, such as lipofuscin or advanced glycation end products (AGEs) are important as indicators in ophthalmic FLIM [37, 181].

## Diffusion of Nanoparticles in Skin

An important issue in dermatology is diffusion of drugs and nano-particles through human skin. On the one hand, diffusion through the skin may be desirable as a way of drug delivery. On the other hand, nanoparticles contained in sunscreens or cosmetic products should not permeate through the stratum corneum of human skin. Moreover, it is important whether the nanoparticles cause changes in their molecular environment. The use of two-photon imaging and FLIM to study these effects has been described in [95, 140, 162, 166, 171].

## NADH FLIM with Oxygen Sensing by PLIM

Cancer cells and normal cells can be distinguished by recording NADH FLIM images, and determining either the amplitude-weighted lifetime or (more accurately) the amplitude ratio of the fast and slow decay component. The amplitude ratio reflects the metabolic state of the cell. Cancer cells are preferentially running glycolysis, normal cells oxidative phosphorylation. However, the metabolic state of a cell also varies with the oxygen concentration (or the oxygen partial pressure). It is therefore important to track the oxygen concentration simultaneously with the NADH FLIM recording. The oxygen concentration can be obtained from PLIM data of an exogenous phosphorescence dye. Due to its high sensitivity and its ability to record FLIM and PLIM simultaneously the bh FLIM/PLIM technique is excellently suitable for these applications, and the number of publications is steeply increasing.

The first publications concentrated on the characterisation of phosphorescent probes. In [78] and [81] Dmitriev and Papkovski give a summary on available phosphorescent probes, their $O_2$ sensitivity, brightness, phosphorescence lifetimes, cell-staining capability, and toxicity.

The problem of sensitivity of phosphorescent dyes to other cell parameters, such as pH, viscosity, and oxygen diffusion time constant, is addressed by embedding the dyes in nanoparticles and nanostructured cell substrates. Phosphorescent nanoparticles, nanostructured films, scaffolds and fibres as pO2-sensors are explored in [77, 79, 110, 111, 150, 198, 214]. Phosphorescent gold clusters as probes for lipid droplets were described in [129].

Oxygen imaging of neurospheres is described in [76]. Applications to Giant Umbrella Cells and to healthy and inflamed colon tissue are described in [216] and [218]. Changes in intracellular oxygen concentration with the metabolic activity were observed by Zhdanov et al. [217]. Jenkins et al. studied the function of SPCA ATPases in HCT116 cells. They found correlations of the expression of SPCA1 and SPCA2 with the $O_2$ concentration [112].

Kurokawa et al. [133] provided a detailed evaluation of TCSPC PLIM with Platinum(II) 5,10,15,20-tatrakis-[4-carboxyphenyl)porphyrin. They tested the sensor with MKN45 cells, colon26 spheroids under different $O_2$ concentration. They were able to correlate low pO2 regions with mitochondria, to track the change in $O_2$ concentration in Colon26 cells after addition of antimycin A, and to visualise the $O_2$ change in MIN6 cells after glucose stimulation.

Simultaneous measurements of NADH FLIM and PLIM and the correlation of metabolic parameters and $O_2$ concentration were published first by Kalinina et al. [116]. The authors observed changes in the NADH lifetime with the $O_2$ concentration and after addition of antimycin A. Changes of the NADH decay functions with the intracellular O2 concentration were also demonstrated by Shcheslavskiy et al. [182].

Lukina et al. [143] used a fibre-based TCSPC system with implantable fibre tips [37] to record NAD(P)H decay curves simultaneously with phosphorescence decay curves of an oxygen sensor in mouse tumors. The authors found characteristic changes in the NADH decay parameters and the $O_2$ concentration between healthy tissue and tumor tissue.

## Plant Physiology

Plant tissue contains a large number of endogenous fluorophores. In practice the fluorescence is dominated by the fluorescence of chlorophyll and the fluorescence of flavines. The flavines emit in a broad range from about 480 nm to 580 nm. Chlorophyll is excited at any wavelength throughout the visible spectrum and emits a strong fluorescence signal around 700 nm. FLIM images recorded with the bh multi-spectral FLIM system at a Zeiss LSM 710 NLO are shown in Fig. 81.

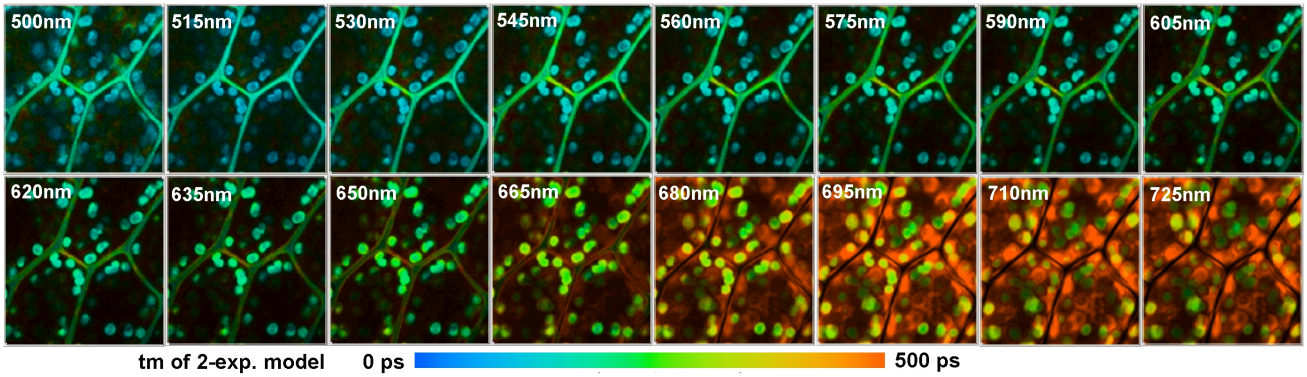


Fig. 81: Multi-spectral FLIM of plant tissue. Moss leaf, LSM 710 NLO, two-photon excitation at 850 nm. Amplitude-weighted mean lifetime of double-exponential fit. Intensity normalised to brightest pixel of each wavelength interval.

The fluorescence of chlorophyll competes with the energy transfer into the photosynthesis channels. Thus, the fluorescence lifetime is a sensitive indicator of the photosynthesis efficiency. Therefore, the fluorescence lifetime of the chlorophyll in live plant tissue not only depends on the state of the tissue but also on the light intensity, and the time of exposure.

The changes in the fluorescence intensity of chlorophyll with the exposure to light have been found 1931 by Kautsky and Hirsch [120]. The effects have been termed fluorescence induction, fluorescence transients, or Kautsky effect [96, 144]. When a dark-adapted leaf is exposed to light the intensity of the chlorophyll fluorescence starts to increase. After a steep rise the intensity falls again and finally reaches a steady-state level. The rise time is of the order of a few milliseconds to a second, the fall time can be from several seconds to minutes.

The initial rise of the fluorescence intensity is attributed to the progressive closing of reaction centres in the photosynthesis pathway. Therefore the quenching of the fluorescence by the photosynthesis decreases with the time of illumination, with a corresponding increase of the fluorescence intensity. The fluorescence quenching by the photosynthesis pathway is termed ‘photochemical quenching’. The slow decrease of the fluorescence intensity at later times is termed ‘non-photochemical quenching’. It is believed that it is a mechanism the plant uses to protect itself from photodamage. Because the

chlorophyll transients are closely related to the metabolism of the plant they are a far better indicator of the health state than the fluorescence lifetime itself [28, 37].

By using a fast scan and a reasonable short acquisition time non-photochemical transients can be measured by time-series FLIM [6, 119]. After getting the sample in the focus the sample is shifted to an area that has not been exposed to light. Then a time-series of FLIM images is recorded. A typical result is shown in Fig. 82. The acquisition time per image was 1 second, the image size 256 x 256 pixels x 64 time channels. The illumination by the laser initiates an increase in non-photochemical quenching. The result is a decrease in the fluorescence lifetime of the chloroplasts which can clearly be seen in Fig. 82.

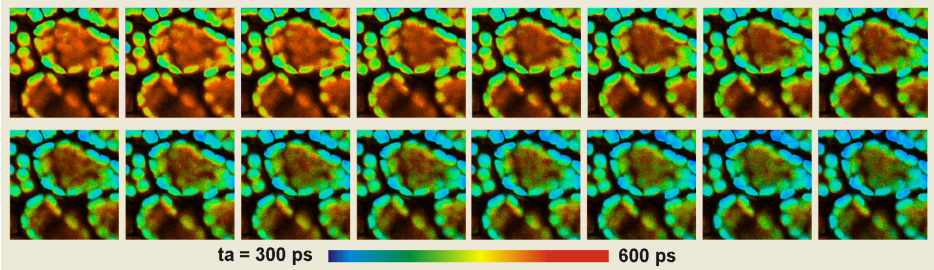


Fig. 82: Change of the fluorescence lifetime of chlorophyll with time of exposure. Moss leaf, 1-photon excitation at 445 nm, 256x256 pixels.

The lifetime changes of chlorophyll can also be recorded by temporal mosaic FLIM, see page 31. Non-repeatable processes can be recorded at a speed of about two images per second. Repeatable processes can be recorded at images rates down to the sub-50 ms range. Even faster effects can be recorded by FLITS. The technique records transient effects in the fluorescence lifetime of a sample along a one-dimensional scan. An example is shown in Fig. 83. It shows decay curves for one location within the line for times of 0.4 s, 8 s, and 14 s after the turn-on of the laser. The mean lifetimes, tm, obtained from a double-exponential fit are 862 ps, 471 ps, and 402 ps, respectively. The changes in the decay profiles are clearly visible.

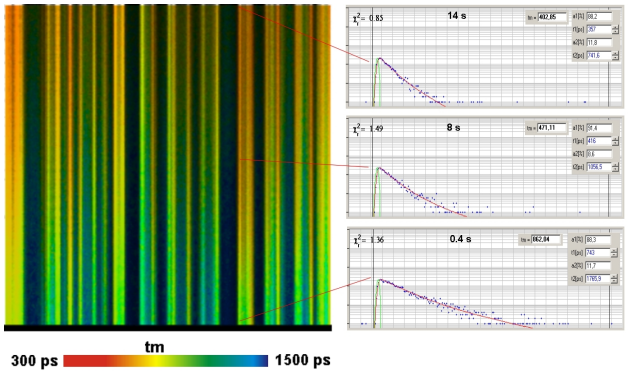


Fig. 83: Decay curves for a selected pixel within the line for times of 0.4 s, 8 s, and 14 s after the turn-on of the laser

FLITS can even be used to record the photochemical transients. A time resolution of about 1 millisecond is required. To obtain enough photons within a time interval this short the laser must be on-off modulated and the data acquired over a large number of on-off periods. Please see [37, 33] for details.

# References


1. K. Amari, E. Boutant, C. Hofmann, C. Schmitt-Keichinger, L. Fernandez-Calvino, P. Didier, A. Lerich, J. Mutterer, C. L. Thomas, M. Heinlein, Y. Mely, A. J. Maule, C. Ritzenthanler, A family of plasmodesmal proteins with receptor-like properties for plant viral movement proteins. PLOS Pathogens 6 e1001119-1 to -10 (2010)
2. S. R. Alam, H. Wallrabe, Z. Svindrych, A. K. Chaudhary, K. G. Christopher, D. Chandra, A. Periasamy, Investigation of Mitochondrial Metabolic Response to Doxorubicin in Prostate Cancer Cells: An NADH, FAD and Tryptophan FLIM Assay. Scientific Reports 7 (2017)
3. E. Avezov, B.C.S. Cross, G.S. Kaminski Schierle, M. Winters, H. P. Harding, E. Pinho Melo, C. F. Kaminski, D. Ron, Lifetime imaging of a fluorescent protein sensor reveals surprising stability of ER thiol redox. J. Cell Biol. 201, 337-349 (2013)
4. B. J. Bacskai, J. Skoch, G.A. Hickey, R. Allen, B.T. Hyman, Fluorescence resonance energy transfer determinations using multiphoton fluorescence lifetime imaging microscopy to characterize amyloid-beta plaques, J. Biomed. Opt 8, 368-375 (2003)
5. B. J. Bacskai, J. Skoch, G.A. HickeyO. Berezovska, B.T. Hyman, Multiphoton imaging in mouse models of Alzheimer's disease, Proc. SPIE, 5323, 71-76 (2004)
6. Becker & Hickl GmbH, Modular FLIM systems for Zeiss LSM 710/780/880 family laser scanning microscopes. User handbook, 7th ed., available on www.becker-hickl.com, please contact bh for printed copies
7. Becker & Hickl GmbH, FLIM systems for Zeiss LSM 980. Addendum to handbook for modular FLIM systems for Zeiss LSM 710/780/880 family laser scanning microscopes 7th ed., available on www.becker-hickl.com, please contact bh for printed copies
8. Becker & Hickl GmbH, SPCImage NG Next Generation FLIM data analysis software. Overview brochure, 20 pages, available on www.becker-hickl.com.
9. Becker & Hickl GmbH, LHB-104 Laser Hub. User manual, available on www.becker-hickl.com.
10. W. Becker, Bigger and Better Photons: The Road to Great FLIM Results. Available on www.becker-hickl.com.
11. Becker & Hickl GmbH, Burst Analyser 2.0, for correlation analysis and single-molecule spectroscopy. Available on www.becker-hickl.com
12. Becker & Hickl GmbH, Becker & Hickl GmbH, Megapixel FLIM with bh TCSPC Modules - The New SPCM 64-bit Software. Application note, available on www.becker-hickl.com
13. Becker & Hickl GmbH, FLIM with NIR Dyes. Application note, available on www.becker-hickl.com
14. Becker & Hickl GmbH, Multiphoton NDD FLIM at NIR Detection Wavelengths with the Zeiss LSM 7MP and OPO Excitation. Application note, available on www.becker-hickl.com
15. Becker & Hickl GmbH, Zeiss BiG-2 GaAsP Detector is Compatible with bh FLIM Systems. Application note, available on www.becker-hickl.com
16. Becker & Hickl GmbH, Simultaneous Phosphorescence and Fluorescence Lifetime Imaging by Multi-Dimensional TCSPC and Multi-Pulse Excitation. Application note, available on www.becker-hickl.com
17. Becker & Hickl GmbH, New SPCImage Version Combines Time-Domain Analysis with Phasor Plot. Application note, available on www.becker-hickl.com
18. Becker & Hickl GmbH, Sub-20ps IRF Width from Hybrid Detectors and MCP-PMTs. Application note, available on www.becker-hickl.com
19. Becker & Hickl GmbH, SPCM Software Runs Online-FLIM at 10 Images per Second. Application note, available on www.becker-hickl.com
20. Fast-Acquisition TCSPC FLIM System with sub-25 ps IRF width. Application note, available from www.becker-hickl.com
21. Fast-Acquisition Multiphoton FLIM with the Zeiss LSM 880 NLO. Application note, available from www.becker-hickl.com
22. Fast-Acquisition TCSPC FLIM: What are the Options? Application note, available from www.becker-hickl.com
23. W. Becker, K. Benndorf, A. Bergmann, C. Biskup, K. König, U. Tirlapur, T. Zimmer, FRET measurements by TCSPC laser scanning microscopy, Proc. SPIE 4431, 94-98 (2001)
24. W. Becker, A. Bergmann, K. König, U. Tirlapur, Picosecond fluorescence lifetime microscopy by TCSPC imaging, Proc. SPIE 4262, 414-419 (2001)
25. W. Becker, A. Bergmann, C. Biskup, T. Zimmer, N. Klöcker, K. Benndorf, Multi-wavelength TCSPC lifetime imaging, Proc. SPIE 4620 79-84 (2002)
26. W. Becker, A. Bergmann, G. Weiss, Lifetime Imaging with the Zeiss LSM-510, Proc. SPIE 4620, 30-35 (2002)
27. W. Becker, A. Bergmann, M.A. Hink, K. König, K. Benndorf, C. Biskup, Fluorescence lifetime imaging by time-correlated single photon counting, Micr. Res. Techn. 63, 58-66 (2004)
28. W. Becker, Advanced time-correlated single-photon counting techniques. Springer, Berlin, Heidelberg, New York, 2005
29. W. Becker, A. Bergmann, E. Haustein, Z. Petrasek, P. Schwille, C. Biskup, L. Kelbauskas, K. Benndorf, N. Klöcker, T. Anhut, I. Riemann, K. König, Fluorescence lifetime images and correlation spectra obtained by multi-dimensional TCSPC, Micr. Res. Tech. 69, 186-195 (2006)
30. W. Becker, A. Bergmann, C. Biskup, Multi-Spectral Fluorescence Lifetime Imaging by TCSPC. Micr. Res. Tech. 70, 403-409 (2007)
31. Becker, W., Su, B., Weisshart, K. & Holub, O. (2011) FLIM and FCS Detection in Laser-Scanning Microscopes: Increased Efficiency by GaAsP Hybrid Detectors. Micr. Res. Tech. 74, 804-811
32. Becker, W., Su, B., Bergmann, A., Weisshart, K. & Holub, O. (2011) Simultaneous Fluorescence and Phosphorescence Lifetime Imaging. Proc. SPIE 7903, 790320
33. W. Becker, B. Su, A. Bergmann, Spatially resolved recording of transient fluorescence lifetime effects by line-scanning TCSPC. Proc. SPIE 8226 (2012)

34. W. Becker, Fluorescence Lifetime Imaging - Techniques and Applications. J. Microsc. 247 (2) (2012)
35. W. Becker, V. Shcheslavskiy, Fluorescence Lifetime Imaging with Near-Infrared Dyes. Proc. SPIE 8588 (2013)
36. W. Becker, V. Shcheslavskiy, S. Frere, I. Slutsky, Spatially resolved recording of transient fluorescence lifetime effects by line-scanning TCSPC. Microsc. Microsc. Res. Techn. 77, 216-224 (2014)
37. W. Becker, The bh TCSPC handbook. 8th edition. Becker & Hickl GmbH (2019). Available on www.becker-hickl.com, please contact bh for printed copies.
38. W. Becker, The bh TCSPC Technique. Principles and Applications. Available on www.becker-hickl.com.
39. W. Becker, V. Shcheslavskiy, Fluorescence Lifetime Imaging with Near-Infrared Dyes. Photonics and Lasers in Medicine 4, 73-83 (2015)
40. W. Becker (ed.), Advanced time-correlated single photon counting applications. Springer, Berlin, Heidelberg, New York (2015)
41. W. Becker, Introduction to Multi-Dimensional TCSPC. In W. Becker (ed.) Advanced time-correlated single photon counting applications. Springer, Berlin, Heidelberg, New York (2015)
42. W. Becker, V. Shcheslavskiy, H. Studier, TCSPC FLIM with Different Optical Scanning Techniques, in W. Becker (ed.) Advanced time-correlated single photon counting applications. Springer, Berlin, Heidelberg, New York (2015)
43. W. Becker, A. Bergmann, L. Braun, Metabolic Imaging with the DCS-120 Confocal FLIM System: Simultaneous FLIM of NAD(P)H and FAD, Application note, Becker & Hickl GmbH (2019)
44. Becker Wolfgang, Suarez-Ibarrola Rodrigo, Miernik Arkadiusz, Braun Lukas, Metabolic Imaging by Simultaneous FLIM of NAD(P)H and FAD. Current Directions in Biomedical Engineering 5(1), 1-3 (2019)
45. W. Becker, C. Junghans, A. Bergmann, Two-Photon FLIM of Mushroom Spores Reveals Ultra-Fast Decay Component. Application note, available on www.becker-hickl.com.
46. W. Becker, T. Saeb-Gilani, C. Junghans, Two-Photon FLIM of Pollen Grains Reveals Ultra-Fast Decay Component. Application note, available on www.becker-hickl.com
47. M. Y. Berezin, S. Achilefu, Fluorescence lifetime maesurement and biological imaging. Chem. Rev. 110(5), 2641-2684 (2010)
48. O. Berezovska, P. Ramdya, J. Skoch, M.S. Wolfe, B.J. Bacskai, B.T. Hyman, Amyloid precursor protein associates with a nicastrin-dependent docking site on the presenilin 1-γ-secretase complex in cells demonstrated by fluorescence lifetime imaging, J. Neurosci. 23, 4560-4566 (2003)
49. O. Berezovska, B.J. Bacskai, B.T. Hyman, Monitoring Proteins in Intact Cells, Science of Aging Knowledge Environment, SAGE KE 14 (2003)
50. O. Berezovska, A. Lleo, L.D. Herl, M.P. Frosch, E.A. Stern, B.J. Bacskai, B.T. Hyman, Familial Alzheimer's disease presenilin 1 mutations cause alterations in the conformation of prenesilin and interactions with amyloid precursor protein, J. Neurosci. 25, 3009-3017 (2005)
51. D.K. Bird , L. Yan , K. M. Vrotsos , K. E. Eliceiri , E. M. Vaughan. Metabolic mapping of MCF10A human breast cells via multiphoton fluorescence lifetime imaging of coenzyme NADH. Cancer Res 65:8766–8773 (2005)
52. C. Biskup, T. Zimmer, K. Benndorf, FRET between cardiac $Na^+$ channel subunits measured with a confocal microscope and a streak camera, Nature Biotechnology, 22(2), 220-224 (2004)
53. C. Biskup, L. Kelbauskas, T. Zimmer, K. Benndorf, A. Bergmann, W. Becker, J.P. Ruppersberg, C. Stockklausner, N. Klöcker, Interaction of PSD-95 with potassium channels visualized by fluorescence lifetime-based resonance energy transfer imaging, J. Biomed. Opt. 9, 735-759 (2004)
54. C. Biskup, T. Zimmer, L. Kelbauskas, B. Hoffmann, N. Klöcker, W. Becker, A. Bergmann, K. Benndorf, Multi-Dimensional Fluorescence Lifetime and FRET Measurements. Micr. Res. Tech. 70, 403-409 (2007)
55. C. Biskup, B. Hoffmann, K. Benndorf, A. Rueck, Spectrally resolved lifetime imaging microscopy. In: A. Periasamy, R.M. Clegg, eds., FLIM Microscopy in Biology and Medicine. CRC Press 2009
56. C. Biskup, Th. Gensch, Fluorescence lifetime imaging of ions in biological tissue. In: L. Marcu. P.M.W. French, D.S. Elson, (eds.), Fluorecence lifetime spectroscopy and imaging. Principles and applications in biomedical diagnostics. CRC Press, Taylor & Francis Group, Boca Raton, London, New York (2015)
57. T. S. Blacker, Z. F. Mann, J. E. Gale, M. Ziegler, A. J. Bain, G. Szabadkai, M. R. Duchen, Separating NADH and NADPH fluorescence in live cells and tissues using FLIM. Nature Communications 5, 3936-1 to -6 (2014)
58. M. Bosch, J. Castro, T. Saneyoshi, H. Matsuno, M. Sur, Y. Hayashi, Structural and Molecular Remodeling of Dendritic Spine Substructures during Long-Term Potentiation. Neuron 82, 12059-1 to -16 (2014)
59. T. Y. Buryakina, P.-T. Su, W.J. Syu, C.A. Chang, H.-F. Fan, F.-J. Kao, Metabolism of HeLa cells revealed through autofluorescence lifetime upon infection with enterohemorrhagic eschericha coli. J. Biomed. Opt. 17(10) 101503-1 to -9
60. V. Calleja, S. Ameer-Beg, B. Vojnovic, R. Woscholski, J. Downwards, B. Larijani, Monitoring conformational changes of proteins in cells by fluorescence lifetime imaging microscopy, Biochem. J. 372, 33-40 (2003)
61. B. Chance, Pyridine nucleotide as an indicator of the oxygen requirements for energy-linked functions of mitochondria. Circ Res 38, I31–I38 (1976)
62. B. Chance, B. Schoener, R. Oshino, F. Itshak, Y. Nakase, Oxidation–reduction ratio studies of mitochondria in freeze-trapped samples. NADH and flavoprotein fluorescence signals J. Biol. Chem. 254, 4764–4771 (1979)
63. Y. Chen, A. Periasamy, Characterization of two-photon excitation fluorescence lifetime imaging microscopy for protein localization, Microsc. Res. Tech. 63, 72-80 (2004)
64. T. H. Chia, A. Williamson, D. D. Spencer, M. J. Levene, Multiphoton fluorescence lifetime imaging of intrinsic fluorescence in human and rat brain tissue reveals spatially distinct NADH binding. Optics Express 16, 4237-4249 (2008)
65. D. Chorvat, A. Chorvatova, Spectrally resolved time-correlated single photon counting: a novel approach for characterization of endogenous fluorescence in isolated cardiac myocytes. Eur. Biophys. J. 36:73-83 (2006)

66. D. Chorvat, A. Mateasik, J. Kirchnerova, A. Chorvatova, Application of spectral unmixing in multi-wavelength time-resolved spectroscopy. Proc. SPIE 6771, 677105-1 to -12 (2007)
67. D. Chorvat, A. Chorvatova, Multi-wavelength fluorescence lifetime spectroscopy: a new approach to the study of endogenous fluorescence in living cells and tissues. Laser Phys. Lett. 6 175-193 (2009)
68. D. Chorvat Jr., A. Mateasik, Y.g Cheng, N.y Poirier, J. Miro, N.S. Dahdah3, A. Chorvatova, Rejection of transplanted hearts in patients evaluated by the component analysis of multi-wavelength NAD(P)H fluorescence lifetime spectroscopy. J. Biophotonics 3 646-652 (2010)
69. A. Chorvatova, F. Elzwiei, A. Mateasik, D. Chorvat, Effect of ouabain on metabolic oxidative state in living cardiomyocytes eavaluated by time-resolved spectroscopy of endogenous NAAD(P)H fluorescence. J. Biomed. Opt. 17(10) 101505-1 to -7 (2012)
70. A. Chorvatova, S. Aneba, A. Mateasik, D. Chorvat Jr., B. Comte, Time-resolved fluorescence spectroscopy investigation of the effect of 4-hydroxynonenal on endogenous NAD(P)H in living cardiac myocytes. J. Biomed. Opt. 18(6), 067009-1 to -11 (2013)
71. A. Chorvatova, D. Chorvat, Tissue fluorophores and their spectroscopic characteristics. In: L. Marcu. P.M.W. French, D.S. Elson, (eds.), Fluorecence lifetime spectroscopy and imaging. Principles and applications in biomedical diagnostics. CRC Press, Taylor & Francis Group, Boca Raton, London, New York (2015)
72. Y. Dancik, A. Favre, C. J. Loy, A.V. Zvyagin, M.S. Roberts, Use of multiphoton tomography and fluorescence lifetime imaging to investigate skin pigmantation in vivo. J. Biomed. Opt. 18(2) 026022-1 to -13
73. G. Deka, W.W. Wu, F.-J. Kao, In vivo wound healing diagnosis with second harmonic and fluorescence lifetime imaging. J. Biomed. Opt. 18(6), 061222-1 to -8
74. M. A. Digman, V. R. Caiolfa, M. Zamai, and E. Gratton, The phasor approach to fluorescence lifetime imaging analysis, Biophys J 94, L14-L16 (2008)
75. M.A. Digman, E. Gratton, The phasor approach to fluorescence lifetime imaging: Exploiting phasor linear properties. In: L.Marcu, P.W.M. French, D.S. Elson, Fluorescence lifetime spectroscopy and imaging. CRC Press, Taylor & Francis Group, Boca Raton (2015)
76. R. I. Dmitriev, A. V. Zhdanov, Y. M. Nolan, D. B. Papkovsky, Imaging of neurosphere oxygenation with phosphorescent probes. Biomaterials 34, 9307-9317 (2013)
77. R. I. Dmitriev, S. M. Borisov, A. V. Kondrashina, J. M. P. Pakan, U. Anilkumar, J. H. M. Prehn, A. V. Zhdanov, K. W. McDermot, I. Klimant, D. B. Papkovsky, Imaging oxygen in neural cell and tissue models by means of anionic cell-permeable phosphorescent nanoparticles. Biomaterials 34, 9307-9317 (2013)
78. R. I. Dmitriev and D. B. Papkovsky, Intracellular probes for imaging oxygen concentrations: how good are they? Methods Appl. Fluoresc. 3, 034001-034010 (2015)
79. R. I. Dmitriev, S. M. Borisov, H. Düssmann, S. Sun, B. J. Müller, J. Prehn, V. P. Baklaushev, I. Klimant, D. B. Papkovsky, Versatile Conjugated Polymer Nanoparticles for High-Resolution O2 Imaging in Cells and 3D Tissue Models. ACS Nano 9, 5275–5288 (2015)
80. K. Dore, S. Labrecque, C. Tardif, P. De Koninck, FRET-FLIM Investigation of PSD95-NMDA Receptor Interaction in Dendritic Spines; Control by Calpain, CaMKII and Src Family Kinase. PLOS ONE 9(11), e112170 (2014)
81. R. I. Dmitriev and D. B. Papkovsky, Multi-parametric $O_2$ Imaging in Three-Dimensional Neural Cell Models with the Phosphorescent Probes. In: Laura Lossi and Adalberto Merighi (eds.), Neuronal Cell Death: Methods and Protocols, Methods in Molecular Biology, vol. 1254, DOI 10.1007/978-1-4939-2152-2_5, Springer Science+Business Media New York (2015)
82. R.R. Duncan, A. Bergmann, M.A. Cousin, D.K. Apps, M.J. Shipston, Multi-dimensional time-correlated single-photon counting (TCSPC) fluorescence lifetime imaging microscopy (FLIM) to detect FRET in cells, J. Microsc. 215, 1-12 (2004)
83. C. Dysli, G. Quellec, M Abegg, M. N. Menke, U. Wolf-Schnurrbusch, J. Kowal, J. Blatz, O. La Schiazza, A. B. Leichtle, S. Wolf, M. S. Zinkernagel, Quantitative Analysis of Fluorescence Lifetime Measurements of the Macula Using the Fluorescence Lifetime Imaging Ophthalmoscope in Healthy Subjects. IOVS 55, 2107-2113 (2014)
84. Th. Förster, Zwischenmolekulare Energiewanderung und Fluoreszenz, Ann. Phys. (Serie 6) 2, 55-75 (1948)
85. Th. Förster, Energy migration anf fluorescence. Translated by Klaus Suhling. J. Biomed. Opt. 17 011002-1 to -10
86. H. Fogel, S. Frere, O. Segev, S. Bharill, I. Shapira, N. Gazit, T. O'Malley, E. Slomowitz, Y. Berdichevsky, D.M. Walsh, E.Y. Isacoff, J.A. Hirsch, I. Slutsky, APP homodimers transduce an amyloid-β-mediated increase in release probability at excitatory synapses. Cell Rep. 7 1560-1576 (2014)
87. J.H. Fox, T. Connor, M. Stiles, J. Kama, Z. Lu, K. Dorsey, G. Lieberman, E. Sapp, R.A. Cherny, M. Banks, I. Volitakis, M. DiFiglia, O. Berezovska, A.I. Bush, S.M. Hersch, Cysteine Oxidation within N-terminal Mutant Huntingtin Promotes Oligomerization and Delays Clearance of Soluble Protein. J. Biol. Chem. 286, 18320-18330 (2011)
88. S. Frere, I. Slutsky, Calcium imaging using Transient Fluorescence-Lifetime Imaging by Line-Scanning TCSPC. In: W. Becker (ed.) Advanced time-correlated single photon counting applications. Springer, Berlin, Heidelberg, New York (2015)
89. W. Becker, S. Frere, I. Slutsky, Recording $Ca^{++}$ Transients in Neurons by TCSPC FLIM. In:F.-J. Kao, G. Keiser, A. Gogoi, (eds.), Advanced optical methods of brain imaging. Springer (2019)
90. K. Funk, A. Woitecki, C. Franjic-Würtz, Th. Gensch, F. Möhrlein, S. Frings, Modulation of chloride homeostasis by inflammatory mediators in dorsal ganglion neurons. Molecular Pain 4:32 (2008)
91. E. Gagnon, D.A. Schubert, S. Gordo, H.H. Chu, K.W. Wucherpfennig, Local Changes in lipid environment of TCR microclusters regulate membrane binding by the CD3ε cytoplasmic domain. J. Eperimental Medicine, 209, 2423 (2012)
92. U. Gehlsen, A. Oetke, M. Szaszak, N. Koop, F. Paulsen, Andreas Gebert, G. Huettmann, P. Steven, Two-photon fluorescence lifetime imaging monitors metabolic changes during wound healing of corneal epithelial cells in vitro. Graefes Arch. Clin. Exp. Ophthalmol 250, 1293-1302 (2012)

93. Th. Gensch, V. Untiet, A. Franzen, P. Kovermann, C. Fahlke, Determination of Intracellular Chloride Concentrations by Fluorescence Lifetime Imaging. In: W. Becker (ed.) Advanced time-correlated single photon counting applications. Springer, Berlin, Heidelberg, New York (2015)
94. H.C. Gerritsen, M.A.H. Asselbergs, A.V. Agronskaia, W.G.J.H.M. van Sark, Fluorescence lifetime imaging in scanning microscopes: acquisition speed, photon economy and lifetime resolution, J. Microsc. 206, 218-224 (2002)
95. B. Geusens, M. Van Gele, S. Braat, S.C. De Smedt, M.C.A. Stuart, T.W. Prow, W. Sanchez, M. Roberts, N.N. Sanders, J. Lambert, Flexible nanosomes (SECosomes) enable efficient siRNA delivery in cultured primary skin cells and in the viable epidermis of ex vivo human skin. Adv. Funct. Mater. 20, 4077-4090 (2010)
96. Govindjee, M.J. Seufferheld, Non-photochemical quenching of chlorophyll α Fluorescence: Early history and characterization of two xanthophyll-cycle mutants of Chlamydomonas Reinhardtii, Funct. Plant Biol. **29**, 1141-1155 (2002)
97. V. Ghukasyan, Y.-Y. Hsu, S.-H. Kung, F.-J. Kao, Application of fluorescence resonance energy transfer resolved by fluorescence lifetime imaging microscopy for the detection of enterovirus 71 infection in cells, J. Biomed. Opt. 12, 024016-1 to -8 (2007)
98. V. Ghukassian, F.-J. Kao, Monitoring cellular metabolism with fluorescence lifetime of reduced nicotinamide adenine dinucleotide. J. Phys. Chem. C, 113, 11532-11540 (2009)
99. V.V. Ghukasyan, A.H. Heikal, Natural biomarkers for cellular metabolism. Biology, techniques, and applications. CRC Press, Taylor and Francis Group, Boca Raton, London, New York (2015)
100. D. Gilbert, C. Franjic-Würtz, K. Funk, T. Gensch, S. Frings, F. Möhrlen, Differential maturation of chloride homeostasis in primary afferent neurons of the somatosensory system. Int. J. Devl. Neuroscience 25, 479-489 (2007)
101. C. Guardia-Laguarta, M. Coma, M. Pera, J. Clarimon, L. Sereno, J.M. Agullo, L. Molina-Porcel, E. Gallordo, A. Deng, O. Berezovska, B. Hyman, R. Blesa, T. Gomez-Isla, A. Lleo, Mild cholesterol depletion reduces amyloid-β production by impairing APP trafficking to the cell surface. J. Neurochem. 110, 220-230 (2009)
102. K. Drozdowicz-Tomsia, A. G. Anwer, M. A. Cahill, K. N. Madlum, A. M. Maki, M. S. Baker, E. M. Goldys, Multiphoton fluorescence lifetime imaging microscopy reveals free-to-bound NADH ratio changes associated with metabolic inhibition. J. Biomed. Opt. 19, 08601 (2014)
103. H.-W. Guo, C.-T. Chen, Y.-H. Wei, O. K. Lee, V. Gukassyan, F.-J. Kao, H.-W. Wanga, Reduced nicotinamide adenine dinucleotide fluorescence lifetime separates human mesenchymal stem cells from differentiated progenies. J. Biomed. Opt. 13(5) 050505-1 to 3 (2008)
104. K.M. Hanson, M.J. Behne, N.P. Barry, T.M. Mauro, E. Gratton, Two-photon fluorescence imaging of the skin stratum corneum pH gradient, Biophys. J. 83, 1682-1690 (2002)
105. K. Hasegawa, S. J. Ryu, P. Kaláb, Chromosomal gain promotes formation of a steep RanGTP gradient that drives mitosis in aneuploid cells. J. Cell Biol. Vol. 200 No. 2 151–161
106. A. Heikal, Intracellular coenzymes as natural biomarkers for metabolic activities and mitochondrial anomalies. Biomark. Med. 4(2), 241–263 (2010)
107. L. Herl, A. V. Thomas, C. M. Lill, M. Banks, A. Deng, P. B. Jones, R. Spoelgen, B. T. Hyman, O. Berezovska, Mutations in amyloid precursor protein affect its interactions with presenilin/γ-secretase. Molecular and Cellular Neuroscience 41, 166–174 (2009)
108. N. A. Hosny, G. Mohamedi, P. Rademeyer, J. Owen, Y. Wu, M. X. Tang, R. J. Eckersley, E. Stride, and M. K. Kuimova, Mapping microbubble viscosity using fluorescence lifetime imaging of molecular rotors. Proc Natl Acad Sci U S A 110, 9225-9230 (2013)
109. M. M. Janas, B. Wang, A. S. Harris, M. Aguiar, J. M. Shaffer, Y. V. B. K. Subrahmanyam, M. A. Behlke, K. W. Wucherpfennig, S. P. Gygi, E. Gagnon, and C. D. Novina, Alternative RISC assembly: binding and repression of microRNA-mRNA duplexes by human Ago proteins. RNA N. Y. N, 18, no. 11, 2041–2055 (2012)
110. J. Jenkins, R. I. Dmitriev, D. B. Papkovsky, Imaging Cell and Tissue $O_2$ by TCSPC-PLIM. In: W. Becker (ed.) Advanced time-correlated single photon counting applications. Springer, Berlin, Heidelberg, New York (2015)
111. J. Jenkins, R. I. Dmitriev, K. Morten, K. W. McDermott, D. B. Papkovsky, Oxygen-sensing scaffolds for 3-dimensional cell and tissue culture. Acta Biomaterialia 16, 126–135 (2015)
112. J. Jenkins, D. B. Papkovsky and R. I. Dmitriev, The $Ca^{2+}$ /$Mn^{2+}$-transporting SPCA2 pump is regulated by oxygen and cell density in colon cancer cells. Biochem. J. 473, 2507-2518 (2016)
113. J. Jenkins, S. M. Borisov, D. B. Papkovsky, R. I. Dmitriev, Sulforhodamine Nanothermometer for Multiparametric Fluorescence Lifetime Imaging Microscopy. Anal. Chem. 88, 10566-10572
114. P. B. Jones, K.W. Adams, A. Rozkalne, T.L. Spires-Jones, T.T. Hshieh, T. Hashimoto1, C.A. F. von Armin, M. Mielke, B.J. Bacskai, B.T. Hyman, Apolipoprotein E: Isoform Specific Differences in Tertiary Structure and Interaction with Amyloid-b in Human Alzheimer Brain.
115. V. Jyothikumar, Y. Sun, A. Periasamy, Investigation of tyrptopahn-NADH in live human cells using 3-photon fluorescence lifetime imaging. J. Biomed. Opt. 18(6), 060501 (2013)
116. S. Kalinina, V. Shcheslavskiy, W. Becker, J. Breymayer, P. Schäfer, A. Rück, Correlative NAD(P)H-FLIM and oxygen sensing-PLIM for metabolic mapping. J. Biophotonics 9(8):800-811 (2016)
117. H. Kaneko, I. Putzier, S. Frings, U. B. Kaupp, and Th. Gensch, Chloride Accumulation in Mammalian Olfactory Sensory Neurons, J. Neurosci., 24(36) 7931-7938 (2004)
118. S. R. Kantelhardt, J. Leppert, J. Krajewski, N. Petkus, E. Reusche, V. M. Tronnier, G. Hüttmann, A. Giese, Imaging of brain and brain tumor specimens by time-resolved multiphoton excitation microscopy ex vivo. Neuro-Onkology April 2007, 103-112
119. V. Katsoulidou, A. Bergmann, W. Becker, How fast can TCSPC FLIM be made? Proc. SPIE 6771, 67710B-1 to 67710B-7 (2007)
120. H. Kautsky, A. Hirsch, Neue Versuche zur Kohlensäureassimilation, Naturwissenschaften **19**, 964 (1931)
121. M. J. Koehler, K. König, P. Elsner, R. Bückle, M. Kaatz, In vivo assessment of human skin aging by multiphoton laser scanning tomography, Opt. Lett. 31, 2879-2881 (2006)

122. M. Köllner, J. Wolfrum, How many photons are necessary for fluorescence-lifetime measurements?, Phys. Chem. Lett. 200, 199-204 (1992)
123. K. König, P.T.C. So, W.W. Mantulin, B.J. Tromberg, E. Gratton, Two-Photon excited lifetime imaging of autofluorescence in cells during UVA and NIR photostress, J. Microsc. **183**, 197-204 (1996)
124. K. König, I. Riemann, High-resolution multiphoton tomography of human skin with subcellular spatial resolution and picosecond time resolution, J. Biom. Opt. **8**, 432-439 (2003)
125. K. Koenig, Clinical multiphoton tomography. J. Biophoton. 1, 13–23 (2008)
126. K. König, Multiphoton-induced cell damage. In: B.R. Masters, P.T.C. So, eds., Handbook of Biomedical Nonlinear Optical Microscopy.Oxford University Press 2008
127. K. Koenig, A. Uchugonova, Multiphoton Fluorescence Lifetime Imaging at the Dawn of Clinical Application. In: A. Periasamy, R.M. Clegg, eds., FLIM Microscopy in Biology and Medicine. CRC Press 2009
128. K. König, A. Uchugonova, E. Gorjup, Multiphoton Fluorescence Lifetime Imaging of 3D-Stem Cell Spheroids During Differentiation. Microsc. Res. Techn. 74, 9-17(2011)
129. E. I. Koshel, P. S. Chelushkin, A. S. Melnikov, P. Y. Serdobintsev, A. Yu. Stolbovaia, A. F. Saifitdinova, V. I. Shcheslavskiy, O.r Chernyavskiy, E. R. Gaginskaya, I. O. Koshevoy, S. P. Tunik, Lipophilic phosphorescent gold(I) clusters as selective probes for visualization of lipid droplets by two-photon microscopy. Journal of Photochemistry and Photobiology A: Chemistry 332 (2017) 122–130
130. T. B. Krasieva, C. Stringari, F. Liu, C.-H. Sun, Y. Kong, M. Balu, F.L.Meyskens, E. Gratton, B.J. Tromberg, Two-photon excited fluorescence lifetime imaging and spectroscopy of melanins in vitro and in vivo. J. Biomed. Opt. 18(3), 031107.1 to -9
131. K.V. Kuchibhotla, C.R. Lattarulo, B. Hyman, B. J. Bacskai, Synchronous hyperactivity and intercellular calcium waves in astrocytes in Alzheimer mice. Science 323, 1211-1215
132. M. K. Kuimova, G. Yahioglu, J. A. Levitt, K. Suhling, Molecular Rotor Measures Viscosity of Live Cells via Fluorescence Lifetime Imaging. J. Am. Chem. Soc. 130, 6672–6673 (2008)
133. H. Kurokawa, H. Ito, M. Inoue, K. Tabata, Y. Sato, K. Yamagata, S. Kizaka-Kondoh, T. Kadonosono, S. Yano, M. Inoue & T. Kamachi, High resolution imaging of intracellular oxygen concentration by phosphorescence lifetime, Scientific Reports **5**, 1-13 (2015)
134. M. Kwaaitaal, N.F. Keinath, Simone Pajonk, C. Biskup, R. Panstruga, Combined Bimolecular Fluorescence Complementation and Förster Resonance Energy Transfer Reveals Ternary SNARE Complex Formation in Living Plant Cells. Plant Physiology 152, 1135-1147 (2010)
135. J.R. Lakowicz, I. Gryczynski, W. Wiczk, J. Kusba, M. Johnson, Correction for incomplete labeling in the measurement of distance distributions by frequency-domain fluorometry, Anal. Biochem. 195, 243-254 (1991)
136. J.R. Lakowicz, H. Szmacinski, K. Nowaczyk, M.L. Johnson, Fluorescence lifetime imaging of free and protein-bound NADH, PNAS 89, 1271-1275 (1992)
137. J.R. Lakowicz, Principles of Fluorescence Spectroscopy, 3rd edn., Springer (2006)
138. J. Leppert, J. Krajewski, S.R. Kantelhardt, S. Schlaffer, N. Petkus, E. Reusche, G. Hüttmann, A. Giese, Multiphoton excitation of autofluorescence for microscopy of glioma tissue. Neurosurgery 58, 759-767 (2006)J. Leppert, J. Krajewski, S.R. Kantelhardt, S. Schlaffer, N. Petkus, E. Reusche, G. Hüttmann, A. Giese, Multiphoton excitation of autofluorescence for microscopy of glioma tissue. Neurosurgery 58, 759-767 (2006)
139. J. A. Levitt, M. K. Kuimova, G. Yahioglu, P.-H. Chung, K. Suhling, D. Phillips, Membrane-Bound Molecular Rotors Measure Viscosity in Live Cells via Fluorescence Lifetime Imaging. J. Phys. Chem. C 2009, 113, 11634–11642
140. L.L. Lin, J. E. Grice, M.K. Butler, A.V. Zvyagin, W. Becker, T. A. Robertson, H.P. Soyer, M. S. Roberts, T.W. Prow, Time-correlated single photon counting for Simultaneous monitoring of zinc oxide nanoparticles and NAD(P)H in intact and barrier-disrupted volunteer skin. Pharm Res. DOI 10.1007/s11095-011-0515-5 (2011)
141. Y. Liu, S. Walter, M. Stagi, D. Cherny, M. Letiembre. W. Schulz-Schaeffer, H. Heine, B. Penke, H. Neumann, K. Fassbender, LPS receptor (CD 4): a receptor for phagocytosis of Alzheimer's amyliod peptide. Brain 28, 778-789 (2005)
142. A. Lleo, O. Berezovska, L. Herl, S. Raju, A. Deng, B.J. Bacskai, M.P. Frosch, M. Irizarry, B.T. Hyman, Nonsteroidal anti-inflammatory drugs lower Aβ42 and change presenilin 1 conformation, Nature Medicine 10, 1065-1066 (2004)
143. M. Lukina, A. Orlova, M. Shirmanova, D. Shirokov, A. Pavlikov, A. Neubauer, H. Studier, W. Becker, E. Zagaynova, T. Yoshihara, S. Tobita, V. Shcheslavskiy, Interrogation of metabolic and oxygen states of tumors with fiber-based luminescence lifetime spectroscopy. Optics Letters 42(4) 731-734 (2017)
144. K. Maxwell, G.N. Johnson, Chlorophyll fluorescence - a practical guide, Journal of Experimental Botany **51**, 659-668 (2000)
145. C.N. Medine, A. McDonald, A, Bergmann, R. Duncan, Time-correlated single photon counting FLIM: Some considerations for Physiologists. Micr. Res. Tech. 70, 421-425 (2007)
146. Y. Miura, G. Hüttmann, R. Orzekowsky-Schroeder, P. Steven, M. Szszak, N. Koop, R. Brinkmann, Two-photon microscopy and fluorescence lifetime imaging of retinal pigment epithel cells under oxydative stress. Invest Ophthalmol Vis Sci, IOVS 54, 3366-3377 (2013)
147. H. Murakoshi, S-J. Lee, R. Yasuda, Highly sensitive and quantitative FRET–FLIM imaging in single dendritic spines using improved non-radiative YFP. Brain Cell Biol. 36, 31-42 (2008)
148. L. Munsie, N. Caron, R. S. Atwal, I. Marsden, E. J. Wild, J. R. Bamburg, S. J. Tabrizi, R. Truant, Mutant huntingtin causes defective actin remodeling during stress: defining a new role for transglutaminase 2 in neurodegenerative disease. Human Molecular Genetics, 2011, Vol. 20, No. 10 1937–1951
149. A. C. Nyborg, L. Herl, O. Berezovska, A. V Thomas, T. B. Ladd, K. Jansen, B. T. Hyman, T. E. Golde, Signal peptide peptidase (SPP) dimer formation as assessed by fluorescence lifetime imaging microscopy (FLIM) in intact cells. Mol. Neurodegener. 1:16 (2006)

150. I. A. Okkelman, A. A. Dolgova, S. Banerjee, J. P. Kerry, A. Volynskii, O. V. Arzhakova, D. B. Papkovsky, Phosphorescent Oxygen and Mechanosensitive Nanostructured Materials Based on Hard Elastic Polypropylene Films. ACS Appl. Mater. Interfaces 9, 13587−13592 (2017)
151. M.N. Pastore, H. Studier, C.S. Bonder, M.S. Roberts, Non-invasive metabolic imaging of melanoma progression. Exp. Dermatol. 26, 607–614 (2017)
152. R. Patalay, C. Talbot, Y. Alexandrov, I. Munro, M. A. A. Neil, K. König, P. M. W. French, A. Chu, G. W. Stamp, C. Dunsby, Quantification of cellular autofluorescence of human skin using multiphoton tomography and fluorescence lifetime imaging in two spectral detection channels. Opt. Expr. 2, 3295-3308 (2011)
153. R.J. Paul, H. Schneckenburger, Oxygen concentration and the oxidation-reduction state of yeast: Determination of free/bound NADH and flavins by time-resolved spectroscopy, Naturwissenschaften 83, 32-35 (1996)
154. S. Pelet, M.J.R. Previte, P.T.C. So, Comparing the quantification of Förster resonance energy transfer measurement accuracies based on intensity, spectral, and lifetime imaging. J. Biomed. Opt. 11 034017-1 to -11 (1006)
155. I. D. Peltan, A.V. Thomas, I. Mikhailenko, D. K. Strickland, B. T. Hyman, C.A.F. von Arnim, Fluorescence lifetime imaging microscopy (FLIM) detects stimulus-dependent phospholylation of the low density lipoprotein receptor-related protein (LRP) in primary neurons. Biochem. Biophys. Res. Commun. 349, 24-30 (2006)
156. A. Periasamy, Methods in Cellular Imaging. Oxford University Press, Oxford New York (2001)
157. A. Periasamy, N. Mazumder, Y. Sun, K. G. Christopher, R. N. Day, FRET Microscopy: Basics, Issues and Advantages of FLIM-FRET Imaging. In: W. Becker (ed.) Advanced time-correlated single photon counting applications. Springer, Berlin, Heidelberg, New York (2015)
158. M. B. M. Pereira, A. M. Santos, D. C. Goncalves, A. C. Cardoso, S. R. Consonni, Fabio C. Gozzo, P. S. Oliveira, A. H. M. Pereira, A. R. Figueiredo, A. O. Tiroli-Cepeda, C. H. I. Ramos, A A. de Thomaz, Carlos L. Cesar, K. G. Franchini, αB-crystallin interacts with and prevents stress-activated proteolysis of focal adhesion kinase by calpain in cardiomyocytes. Nature Communications, 5, 5159 (2014)
159. L. Pires, M. S. Nogueira, S. Pratavieira, L. T. Moriyama, C. Kurachi, Time-resolved fluorescence lifetime for cutaneous melanoma detection. Biomed. Opt. Expr. 5, 2014, 3080-3089
160. M. Peter, S.M. Ameer-Beg, Imaging molecular interactions by multiphoton FLIM, Biology of the Cell 96, 231-236 (2004)
161. P.P. Provenzano, C.T. Rueden, S.M. Trier, L. Yan, S.M. Ponik, D.R. Inman, P.J. Keely, K. W. Eliceiri, Nonlinear optical imaging and spectral-lifetime computational analysis of endogenous and exogenous fluorophores in breast cancer. J. Biomed. Opt. 13(3), 031220-1 to -11 (2008)
162. Tarl W. Prow, Jeffrey E. Grice, Lynlee L. Lin, Rokhaya Faye, Margaret Butler, Wolfgang Becker, Elisabeth M.T. Wurm, Corinne Yoong, Thomas A. Robertson, H. Peter Soyer, Michael S. Roberts, Nanoparticles and microparticles for skin drug delivery. Advanced Drug Delivery Reviews 63, 470–491 (2011)
163. M. Prummer, B. Sick, A. Renn, U.P. Wild, Multiparameter microscopy and spectroscopy for single-molecule analysis, Anal. Chem. 76, 1633-1640 (2004)
164. R. Richards-Kortum, R. Drezek, K. Sokolov, I. Pavlova, M. Follen, Survey of endogenous biological fluorophores. In M.-A. Mycek, B.W. Pogue (eds.), Handbook of Biomedical Fluorescence, Marcel Dekker Inc. New York, Basel, 237-264 (2003)
165. L. Richert, P. Didier, H. de Rocquigny, Y. Mély, Monitoring HIV-1 Protein Oligomerization by FLIM FRET Microscopy. In: W. Becker (ed.) Advanced time-correlated single photon counting applications. Springer, Berlin, Heidelberg, New York (2015)
166. Roberts, M. S., Dancik, Y., Prow, T.W., Thorling, C.A., Li, L., Grice, J.E., Robertson, T.A., König, K., Becker,W. Non-invasive imaging of skin physiology and percutaneous penetration using 5D (space, time and anisotropy) fluorescence spectral and lifetime imaging with multiphoton and confocal microscopy. European Journal of Pharmaceutics and Biopharmaceutics **77**, 469-488 (2011)
167. A. Rück, Ch. Hülshoff, I. Kinzler, W. Becker, R. Steiner, SLIM: A New Method for Molecular Imaging. Micr. Res. Tech. 70, 403-409 (2007)
168. A. Rück, C. Hauser, S. Mosch, S. Kalinina, Spectrally resolved fluorescence lifetime imaging to investigate cell metabolism in malignant and nonmalignant oral mucosa cells. J. Biomed. Opt. 19(9), 096005-1 to -9 (2014)
169. W.Y. Sanchez, T.W. Prow, W.H. Sanchez, J.E.Grice, M.S. Roberts, Analysis of the metaboloic deterioration of ex-vivo skin, from ischemic necrosis, through the imaging of intracellular NAD(P)H by multiphoton tomography and fluorescence lifetime imaging microscopy (MPT-FLIM). J. Biomed. Opt. 09567RR in press (2010)
170. W.Y. Sanchez, C. Obispo, E. Ryan, J. E. Grice, M.S. Roberts, Changes in the redox state and endogenous fluorescence of in vivo human skin due to intrinsic and photo-induced aging, measured by multiphoton tomography with fluorescence lifetime imaging. J. Biomed. Opt. 18(6), 061217-1 to -12
171. W. Y. Sanchez, M. Pastore, I. Haridass, K. König, W. Becker, M. S. Roberts, Fluorescence Lifetime Imaging of the Skin. In: W. Becker (ed.) Advanced time-correlated single photon counting applications. Springer, Berlin, Heidelberg, New York (2015)
172. D. Schweitzer, A. Kolb, M. Hammer, E. Thamm, Tau-mapping of the autofluorescence of the human ocular fundus, Proc. SPIE 4164, 79-89 (2000)
173. D. Schweitzer, M. Hammer, F. Schweitzer, R. Anders, T. Doebbecke, S. Schenke, E. R. Gaillard, In vivo measurement of time-resolved autofluorescence at the human fundus, J. Biomed. Opt. **9**, 1214-1222 (2004)
174. D. Schweitzer, S. Schenke, M. Hammer, F. Schweitzer, S. Jentsch, E. Birckner, W. Becker, Towards Metabolic Mapping of the Human Retina. Micr. Res. Tech. 70, 403-409 (2007)
175. D. Schweitzer, S. Quick, S. Schenke, M. Klemm, S. Gehlert, M. Hammer, S. Jentsch, J. Fischer, Vergleich von Parametern der zeitaufgelösten Autofluoreszenz bei Gesunden und Patienten mit früher AMD. Der Ophthalmologe 8 (2009)
176. D. Schweitzer, Quantifying fundus autofluorescence. In: N. Lois, J.V. Forrester, eds., Fundus autofluorescence. Wolters Kluwer, Lippincott Willams & Wilkins (2009)
177. D. Schweitzer, Metabolic Mapping. In: F.G. Holz, R.F. Spaide (eds), Medical retina, Essential in Opthalmology, Springer (2010)

178. D. Schweitzer, E.R. Gaillard, J. Dillon, R.F. Mullins, S. Russell, B. Hoffmann, S. Peters, M. Hammer, C. Biskup, Time-Resolved Autofluorescence Imaging of Human Donor Retina Tissue from Donors with Significant Extramacular Drusen. IOVS, 53, 3376-3386 (2012)
179. D. Schweitzer, Autofluorescence diagnostics of ophthalmic diseases. In: V.V. Ghukasyan, A.H. Heikal, eds., Natural biomarkers for cellular metabolism. Biology, techniques, and applications. CRC Press, Taylor and Francis Group, Boca Raton, London, New York (2015)
180. D. Schweitzer, M. Hammer, Fluorescence Lifetime Imaging in Ophthalmology. In: W. Becker (ed.) Advanced time-correlated single photon counting applications. Springer, Berlin, Heidelberg, New York (2015)
181. D. Schweitzer, Ophthalmic applications of FLIM. In: L. Marcu. P.M.W. French, D.S. Elson, (eds.), Fluorecence lifetime spectroscopy and imaging. Principles and applications in biomedical diagnostics. CRC Press, Taylor & Francis Group, Boca Raton, London, New York (2015)
182. V. I. Shcheslavskiy, A. Neubauer, R. Bukowiecki, F. Dinter, W. Becker, Combined fluorescence and phosphorescence lifetime imaging. Appl. Phys. Lett. 108, 091111-1 to -5 (2016)
183. T. F. Sergeeva, M. V. Shirmanova, O. A. Zlobovskaya, A. I. Gavrina, V. V. Dudenkova, M. M. Lukina, K. A. Lukyanov, E. V. Zagaynova, Relationship between intracellular pH, metabolic cofactors, and caspase-3 activation in cancer cells during apoptosis. BBA - Molecular Cell Research (2017)
184. S. Sever, J. Skoch, S. Newmyer, R. Ramachandran, D. Ko, M. McKee, R. Bouley, D. Ausiello, B. T Hyman, B. J. Bacskai, Physical and functional connection between auxilin and dynamin during endocytosis. EMBO J. 25, 4163-4174 (2006)
185. S. Sever, J. Skoch, B. J. Bacskai, S. Newmyer, Assays and functional properties of auxilin-dynamin interactions. Methods Enzymol. 404, 570-585 (2005)
186. Y.-F. Shen, M.-R. Tsai, S.-C. Chen, Y.-S. Leung, C.-T. Hsieh, Y.-S. Chen, F.-L. Huang, R. P. Obena, M. M. L. Zulueta, H.-Y. Huang, W.-J. Lee, K.-C. Tang, C.-T. Kung, M.-H. Chen, D.-B. Shieh, Y.-J. Chen, T.-M. Liu, P.-T. Chou, and C.-K. Sun, Imaging endogenous bilirubins with two-photon fluorescence of bilirubin dimers. Anal. Chem. 87, 7575-7582 (2015)
187. M. V. Shirmanova, I. N. Druzhkova, M. M. Lukina, V. V. Dudenkova, N. I. Ignatova, L. B. Snopova, V. I. Shcheslavskiy, V. V. Belousov, E. V. Zagaynova, Chemotherapy with cisplatin: insights into intracellular pH and metabolic landscape of cancer cells in vitro and in vivo. Scientific Reports 7, 8911-1 to -11
188. M. C. Skala, K. M. Riching, D. K. Bird, A. Dendron-Fitzpatrick, J. Eickhoff, K. W. Eliceiri, P. J. Keely, N. Ramanujam, In vivo multiphoton fluorescence lifetime imaging of protein-bound and free nicotinamide adenine dinucleotide in normal and precancerous epithelia. J. Biomed. Opt. 12 02401-1 to 10 (2007)
189. M. C. Skala, K. M. Riching, A. Gendron-Fitzpatrick, J. Eickhoff, K. W. Eliceiri, J. G. White, N. Ramanujam, In vivo multiphoton microscopy of NADH and FAD redox states, fluorescence lifetimes, and cellular morphology in precancerous epithelia, PNAS 104, 19494-19499 (2007)
190. M.C. Skala, A. Fontanella, L. Lan, J.A. Izatt, M.W. Dewhirst, Longitudinal optical imaging of tumor metabolism and hemodynamics. J. Biomed. Opt. 15(1) 011112-1 to -8 (2010)
191. M.C. Skala, N. Ramanujam, Multiphoton Redox Ratio Imaging for Metabolic Monitoring in vivo. Methods Mol. Biol. 594, 155-162 (2010)
192. J. F. Soderholm, S. L. Bird, P. Kalab, Y.i Sampathkumar, K Hasegawa, M. Uehara-Bingen, Karsten Weis, R. Heald, Importazole, a small molecule inhibitor of the transport receptorimportin-β. ACS Chem Biol. 15, 6, 700–708 (2011)
193. Studier, H., Becker, W. Megapixel FLIM. Proc. SPIE 8948, (2014)
194. E. Stuntz, Y. Gong1, D. Sood, V. Liaudanskaya, D. Pouli, K. P. Quinn, C. Alonzo, Z. Liu1, D. L. Kaplan, I. Georgakoudi, Endogenous Two-Photon Excited Fluorescence Imaging Characterizes Neuron and Astrocyte Metabolic Responses to Manganese Toxicity. Scientific Reports 7, 1041-1 to -15 (2017)
195. K. Suhling, L. M. Hirvonen, J. A. Levitt, P.-H. Chung, C. Tregido, A. le Marois, D. Rusakov, K. Zheng, Fluorescence Lifetime Imaging (FLIM): Basic Concepts and Recent Applications. In: W. Becker (ed.) Advanced time-correlated single photon counting applications. Springer, Berlin, Heidelberg, New York (2015)
196. Y. Sun, J. Qu, G. Xu, L. Zhao, H. Niu, Autofluorescence lifetime imaging of Lipofuscin and melanin in retinal pigment epithelium cells. Invest Ophthalmol Vis Sci, IOVS 48, 2965 (2007)
197. M. Szaszak, P. Steven, K. Shima, R. Orzekowsky-Schröder, Gereon Hüttmann, I.R. König, W. Solbach, J. Rupp, Fluorescence Lifetime Imaging Unravels C. trachomatis Metabolism and Its Crosstalk with the Host Cell. PLOS Pathogens 7, e1002108-1 to 12 (2011)
198. C. Toncelli, O. V. Arzhakova, A. Dolgova, A. L. Volynskii, N. F. Bakeev, J. P. Kerry, D. B. Papkovsky, Oxygen-sensitive phosphorescent nanomaterials produced from high density polyethylene films by local solvent-crazing. Anal. Chem. 86(3), 1917-23 (2014)
199. C. Tregido, J.A. Levitt, K. Suhling, Effect of refractive index on the fluorescence lifetime of green fluorescent protein. J. Biomed. Opt. 13(3), 031218-1 to -8 (2008)
200. Y. Ueda, S. Kwok, Y. Hayashi, Application of FRET probes in the analysis of neuronal plasticity, Frontiers in neural circuits 7, 163 (2013)
201. Y. Ueda, Y. Hayashi, $PIP_3$ regulates spinule formation in dentritic spines structural long-term potentiation. J. Neurosci. 33(27) 11040-11047 (2013)
202. K. Uemura, C. M. Lill, M. Banks, M. Asada, N. Aoyagi, K. Ando, M. Kubota, T. Kihara, T. Nishimoto, H. Sugimoto, R. Talahashi, B. T. Hyman, S. Shimohama, O. Berezovska, A. Kinoshita, N-cadherin-based adhesion anhances Aβ releases and decreases $Aβ_{42/40}$ ratio. J. Neurochem. 108, 350-360 (2009)
203. H.D. Vishwasrao, A. A. Heikal, K.A. Kasischke, W. W. Webb, Conformational Dependence of Intracellular NADH on Metabolic State Revealed by Associated Fluorescence Anisotropy. J. Biol. Chem. 280, 25119-25126 (2005)

204. A. Walsh, R.C. Cook, B. Rexer, C.L. Arteaga, M.C. Skala, Optical Imaging of metabolism in HER2 overexpressing breast cancer cells. Biomedical Optics Express 3(1), 75-85 (2012)
205. A. J. Walsh, R. S. Cook, H. C. Manning, D. J. Hicks, A. Lafontant, C. L. Arteaga, M. C. Skala, Optical Metabolic Imaging Identifies Glycolytic Levels, Subtypes, and Early-Treatment Response in Breast Cancer. Cancer Res. 73, 6164-6174 (2013)
206. A. J. Walsh, R. S. Cook, M. E. Sanders, L. Aurisicchio, G. Ciliberto, C. L. Arteaga, M. C. Skala, Quantitative Optical Imaging of Primary Tumor Organoid Metabolism Predicts Drug Response in Breast Cancer. Cancer Res 74, OF1-OF11 (2014)
207. A. J. Walsh, A. T. Shah, J. T. Sharick, M. C. Skala, Fluorescence Lifetime measurements of NADH in live cells and tissue. In: W. Becker (ed.) Advanced time-correlated single photon counting applications. Springer, Berlin, Heidelberg, New York (2015)
208. A. J. Walsh, M. C. Skala, Optical metabolic imaging quantifies heterogeneous cell populations. Biomed. Opt. Expr. 6, 559-573 (2015)
209. H-W. Wang, V. Ghukassyan, C.T. Chen, Y.H. Wei, H.W. Guo, J.S. Yu, F.J. Kao, Differentiation of appoptosis from necrosis by dynamic changes of reduced nicotinamide adenine dinucleotide fluorescence lifetime in live cells. J. Biomed. Opt. 13(5), 054011-1 to 9 (2008)
210. O. Warburg, On the origin of cancer cells. Science 123, 309-314 (1956)
211. O. Warburg, On respiratory impairment in cancer cells. Science 124, 269-270 (1956)
212. J. Widengren, V. Kudryavtsev, M. Antonik, S. Berger. M. Gerken, C. A. M. Seidel, Single-molecule detection and identification of multiple species by multiparameter fluorescence detection. Anal.Chem. 78, 2039-2050 (2006)
213. M.A. Yaseen, S. Sakadzic, w. Wu, W. Becker, K.A. Kasischke, D.A. Boas, In vivo imaging of cerebral enery matabolism with two-photon fluorescence lifetime imaging microscopy of NADH. Biomed. Opt. Expr. 4, 307-321 (2013)
214. G. Yazgan, R. I. Dmitriev, V Tyagi, J.Jenkins, G-M. Rotaru, M.Rottmar, R. . Rossi, C. Toncelli, D. B. Papkovsky, K. Maniura-Weber, G. Fortunato, Steering surface topographies of electrospun fibers: understanding the mechanisms. Scietific Reports 7, 158-1 to -13 (2017)
215. Q. Yu, A. A. Heikal, Two-photon autofluorescence dynamics imaging reveals sensitivity of intracellular NADH concentration and conformation to cell physiology at the single-cell level. J. Photochem. Photobiol. B 95, 46-57 (2009)
216. A. V. Zhdanov, A. V. Golubeva, I. A. Okkelman, J. F. Cryan, D. B. Papkovsky, Imaging of oxygen gradients in giant umbrella cells: an ex vivo PLIM study. Am J Physiol Cell Physiol 309, 2015
217. A. V. Zhdanov, I. A. Okkelman, F. W. J. Collins, S. Melgar, D.i B. Papkovsky, A novel effect of DMOG on cell metabolism: direct inhibition of mitochondrial function precedes HIF target gene expression. Biochimica et Biophysica Acta 1847, 1254–1266 (2015)
218. A. V. Zhdanov, I. A. Okkelman, A. V. Golubeva, B. Doerr, N. P. Hyland, S. Melgar, F. Shanahan, J. F. Cryan, D. B. Papkovsky, Quantitative analysis of mucosal oxygenation using ex vivoimaging of healthy and inflamed mammalian colon tissue. Cell. Mol. Life Sci. 74, 141–151 (2017)
219. K. M. Zoltowska, M.o Maesako, I. Lushnikova, S. Takeda, Laura J. Keller, G, Skibo, B. T. Hyman, O. Berezovska, Dynamic presenilin 1 and synaptotagmin 1 interaction modulates exocytosis and amyloid β production. Molecular Neurodegeneration 12, 15 (2017)

# Specifications

## General Principle

| | |
|---|---|
| Lifetime measurement | time-domain |
| Excitation | high-frequency pulsed lasers |
| Buildup of lifetime images | Single-photon detection by multi-dimensional TCSPC [37] |
| | Builds up distribution of photons over photon arrival time |
| | after laser pulses, scan coordinates, |
| | time from laser modulation, time from start of experiment. |
| Multi-wavelength FLIM | uses wavelength of photons as additional coordinate of photon distribution |
| Excitation wavelength multiplexing | uses laser number as additional coordinate of photon distribution |
| Scan rate | works at any scan rate |
| Buildup of fluorescence correlation data | correlation of absolute photon times [37] |
| General operation modes | FLIM, two spectral or polarisation channels |
| | Multi-wavelength FLIM |
| | Time-series FLIM, microscope-controlled time series |
| | Z-Stack FLIM |
| | Mosaic FLIM, x,y, z, temporal |
| | Excitation-wavelength multiplexed FLIM |
| | FLITS (fluorescence lifetime-transient scanning) |
| | PLIM (phosphorescence lifetime imaging) simultaneous with FLIM |
| | FCS, cross FCS, gated FCS, PCH |
| | Single-point fluorescence decay recording |

## Data recording hardware, please see [37] for details

| | | | | |
|---|---|---|---|---|
| TCSPC System | SPC-150NX or SPC-180NX TCSPC / FLIM modules | | | |
| Number of parallel TCSPC / FLIM channels | typ. 2, min. 1, max 4 | | | |
| Number of detector (routing) channels in FLIM modes | 16 for each FLIM channel | | | |
| Principle | Advanced TAC/ADC principle | | | |
| Electrical time resolution | 1.63 ps rms / 3.5 ps fwhm | | | |
| Minimum time channel width | 405 fs | | | |
| Timing stability over 30 minutes | typ. better than 5ps | | | |
| Dead time | SPC-150NX: 100 ns / SPC-180NX: 80 ns | | | |
| Saturated count rate | 10 MHZ / 12 MHz per channel | | | |
| Dual-time-base operation | via micro times from TAC and via macro time clock | | | |
| Source of macro time clock | internal 40MHz clock or from laser | | | |
| Input from detector | constant-fraction discriminator | | | |
| Reference (SYNC) input | constant-fraction discriminator | | | |
| Synchronisation with scanning | via frame clock, line clock and pixel clock pulses | | | |
| Scan rate | any scan rate | | | |
| Synchronisation with laser multiplexing | via routing function | | | |
| Recording of multi-wavelength data | simultaneous in 16 channels, via routing function | | | |
| Experiment trigger function | TTL, used for Z stack FLIM and microscope-controlled time series | | | |
| Basic acquisition principles | on-board-buildup of photon distributions | | | |
| | buildup of photon distributions in computer memory | | | |
| | generation of parameter-tagged single-photon data | | | |
| | online auto or cross correlation and PCH | | | |
| Operation modes | f(t), oscilloscope, f(txy), f(t,T), f(t) continuous flow | | | |
| | FIFO (correlation / FCS / MCS) mode | | | |
| | Scan Sync In imaging, Scan Sync In with continuous flow | | | |
| | FIFO imaging, with MCS imaging, mosaic imaging, time-series imaging | | | |
| | Multi-detector operation, laser multiplexing operation | | | |
| | cycle and repeat function, autosave function | | | |
| Max. Image size, pixels (SPCM 64 bit software) | 4096x4096 | 2048x2048 | 512x512 | 256x256 |
| No of time channels, see [37] | 64 | 256 | 1024 | 4096 |

## Data Acquisition Software, please see [37] for details

| | |
|---|---|
| Operating system | Windows 10, 64 bit |
| Loading of system configuration | single click in predefined setup panel |
| Start / stop of measurement | by operator or by timer, starts with start of scan, stops with end of frame |
| Online calculation and display, FLIM, PLIM | in intervals of Display Time, min. 1 second |
| Online calculation and display, FCS, PCH | in intervals of Display Time, min. 1 second |

| | |
|---|---|
| Number of images displayed simultaneously | max 8 |
| Number of curves (Decay, FCS, PCH, Multiscaler) | 8 in one curve window |
| Cycle, repeat, autosave functions | user-defined, used for<br>for time-series recording, Z stack FLIM,<br>microscope-controlled time series |
| Saving of measurement data | User command or autosave function<br>Optional saving of parameter-tagged single-photon data |
| Link to SPCImage data analysis | automatically after end of measurement or by user command |

## Data Analysis: bh SPCImage, integrated in bh TCSPC package, see [6] or [37]

| | |
|---|---|
| Data types processed | FLIM, Lif/Int FLIM, PLIM, MW FLIM, Mosaic FLIM, time-series, Z stacks, single curves |
| Procedures | WLS, MLE or first-moment calculation |
| GPU Processing | MLE, if GPU is present |
| Extra Hardware | NVIDIA GPU, optional |
| IRF | Synthetic IRF or measured IRF |
| Model functions | Single, double, triple exponential decay<br>Single, double, triple exponential incomplete decay models<br>Shifted-component model |
| Parameters displayed | Amplitude- or intensity-weighted average of component lifetimes<br>Ratios of lifetimes or amplitudes, FRET efficiency<br>Fractional intensities of components or ratios of fractional intensities<br>Parameter distributions |
| Phasor Plot | Available for all types of FLIM data |
| Parameter histograms, one-dimensional | Pixel frequency over any decay parameter or ratio of decay parameters |
| Parameter histograms, two-dimensional | Pixel frequency over two decay parameters, Phasor plot |
| ROI definition | Polygon or rectangle |
| Image segmentation | Via Phasor Plot or 2D Histograms |

## Excitation Sources, One-Photon Excitation, please see [6] for details

**Picosecond Diode Lasers, LSM 710...880**

| | |
|---|---|
| Number of lasers | 1 or 2 |
| Configuration | Modified bh BDL-SMC lasers, Integrated in LSM System |
| Wavelengths | 405nm, 445nm |
| Mode of operation | picosecond pulses or CW |
| Pulse width, typical | 40 to 100 ps |
| Pulse frequency | selectable, 20MHz, 50MHz, 80MHz |
| Power in picosecond mode | 0.4mW to 1mW at fibre output. Depends on wavelength version. |
| Power in CW mode | 20 to 40mW at fibre output. Depends on wavelength version. |

**Picosecond Diode Lasers, LSM 980**

| | |
|---|---|
| Number of lasers | 4 |
| Available Wavelengths | 375nm, 405nm, 445nm, 473nm, 488nm, 515nm, 640nm, 685nm, 785nm |
| Configuration | 4 bh BDL-SMC lasers in LHB-104 laser module, single fibre output |
| Mode of operation | Picosecond pulses or CW |
| Pulse width, typical | 40 to 100 ps |
| Pulse frequency | Selectable, 20MHz, 50MHz, 80MHz |
| Power in picosecond mode | 0.2mW to 1mW at fibre output. Depends on wavelength version. |
| Power in CW mode | 20 to 40mW at fibre output. Depends on wavelength version. |

**Lasers Multiplexing**

| | |
|---|---|
| LSM 710..880, integrated ps diode lasers | Multiplexing not available |
| LSM 980, diode lasers in bh LHB-104 Laser Hub | Frame, Line, Pixel |

**Laser Modulation for PLIM**

| | |
|---|---|
| Multiphoton (NLO) systems | Requires bh DDG-210 card and Zeiss PLIM indimo |
| Diode Lasers, LSM 710..880 | not available |
| Diode Lasers, LSM 980 | By electronics of LHB-104 Laser Hub |

## Excitation Sources, Multi-Photon Excitation, please see [6] for details

| | |
|---|---|
| **Femtosecond NIR Lasers** | any femtosecond Ti:Sa laser or Ti:Sa pumped OPO |
| Wavelength | 650 to 1000 |
| Repetition rate | typ. 80 MHz |

| | |
|---|---|
| Laser Modulation for PLIM | requires bh DDG-210 card and Zeiss PLIM indimo |

## Detectors

| | |
|---|---|
| Interface to LSM family microscopes | NDD or BIG adapter |
| Beamsplitter, NDD port | Zeiss NDD T Adapter |
| Beamsplitter, confocal port | bh beamsplitter assembly with Zeiss-type filter cubes<br>detectors are portable between NDD and (confocal) BIG port |
| **Hybrid Detectors (standard)** | bh HPM-100-40 hybrid detector |
| Spectral Range | 300 to 710nm |
| Peak quantum efficiency | 40 to 50% |
| IRF width (fwhm) | 120 to 130 ps |
| Detector area | 3mm |
| Background count rate, thermal | 300 to 2000 counts per second |
| Background from afterpulsing | not detectable |
| Afterpulsing peak in FCS | not detectable |
| Power supply and overload shutdown | via DCC-100 or DCU-400/800 controller of TCSPC system |
| **Hybrid Detectors (ultra-fast, optional)** | bh HPM-100-06 and -07 hybrid detector |
| Spectral Range | -06: 300 to 600nm -07: 300 to 750nm |
| Peak quantum efficiency | 20 % |
| IRF width (fwhm, with Ti:Sa laser) | 19 ps |
| Detector area | 3mm |
| Background count rate, thermal | 100 to 500 counts per second |
| Background from afterpulsing | not detectable |
| Power supply, gain control, overload shutdown | via DCC-100 or DCU-400/800 controller of TCSPC system |
| **Hybrid Detectors for NIR (optional)** | bh HPM-100-50 hybrid detector |
| Spectral Range | 400 to 900nm |
| Peak quantum efficiency | 12 to 15% |
| IRF width (fwhm) | 130 to 160 ps |
| Detector area | 3mm |
| Background count rate, thermal | 1000 to 8000 counts per second |
| Background from afterpulsing | not detectable |
| Power supply, gain control, overload shutdown | via DCC-100 or DCU-400/800 controller of TCSPC system |
| **Multi-Wavelength FLIM Detector (optional)** | bh MW FLIM assembly |
| Spectral range | 380 to 630nm or 380 to 750nm |
| Number of wavelength channels | 16 |
| Spectral width of wavelength channels | 12.5 nm |
| IRF width (fwhm) | 250 ps |
| Power supply, gain control, overload shutdown | via DCC-100 or DCU-400/800 controller of TCSPC system |
| **Zeiss BIG-2 Detector** | |
| IRF width (fwhm, with Ti:Sa laser) | 250 ps |
| Electrical connection | Via bh A-PPI-D adapter |
| Power supply, gain control and overload shutdown | via LSM / ZEN hardware / software |
| Other specifications | please see [15] |

**Becker & Hickl GmbH**
Nunsdorfer Ring 7-9
12277 Berlin, Berlin
Tel.  +49 / 30 / 212 800 20, Fax. +49 / 30 / 212 800 213
email: info@becker-hickl.com, www.becker-hickl.com